Internal Report
DESY F35D-95-01
January 1995

Measurement of Scaled Momentum Distributions in the Breit Frame at HERA using the ZEUS Detector

V. A. Jamieson

'Die Verantwortung für den Inhalt dieses
internen Berichtes liegt ausschließlich beim Verfasser"

Measurement of Scaled Momentum Distributions in the Breit Frame at HERA using the ZEUS Detector

Valerie Ann Jamieson

Department of Physics and Astronomy, University of Glasgow, Glasgow

Abstract

Charged particle production has been studied in Deep Inelastic Scattering (DIS) events using the ZEUS detector. The Central Tracking Detector (CTD) has been a principal component in this analysis. Results from a method developed to measure the hit efficiency of the CTD were used to determine its optimum operating conditions during the data taking period.

Scaled momentum distributions of charged particles have been measured in the current fragmentation region of the Breit frame over a large range of Q^2 from 10 to 1280 GeV^2. In this region, the fragmentation properties of the struck quark in DIS are expected to be similar to those of the quarks produced in e^+e^- annihilation experiments. Transformation from the HERA laboratory frame to the Breit system is shown to be accomplished experimentally. The required Lorentz boost, however, limits the resolution with which the scaled momentum distributions can be measured.

The evolution with Q of the scaled momentum distributions is used to study QCD coherence effects in DIS by comparing to a variety of Monte Carlo models. This comparison reveals that the best description of the data is achieved using models which incorporate coherence effects. The data are compared with theoretical predictions in order to extract a value of $\Lambda_{\rm EFF}$, an effective QCD scale. A comparison between the DIS data and corresponding data from e^+e^- annihilation experiments is made in order to investigate the similarity between the fragmentation properties of quarks in the two distinct processes. A clear agreement is observed between the Q-evolution of the scaled momenta in DIS and e^+e^- annihilation and thereby provides evidence for the universality of quark fragmentation.

Preface

One of the most widely discussed topics of perturbative Quantum Chromodynamics (pQCD) in recent years is the phenomenon of coherence, a natural consequence of the quantum mechanical nature of QCD acting on the parton cascade. As long wavelength gluons are unable to resolve individual colour charges of partons within the parton cascade, the available phase space for soft gluon emissions is reduced to an angular-ordered region due to destructive interference. This leads to a number of important modifications to the properties of the partonic final state relative to the incoherent case. The most notable of these are the slower rise in the multiplicity of partons with increasing energy and the modified shape of the parton momentum spectra to an approximately Gaussian form.

Coherence effects are explicitly included in the Modified Leading Log Approximation (MLLA) of pQCD. The MLLA predicts the parton multiplicity and the form of the momentum spectra from quark fragmentation at a given, sufficiently large energy to be determined experimentally. The hypothesis of Local Hadron Parton Duality (LPHD) which relates the observed hadron distributions to the calculated parton distributions via a constant of proportionality is used in conjunction with the predictions of MLLA. Using this assumption the modifications due to coherence are therefore not only expected to be experimentally observed, but the MLLA calculations should also be directly applicable to data.

So far these effects have been studied at e^+e^- annihilation experiments in terms of the scaled momentum distribution $\ln(1/x_p)$, where $x_p = 2p/\sqrt{s}$, and the

average charged particle multiplicity. The results from these experiments, are in accordance with the MLLA and the assumptions of LPHD.

Operation of the HERA electron-proton collider has extended the kinematic range for studies of the hadronic final state in Deep Inelastic Scattering (DIS). The purpose of this thesis is to compare the properties of the fragmentation process initiated by the struck quark in DIS to those in e^+e^-.

This can best be accomplished by transforming from the HERA laboratory system to the Breit frame of reference, defined as the frame in which the exchanged boson is completely space-like. In the naïve quark parton model the incoming and outgoing quark have equal but opposite momentum after the interaction with the exchanged boson. Particles in the Breit frame can be assigned to one of two regions depending on their longitudinal momentum in the boosted frame. The current region corresponds to particles with $p'_z < 0$, the struck quark direction in the quark parton model; whilst the target region is defined by $p'_z > 0$.

In e^+e^- annihilation the $q\bar{q}$ pair are produced with equal and opposite momenta, $\pm\sqrt{s}/2$. In the Breit frame, the struck quark from DIS has momentum $-Q/2$. In the direction of the outgoing struck quark, scaled momentum spectra are expected to have a similar dependence on Q to those observed in e^+e^- annihilation at energy $\sqrt{s} = Q$.

In this thesis the inclusive scaled momentum distributions of charged hadrons measured in the current region of the Breit frame using the ZEUS Central Tracking Detector (CTD) are presented. The distributions are measured over a wide range of x and Q^2, from $6 \times 10^{-4} < x < 5 \times 10^{-2}$ and $10 < Q^2 < 1280$ GeV^2 and the data are corrected using Monte Carlo techniques. The main causes of systematic uncertainty are studied. Comparisons are made with Monte Carlo models, MLLA calculations and e^+e^- data.

In chapter 1 a description of the HERA accelerator and ZEUS detector is presented, concentrating on the detector components used in the analysis. Brief

explanations of the two track reconstruction algorithms employed in the analysis are given.

A method developed by the author to provide an estimate of the CTD hardware efficiency is recounted in chapter 2. The measurement was used to ascertain the optimum CTD operating conditions during the 1993 running period. The algorithm identified various features of the CTD design and operation and was used to monitor the detector performance throughout the year.

The kinematics of DIS are described in chapter 3. These kinematic quantities, x, Q^2 and y can be calculated in a variety of ways using the scattered lepton and/or outgoing hadronic system. Relevant formulae are given and measurements of the x and Q^2 resolutions from the double-angle method adopted in this analysis are presented.

In chapter 4, some theoretical background to the measurement is given. First a short historical review of the quark parton model is presented. To clarify the origins of coherence, an analogy between coherence in QED showers is drawn. MLLA predictions of the scaled momentum distribution, in particular the evolution of the peak position with Q, are discussed.

The simulation of DIS events using Monte Carlo techniques is discussed in chapter 5. Emphasis is given to the Monte Carlo models which have previously been shown to provide a reasonable description of ZEUS data. These models are used later to correct the data distributions.

A large fraction of the data collected at ZEUS comprises background events to the DIS process. A description of the experimental techniques used to reduce this background and obtain a fiducial sample of DIS events is given in chapter 6. A Monte Carlo study to ascertain those regions of (x, Q^2) which offer a high acceptance for CTD tracks in the current region of the Breit frame is presented.

In chapter 7, experimental aspects of the transformation from the HERA laboratory to the Breit frame are discussed. The magnitude and direction

of the boost is shown to vary across the (x, Q^2) plane. The quality of the boost reconstruction is shown to be the limiting factor in the precision of the measurement and the $\ln(1/x_p)$ resolution is determined.

The scaled momentum distributions are presented in chapter 8. A description of the data correction technique is given and the main sources of systematic uncertainty are investigated. An account of the fitting procedure to evaluate the peak position of the ZEUS data distributions is reported. The same fitting technique is applied to data from TASSO and OPAL for a consistent comparison of the evolution of the peak position, $\ln(1/x_p)_{\max}$. To test the sensitivity of the peak position to the influence of coherence, data are compared to Monte Carlo models in which coherence effects can be optionally removed. The evolution of the peak position with Q is compared to TASSO and OPAL data at various $\sqrt{s}$ energies. A fit to the evolution with Q of the maxima allows a determination of Λ_{EFF}, a free parameter in the MLLA, to be made.

Contents

List of Tables

List of Tables

Chapter 1

The HERA Accelerator and ZEUS Detector

1.1 The HERA Accelerator

The Hadron Electron Ring Accelerator (HERA), located at DESY in Hamburg, is the world's first electron-proton collider. Two independent accelerators, 6.3 km in circumference, store counter-rotating beams of 820 GeV protons and 30 GeV electrons (or positrons). The beams are made to collide at zero crossing-angle in four interaction regions (figure 1.1), two of which are occupied by the ZEUS and H1 experiments. At nominal beam energies, the resulting centre-of-mass energy, $\sqrt{s}$ = 314 GeV, is equivalent to a 51 TeV electron beam colliding on a fixed proton target.

The design luminosity is 1.5×10^{31} cm^{-2}s^{-1}. To attain this luminosity both beams are bunched into 220 equidistant buckets. Of these, 210 are filled with particles and 10 are left empty for background studies. The time between bunch-crossings is 96 ns which places stringent demands on the detectors and their readout (see section 1.2).

The injection system is shown in figure 1.2. Electrons from a 500 MeV

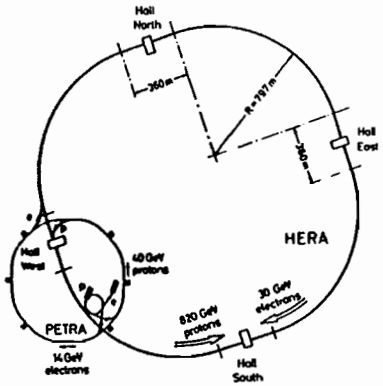

Figure 1.1: *The HERA accelerator complex.*

linear accelerator are injected into a small storage ring (PIA) where they are accumulated into a 60 mA single bunch. They are then injected into the DESY II synchrotron, accelerated to 7 GeV, and transferred to the PETRA ring. Once 70 such bunches, 28.8 m apart, are accumulated, the electrons are accelerated to 14 GeV and then injected into the HERA electron storage ring.

To obtain a proton beam, negatively charged hydrogen ions are injected into a 50 MeV linear accelerator. The H^- ions are stripped upon entering the DESY III synchrotron and captured into bunches. The protons are accelerated to 7.5 GeV and transferred to PETRA where up to 70 bunches are accelerated to 40 GeV. The protons are then injected into the HERA proton storage ring.

Superconducting magnets are used in the HERA proton ring to provide the 4.68 T field necessary to store protons of energy 820 GeV within the small circumference of HERA. In contrast, the field required to store 30 GeV electrons can be accomplished using conventional magnets. The energy lost by the electrons due to synchrotron radiation is compensated by the radiofrequency cavities, some of which are superconducting.

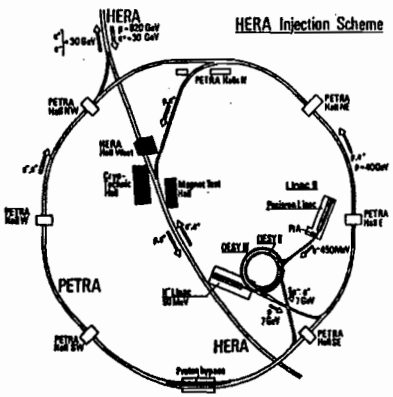

Figure 1.2: *The HERA injection system.*

In 1993 the electron beam energy was limited to 26.67 GeV since not all of the accelerator cavities were installed. Each beam consisted of 84 paired bunches with an additional 10 electron and 6 proton bunches left unpaired. An integrated luminosity of $\sim$ 1000 nb^{-1} was delivered to ZEUS, $\sim$ 600 nb^{-1} of which was recorded onto tape.

1.2 The ZEUS Detector

The general layout of the ZEUS detector is shown in figure 1.3. A fuller description is given in [1]. The detector is asymmetric to allow for the boost in the centre-of-mass of the colliding particles in the forward (proton) direction. This typically results in a greater density of high momentum tracks in the forward direction than in the rear (electron) and barrel regions. Additional instrumentation is therefore deployed in the forward direction.

The ZEUS coordinate system is defined with the $+z$-axis pointing in the proton direction, the x-axis points towards the centre of the HERA ring and y

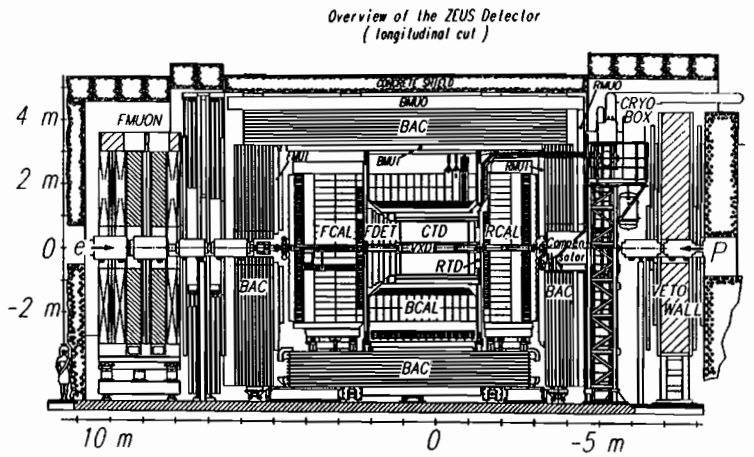

Figure 1.3: *Cross-sectional view of the ZEUS detector parallel to the beam axis.*

pointing upwards to complete the right-handed coordinate system.

Charged particles are tracked by the inner tracking system comprising a Vertex Detector (VXD) and a Central Tracking Detector (CTD) which consists of cylindrical drift chamber layers. A Forward tracking Detector (FDET) complements charged track detection in the proton direction and consists of three planar drift chambers. Sandwiched between the planar drift chambers are pairs of Transition Radiation Detectors (TRDs). In the rear direction, the inner tracking system is completed by the Rear Tracking Detector (RTD) which comprises a single planar drift chamber.

A thin superconducting solenoid surrounds the inner tracking detector and produces a magnetic field of 1.43 T allowing charged particle momentum measurements. A hermetic[1] uranium-scintillator calorimeter encloses the solenoid and inner tracking detectors. The calorimeter consists of three parts covering different regions of the polar angle θ: forward (FCAL $2.2° \leq \theta \leq 39.9°$), barrel

[1]Holes of dimension 20 cm x 20 cm are required to accommodate the beam-pipe.

(BCAL, $36.7° \leq \theta \leq 129.1°$) and rear (RCAL, $128.1° \leq \theta \leq 176.5°$). Each part is divided in depth into two parts: the electromagnetic and hadronic components.

The iron return yoke for the magnet which surrounds the calorimeter is instrumented with proportional counters. The instrumented iron serves a dual purpose: as a Backing Calorimeter (BAC) which measures any hadronic energy which leaks out of the main calorimeter, and as a muon detector. In the forward direction, iron toroids and tracking chambers reinforce muon detection (FMUON).

Downstream of the main detector in the proton direction, six measuring stations are installed in the proton ring for detecting forward scattered protons.

In the electron direction, two large scintillator VETO walls are used to reject proton-beam induced background. A set of scintillator counters (C5) partially surrounds the beam-pipe behind the rear part of the calorimeter. This serves to monitor the timing of both beams and detects background events generated upstream of the detector by the proton beam. In the same direction, two lead-scintillator calorimeters placed at $z = -34.7$ m and $z = -107$ m from the interaction point measure the luminosity and tag events with a small momentum transfer ($Q^2 \simeq 0$).

1.3 Inner Tracking Detector

The inner tracking detector is dedicated to charged particle detection in the angular range $7.5° \leq \theta \leq 170°$. The detector has been designed with the following objectives:

- to reconstruct high-momentum charged hadrons and leptons with momentum resolution $\sigma(p_T)/p_T \lesssim 0.003\, p_T$ over a wide angular range and, in particular, to discern particles within dense jets;
- to reconstruct secondary tracks from short-lived particles;

- to provide particle identification, and in particular, enhance electron identification using dE/dx information and transition radiation;
- to complement the calorimeter information and improve the resolution of the kinematic variables which characterise neutral and charged current Deep Inelastic Scattering (DIS) events;
- to provide prompt signals for use by the trigger.

1.3.1 Central Tracking Detector

The Central Tracking Detector (CTD) is a drift chamber with an active length of 2 m which covers the angular region $15° < \theta < 164°$ [2]. It consists of 72 cylindrical drift layers arranged into 9 "superlayers" as shown in figure 1.4. The odd-numbered "axial" layers have wires strung parallel to the beam (z) axis whilst the four even-numbered "stereo" layers have wires tilted by a small stereo angle of approximately $\pm 5°$. This angle is chosen such that the polar and azimuthal angular resolutions are roughly equal. Measurement of the z coordinate using these stereo wires is designed to provide a resolution of $\sigma_z = 1.4$ mm and provides increased polar angle accuracy.

The CTD has been designed for use in a high magnetic field to provide precision on the momentum measurement of the charged tracks. By design, the electron drift trajectories are rotated by a 45° Lorentz angle from the electric field direction. The wires within a superlayer are arranged azimuthally in cells, each containing eight sense wires. The maximum drift length within a cell is $\simeq 2.5$ cm and the short inter-bunch time requires a fast ($\simeq 50$ μm/ns) drift gas.

The centre of each cell is inclined 45° with respect to the radial direction. This inclination is required to ensure that the electron drift lines are perpendicular to high momentum tracks originating from the interaction region, thereby providing optimum resolution and reducing the left-right ambiguity. The inclination of cells

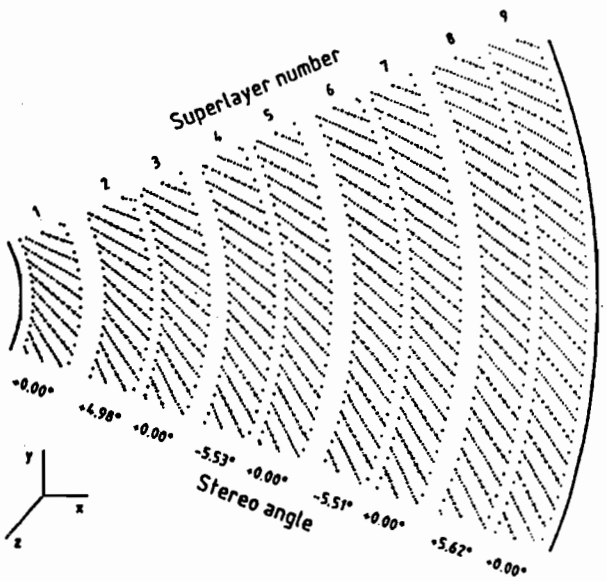

Figure 1.4: *The arrangement of wires in one octant of the CTD. Sense wires are indicated by the larger dots. Also shown is the superlayer numbering convention and the stereo angle of wires within the superlayer.*

also means that tracks always cross several sense wire planes so that at least one drift time measurement is less than 96 ns. This allows tracks from neighbouring bunch crossings to be separated.

The chamber was designed around the use of a 50:50 argon/ethane gas mixture for operation within a 1.8 T magnetic field. During 1993 operation a lower field of 1.43 T and a mixture of $Ar/CO_2/C_2H_6$ in the ratio 90/8/2 is used. This mixture offers similar values of gain, drift velocity and Lorentz angle to the design requirements.

All the CTD wires are read out by a 100 MHz Flash Analogue to Digital Converter (FADC) system. The digitisations are processed at the front-end providing a drift time and pulse height for each wire. From these, the $r\phi$ drift coordinate is designed to be extracted to a precision of $\sigma(r\phi) = 100 - 120$ μm, and dE/dx to an accuracy of $\simeq 6\%$. Wires in superlayer 1, and alternate wires in superlayers 3 and 5 have an additional readout system which provides a fast determination of the z coordinate of a track. The "z-by-timing" method compares the arrival time of signals from both ends of the chamber and obtains the z coordinate from the time difference, designed to a precision of $\sigma(zbt) \simeq 3$ cm. This is used as input to the trigger and discriminates against events caused by upstream beam-gas interactions.

At the start of the 1993 running period the CTD electronics were completed. During the running period, experience was gained operating the chamber, and the following resolutions were achieved [3]:

- $\sigma(r\phi) \sim 260$ μm
- $\sigma(zbt) \sim 4.5$ cm.

1.3.2 Vertex Detector

The Vertex Detector (VXD) is a high precision drift chamber [4] situated between the outer radius of the beam-pipe and inner wall of the CTD. It covers the angular region $8.6° < \theta < 165°$. Enclosed within a thin cylindrical carbon-fibre vessel, which has an inner and outer radius of 9.9 cm and 15.9 cm, are 120 drift cells. Each drift cell consists of twelve sense wires, 1.6 m in length, strung parallel to the beam axis. Dimethyl-ether with a trace amount of oxygen is used as a drift gas. The presently achieved resolution in $r\phi$ is 50 μm (compared to a design resolution of $30 - 40$ μm) in the central region of a cell and 150 μm near the edges.

Using hit information from the VXD in conjunction with the CTD improves the measurement of track momentum and distance of closest approach to the interaction region by a factor of 2-3 compared to the CTD measurement alone. In 1993 the achieved transverse momentum resolution of full length tracks in the CTD and VXD was $\sigma(p_T)/p_T = 0.005\,p_T \oplus 0.016$ for p_T measured in GeV.

1.3.3 Forward and Rear Tracking Detectors

Particles emitted in the forward direction ($6° < \theta < 25°$) are detected by the forward tracking system (FDET) [5]. The FDET is designed to provide accurate measurements of track parameters at small polar angles where the CTD acceptance becomes unfavourable, despite the shorter track lengths and the smaller influence of the longitudinal magnetic field than observed in the CTD. Particle identification is achieved in the FDET through the use of dE/dx and transition radiation.

Accurate track measurements are achieved by each forward tracking chamber (FTD) consisting of three planes of wires each rotated by 120° with respect to the each other. The sense wires in each plane are separated by 7 mm and alternate sense wires are staggered by 300 μm with respect to the potential wires to resolve the left-right ambiguity.

The three FTD chambers are separated by two gaps, each 210 mm in length to increase the lever-arm between track elements and therefore increase the accuracy of the track momentum measurement. In test beam studies a single-wire resolution of $120 - 130$ μm has been achieved. The resolution is dependent on drift distance and track angle. The double-track resolution achieved was found to be $\lesssim$2.4 mm.

Sandwiched between the FTD chambers are two transition radiation detector (TRD) modules which enhance particle identification. Each TRD module consists of a polypropylene fleece 70 mm thick through which CO_2 is flushed, followed

by a drift chamber which uses a mixture of xenon and CO_2. The change in refractive index between the layers of the fleece and the gas causes particles to radiate X-rays which are detected by the MWPC. The intensity of the emitted X-rays is proportional to the Lorentz factor $\gamma = E/mc^2$, of the particle. This allows particles with the same energy and differing mass to be distinguished from one another, although the effect is only really significant for separating electrons from heavier particles such as $\pi^{\pm}$s. For electrons with momentum between 1 and 30 GeV/c the design of the TRD has been optimised to produce a hadron/electron separation of 10^{-2}.

In the rear direction, tracking is completed by the rear tracking detector (RTD) covering polar angles between 160° and 170°. The RTD consists of a single chamber of identical design to the FTD.

Commissioning of the readout electronics for the forward and rear tracking detectors began toward the end of the 1993 running period. A small section of the FTD and TRD was read out in 1993 but was not used for physics analysis. The electronics are due to be completed in 1995.

1.4 Calorimeter

The design of the ZEUS calorimeter is such that it complements the tracking detectors in measuring jets with high particle densities and discriminating between leptons and hadrons. One of the main design objectives has been to ensure precise measurement of jets by providing a high energy resolution for hadrons and an equal response to hadrons and electrons. A high angular resolution and good separation for jets is necessary.

The calorimeter is needed in areas where measurements from tracking detectors are unavailable, such as the detection of neutral particles. The momentum resolution of tracking detectors worsens for high momentum particles which are deflected less by the magnetic field. Combining calorimeter and tracking compo-

nents within a detector is therefore advantageous to cover the large momentum range of particles to be measured. In addition, neutrinos can only be inferred from missing transverse energy requiring the detector to be hermetic.

These aims are achieved by using a sampling calorimeter constructed from towers which consist of alternate layers of Depleted-Uranium (DU) and plastic scintillator tiles [6]. A series of FCAL towers is shown in figure 1.5 and dimensions are given in table 1.1.

Each tower is segmented longitudinally into two parts. The inner part constitutes the electromagnetic calorimeter (EMC) with a depth of ~ 25 radiation lengths, X_0, enough to fully contain electromagnetic showers. The depth of the EMC is equivalent to 1 nuclear interaction length, λ, for hadrons. The outer part is the hadronic calorimeter (HAC) and varies in depth from 6λ, for hadrons in the forward direction to 3λ in the rear.

Each sampling layer, which is essentially repeated throughout the calorimeter, comprises a 3.3 mm thick DU plate wrapped in stainless steel foil and a 2.6 mm thick plastic scintillator slab wrapped in reflective paper. The thickness of the uranium and scintillator plates has been optimised to give equal response for electron and hadrons, through a technique known as self-compensation discussed below. The sampling layers in the tower are coupled via two wavelength shifter bars, one either side of the cell, which are in turn connected to a pair of photomultipler tubes (PMTs). The signal produced in the PMTs is proportional to the energy of the incident particle.

An equal response to electromagnetic and hadronic showers ($e/h \sim 1$) is important since hadronic showers in the calorimeter consist of an electromagnetic component from the production and decay of π^0s, ηs *etc.* When the calorimeter does not respond equally to the electromagnetic and hadronic components, the energy measurement of the hadron shower is affected.

In hadronic calorimeters which use iron or lead, a large fraction of the incident

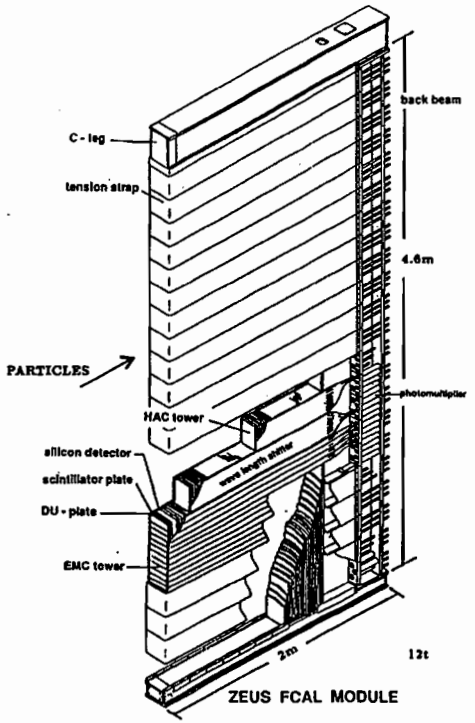

Figure 1.5: *Isometric view of an FCAL module showing the segmentation into towers. Each tower consists of alternate layers of depleted uranium and scintillator plates. The layers are coupled together by two wavelength shift bars, one on either side of the tower, which are connected to photomultiplier tubes.*

hadron's energy is lost through the release of binding energy during the breakup of the heavy nucleus. This energy is normally lost and therefore the hadronic energy resolution is relatively poor $\sigma(E)/E \sim 60\%/\sqrt{E}$.

Through the use of depleted-uranium and plastic scintillator, however, the lost binding energy can be recouped, a procedure known as self-compensation. A

Electromagnetic Calorimeter	
FCAL	5× 20 cm^2
RCAL	10× 20 cm^2
Hadronic Calorimeter	
FCAL	20× 20 cm^2
RCAL	20× 20 cm^2

Table 1.1: *Dimensions of the face of FCAL and RCAL towers.*

fraction of the shower energy results in the production of spallation neutrons which undergo elastic np scattering on free hydrogen atoms in the plastic scintillator. The recoil protons produce light in the scintillator by ionisation thereby compensating for some of the lost energy. The thickness of the uranium and scintillator plates is tuned such that the energy gained from the np scatters equals the lost binding energy. This self-compensation results in the ZEUS calorimeter having a high resolution for hadrons.

The energy resolution of the ZEUS calorimeter is

$$\frac{\sigma(E)}{E} = \frac{0.35}{\sqrt{E}} \oplus 0.02 \text{ (sampling } \oplus \text{ systematic) for hadrons; and}$$

$$\frac{\sigma(E)}{E} = \frac{0.18}{\sqrt{E}} \oplus 0.01 \text{ for electrons.}$$

The fast response time of the plastic scintillator offers an additional advantage to the experiment: the calorimeter timing can be used in the trigger to discriminate between $e-p$ collisions and the large rate of background events.

1.4.1 Hadron-Electron Separator

Gaps are provided after the 4th and 7th scintillator layers in FCAL, and after the 4th scintillator layer in BCAL and RCAL to accommodate the Hadron-Electron Separator (HES). The HES consists of one or two planar arrays of small

silicon diodes 3 cm × 3 cm in dimension. It has been designed to improve the identification of single electrons and electrons within jets compared to information from the calorimeter alone. Discrimination between electron and hadron showers is possible due to the difference between their shower profiles. The higher degree of granularity offered by the HES improves the segmentation of the calorimeter by an order of magnitude. During the 1993 running period, only part of the rear HES was read out. HES modules will be installed in FCAL and BCAL in 1994-1995.

1.4.2 Backing Calorimeter

The iron yoke provides a return path for the magnetic field produced by the solenoid. The yoke can be magnetised by up to 1.6 T by normal conducting coils to allow an independent momentum measurement of the muons traversing the barrel muon chambers. It consists of 7.3 cm thick iron plates with 3.7 cm gaps equipped with aluminium proportional tubes. The tubes and iron slabs of the yoke form the Backing Calorimeter (BAC) which is used to measure the hadronic energy leakage for those events which are not fully contained in the calorimeter. The energy resolution of the BAC is $\sigma(E)/E \sim 1.1/\sqrt{E}$ whilst a spatial resolution of about 1 mm along the length of the tubes is expected for muons.

1.5 Muon Detectors

Lepton identification is important for heavy flavour physics and the detection of new exotic processes at HERA. In addition to the electron identification provided by the tracking system and calorimeter, it is essential to have hermetic muon detectors. This is achieved by a muon detector which is divided into three sections:

Forward Muon Detector

The aim of the forward muon detector (FMUON) is to identify and provide an independent measurement of high momentum muons in the forward direction. Comparison of the momentum measurement from FMUON and the CTD allows prompt muons produced in heavy flavour decays to be distinguished from the background sources such as halo muons from proton beam-gas interactions and from the weak decay of πs and Ks.

To accomplish this, the FMUON detector consists of two iron toroids sandwiched between drift chambers planes, which measure θ, and limited streamer tube (LST) planes which provide an $r\phi$ measurement. Each toroid produces a magnetic field up to 1.7 T which produced the necessary bending power for precise momentum measurements. The momentum resolution is $\sigma(1/p)/1/p \sim 25\%$.

Barrel and Rear Momentum Detectors

The main task of the barrel and rear muon detectors (BMUON, RMUON) is to identify tracks penetrating the total calorimeter and iron yoke, and, by remeasuring their momentum and comparing this with the momentum measurement from the CTD, reduce the background of non-prompt muons. The momentum determination is performed by measuring the direction of the particle before and after the magnetised iron yoke. Each chamber consists of two double layers of LSTs equipped with wire or pad readout. The wires and the pads are orthogonal to each other so that the cross-coordinate allows a precise determination of the muon trajectory.

1.6 Small Angle Detectors

1.6.1 Luminosity Monitor

The luminosity measurement is calculated by measuring the rate of $ep \rightarrow ep\gamma$ bremsstrahlung events in two lead-scintillator calorimeters [7] situated upstream. Photons emerging from this process at angles $\theta \leq 0.5$ mrad leave the beam-pipe at a distance 92.5 m from the interaction point (IP) and hit the photon calorimeter 107 m upstream from the IP. Electrons scattered at angles $\theta \leq 6$ mrad and with energies between $0.2E_e$ and $0.9E_e$, where E_e is the electron beam energy, are deflected by the beam magnets away from the electron beam orbit and hit the electron calorimeter 34.7 m from the IP.

The luminosity monitor can be used to tag low Q^2 events where the scattered electron suffers little deflection from its original direction, and events in which a photon is emitted from the incoming electron beam.

1.7 Trigger and Data Acquisition System

Bunch crossings at HERA occur every 96 ns, equivalent to a rate of 10^7 Hz. The rate of ep events is low in comparison to the rate of background interactions. The principal sources of these interactions are synchrotron radiation from the electron beam, interactions between the proton bunch and residual gas molecules in the vacuum (beam-gas), and cosmic rays.

It is the aim of the trigger to select on-line the small fraction of interesting events from this background. The short bunch crossing time requires an innovative approach to triggering and data acquisition. A three-level trigger system is used to minimise deadtime and reduce the event rate to a few Hz.

Each detector component has its own front-end electronics, trigger and readout chain which independently transfers data to the central data acquisition

system. The detector must transfer its data to a 5 μs buffer, known as a pipeline, within 96 ns to avoid being overwritten.

Every component has its own first-level trigger (FLT), a hardware trigger which operates on a subset of the full data. It must make a relatively unsophisticated trigger decision within 5 μs of the bunch crossing. Each component transfers its trigger decision to the global first level trigger (GFLT) which makes a decision based on the global information. The GFLT is designed to reduce the trigger rate to $\simeq 1$ kHz.

If the event is accepted, it is passed to the second-level trigger (SLT). Each component can have its own SLT system which employs transputers to perform calculations on a greater proportion of the full data. Combining the results of the local transputers in the global second level trigger (GSLT) results in a further reduction of the trigger rate to 100 Hz. If the GSLT decides to keep the event the data is transferred to the Event Builder. There, data from the different components is combined into a single event record and passed to the third level trigger (TLT). The TLT analyses the event as a whole. Kinematic properties of the event can be calculated and more sophisticated rejection algorithms are applied to further reduce the event rate. The output rate, 3-5 Hz, is limited by the rate at which events can be written to tape.

1.8 Event Reconstruction

Real events from the detector are reconstructed by the ZEPHYR program[2]. The first stage of the offline reconstruction takes the raw digitisations from each component and corrects them using information gained by calibration of the detector. The corrected data can then be converted into useful quantities such as energy and position measurements from which clusters of calorimeter cells,

[2]ZEPHYR also reconstructs Monte Carlo events which have been passed through the detector simulation, MOZART.

tracks and vertices can be reconstructed. In the second stage, information from the individual components is matched: CTD tracks are linked to tracks in the VXD, FTD and RTD; global clusters in the CAL and BAC are found; and tracks are matched to calorimeter clusters.

1.8.1 Track Reconstruction

As the analysis presented in this thesis primarily relies on the detection and measurement of charged tracks, some brief details of the two packages used to reconstruct CTD and VXD tracks in 1993 are presented.

Two programs for track finding and fitting have been developed independently. The two follow different strategies in their pattern recognition and track fitting stages:

Algorithm 1 - VCTRAK

In the first approach, VCTRAK [8], the pattern recognition uses hits in the axial superlayers of the CTD and the vertex detector. The algorithm starts with hits in the outer axial superlayer of the CTD and uses a "virtual hit" at $x = y = 0$ to guide the trajectory inwards, gathering more axial hits on the way. The resulting trajectory forms a circle in the xy plane which is used for z-by-timing and stereo pattern recognition. The z-by-timing and stereo hits which superimpose on this trajectory are used to provide z information about the track so that eventually every track is described by an ideal helix from which the track momentum is determined.

To improve the fit, the track parameters at the innermost hit provided by the pattern recognition are "swum" outwards using a relatively unrefined model of the magnetic field to increase the speed of the algorithm. The ideal helix parameters and their errors are updated at each wire layer. For each measured hit, the residual distance between the swum track and the coordinate is calculated. At

the corresponding path length, the ideal helix is shifted by this residual distance and its track parameters are updated until the outermost hit is reached.

Algorithm 2 - TGTRAK

The second track finding program, TGTRAK [9], is based on the Kalman filtering technique. "Seed hits" found in the outer axial layers of the CTD are extended inwards to superlayer 1 and points are added as wire layers of the CTD are crossed. The track parameters at each step are updated using the Kalman method [10], providing an increased precision on the prediction of the next point. In the second stage, a Kalman fit to the points found in the pattern recognition phase is performed taking into account non-linear corrections to the measured drift time and the full magnetic field map. The fit starts from the innermost point from the pattern recognition and updates the measurement errors and correlations at each point. The Kalman filtering algorithm is again used to merge CTD tracks with track segments in the vertex detector.

In both algorithms, multiple Coulomb scattering in the beam-pipe and outer walls of the VXD were taken into account in the evaluation of the covariance matrix associated with each track.

Vertex Fitting

The primary vertex fit is performed in a similar way in the two packages, using only the tracks which reach superlayer 1. The first stage involves a "pre-fit" in which an initial estimate of the vertex position is calculated using a weighted mean of the track parameters at their distance of closest approach or "perigee" [11]. Tracks which contribute too much to the χ^2 of this simple fit are discarded, one by one until the fit quality is acceptable. The resulting vertex position provides the starting point for the full vertex fit which can be determined relatively quickly using this starting point and the perigee parameters. The full fit not only solves

for the final vertex position but simultaneously re-evaluates the track parameters constrained to this vertex.

Performance in 1993

While the 1993 configurations of both these tracking packages performed well, a variety of studies and visual scanning indicated that the VCTRAK package split fewer tracks, and correctly identified and assigned more tracks to the primary vertex than the TGTRAK package. Charged tracks reconstructed from the VCTRAK package have therefore been used in the central analysis presented in this thesis. The analysis was, however, repeated using tracks from the TGTRAK package as a systematic check. Full details of the analysis and the systematic uncertainties are given in chapter 8.

Chapter 2

Efficiency of the Central Tracking Detector

The Central Tracking Detector (CTD) readout electronics were completed at the start of the 1993 running period. In order to use the detector to its full potential, it must be calibrated correctly, and operated at its optimum efficiency. A method of measuring the hardware efficiency has been developed, and is discussed in this chapter.

2.1 Overview of Chamber Operation

The CTD operates as a drift chamber where the arrival times and size of the pulses are used to measure a spatial coordinate. The charge collection is determined by the trajectory of the drift, which is tuned by applied voltages to the sense wires and field shaping wires. The layout of wires within a drift cell is illustrated in figure 2.1. This arrangement allows the gain and drift field to be varied independently. The analogue signals collected on the sense wires are amplified and, if the size of the pulses exceed some threshold value, are converted to digital signals by FADCs.

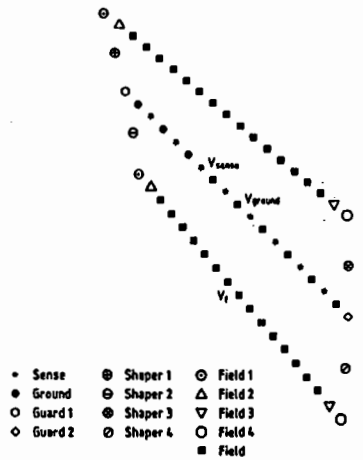

Figure 2.1: *Schematic layout of wires in a unit drift cell.*

The offline reconstruction converts the arrival time to a spatial coordinate, known as a hit, using a time-to-distance relationship. Whilst the timing measurement allows the drift distance to be measured, it does not indicate the direction of the drift. This introduces an ambiguity which can only be resolved at the pattern recognition stage of the track reconstruction. The ambiguous hits are known as ghost hits.

2.2 The Efficiency Measurement

The efficiency measurement compares the number of hits associated with a particular wire to the number of hits expected.

$$\%\text{Efficiency} = \frac{\text{Number of Measured hits}}{\text{Number of Expected hits}} \times 100\% \qquad (2.1)$$

Some form of track reconstruction is required to identify whether a charged particle should have induced a signal on the wire, and hence an associated

hit. Requiring a reconstructed track, however, results in the measured efficiency becoming a convolution of the track-finding and reconstruction efficiencies as well as the hardware efficiency. A minimum number of hits is generally required before a track is reconstructed thereby introducing a small bias to the measurement. The efficiency measurement provides a useful estimator of the "true" hardware efficiency. It does not, however, take account of inefficiencies due to, say, a high voltage failure in a sector of the detector.

Rather than use fully reconstructed tracks from the reconstruction code, portions of track reconstructed in individual superlayers, known as segments, are used as the basis for the efficiency measurement. For particles which fully traverse a superlayer, the number of expected hits is always eight. This assumption, however, is not necessarily valid for

- tracks with low transverse momentum, p_T; and
- tracks produced in upstream interactions travelling parallel to the wires which do not pass through the whole superlayer.

Reconstructed segments consist of at least four and at most eight hits to which a parabola is fitted in the $r-\phi$ plane. The segment reconstruction is not restricted to using hits in a single cell, typically using hits from two adjacent cells (see figure 2.8). Since the segments are reconstructed within individual superlayers, they are also, in general, reconstructed from the ghost hits. The segment has the following attributes, shown in figure 2.2: polar coordinates z, θ and ϕ; curvature, ρ; the azimuthal angle of the tangent to the segment, ψ; and cell number, each defined at the midpoint of the segment. The quantity $|\psi-\phi|$ is a measure of how well the segment points to the interaction point in $r-\phi$.

The wire efficiency can be determined using physics or background events. However, segments are required to satisfy the following cuts to ensure that eight hits are expected for a superlayer which is 100% efficient:

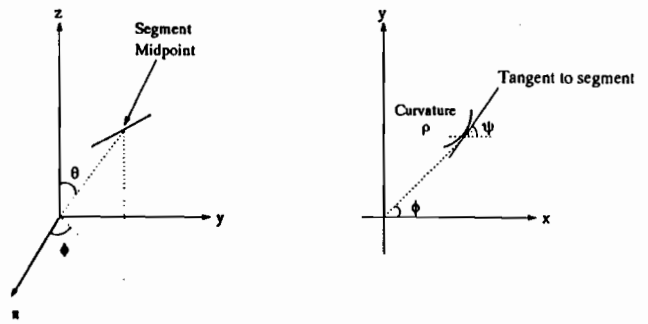

Figure 2.2: *A segment is completely described by the z, θ and ϕ coordinates; curvature, ρ, and the azimuthal angle of the tangent to the segment, ψ.*

- -90 cm $< z_{seg} <$ 90 cm - a cut to ensure that segments are wholly contained within the fiducial volume of the detector;
- $|\psi-\phi| < 0.5$ radians - a loose cut to remove ghost segments and ensure that segments point to the interaction region in the $r-\phi$ plane; and
- $\rho < 0.04$ cm^{-1} - equivalent to a cut of $p_T > 1.7$ GeV/c to remove low momentum tracks.
- at least four hits from which the segment has been reconstructed must have a residual hit-segment distance < 380 μm to remove badly reconstructed segments.

If the number of hits used by a segment is less than eight, it does not necessarily follow that wires are inefficient; it could be a feature of the segment finding algorithm. Hits are associated with the segment if they lie within a relatively narrow road defined in the segment-finder around the fitted parabola. In figure 2.3, hits which lie inside and outside this narrow road are denoted by o and • respectively. There can be hits outside this road which have produced pulses on wires but are not used in the segment fitting. Therefore, to avoid bias

from the segment reconstruction, all the hits in the two cells either side of the segment are considered, not just those associated with the segment. Then, in each wire layer, the distance between these hits and the segment is measured along a planar approximation to the drift line, *ie* the electron drift lines are approximated as straight lines as shown in figure 2.3(a), a good approximation up to distances of ~ 2 mm from the sense wire [12]. If a wire experiences multiple hits, the one closest to the reconstructed segment is considered. A new and wider road around the segment is then defined (figure 2.3(b)), the width of which was tuned using Monte Carlo events as discussed in section 2.2.1. All hits within the road are counted and so the number of measured hits is incremented in equation 2.1. If a hit does not lie within this road, the wire is considered inefficient.

2.2.1 Determination of the Roadwidth

The width of the road around the segment ultimately defines the measured efficiency. This width was tuned using a sample of DIS Monte Carlo events with $Q^2 > 100$ GeV^2 which had been passed through the detector simulation, based on the GEANT [13] package. The advantage of using such generated events is that the input efficiency of the wires can be chosen as an input parameter. To tune the width of the road, the Monte Carlo sample used had wires with 90% efficiency and an input spatial resolution in $r - \phi$ of 150 μm. This allowed the efficiency algorithm to be studied and tuned in an environment which is well understood.

The efficiency of each superlayer was measured several times, increasing the width of the road from 0.05 cm to 1.0 cm. The results are presented in table 2.1 and in figure 2.4. As the width of the road is widened, more hits are included in the efficiency measurement and so the efficiency increases until a plateau is reached at 90%. On further increasing the width, however, the measured efficiency continues to increase slightly, beyond the input value, as more hits from other tracks are included. The nominal roadwidth was taken to be 0.3 cm as this value

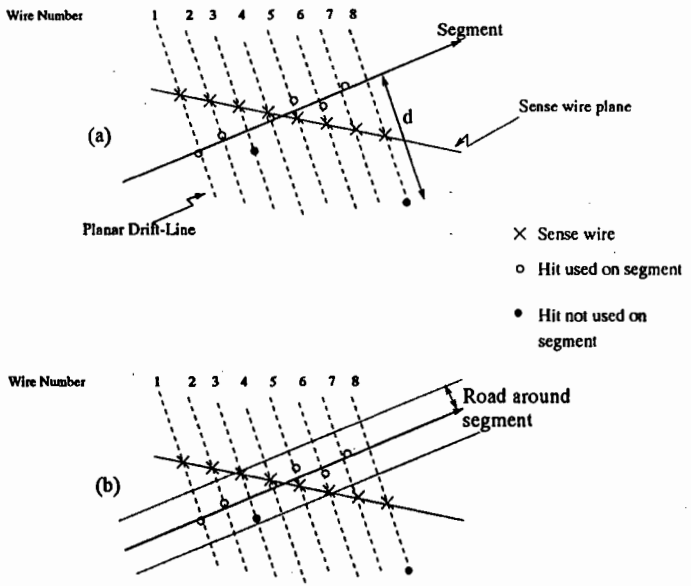

Figure 2.3: *(a) Measuring the distance between hits and the reconstructed segment forms the basis of the efficiency measurement. If only the hits which were used in the segment reconstruction were used (o), the measurement would be biased by the segment-finding algorithm. Ghost hits are not shown for clarity. (b) Hits which lie within a defined road around the segment are used to increment the number of measured hits, wire (3) in this example. If a hit lies outside this road, wire (8) in this example is defined as inefficient.*

provides a measured efficiency to within 0.8% of the input value and is just on the efficiency plateau.

Road Width (cm)	Superlayer								
	1	2	3	4	5	6	7	8	9
0.05	85.0	83.5	86.0	85.0	86.5	85.9	86.9	87.4	87.0
0.1	86.8	85.8	87.7	87.2	87.2	88.0	88.6	88.7	88.5
0.2	88.7	88.3	89.5	89.7	89.7	89.8	89.7	90.3	89.8
0.3	89.5	89.5	90.2	90.4	90.2	90.3	90.1	90.8	90.3
0.4	90.1	90.1	90.6	90.9	90.6	90.6	90.3	91.0	90.5
0.5	90.5	90.6	91.0	91.2	90.8	90.8	90.4	91.1	90.7
1.0	92.3	92.0	92.2	92.1	91.7	91.8	91.1	91.7	91.2

Table 2.1: *The measured efficiency of each superlayer as a function of roadwidth.*

2.2.2 Testing the Algorithm

The efficiency was measured using a second sample of DIS events with $Q^2 >$ 100 GeV^2 in which the input efficiency of the wires was 99%. The measured efficiency of the superlayers is shown in figure 2.5 and is compared to results from the sample with 90% wire efficiency.

The measurements from the 99% sample do not converge to the input efficiency in the same way as the 90% sample, but are typically 1-2% lower, suggesting that there may be some factor limiting the measurement.

To investigate this further, a sample of single muons was generated in which the detector was 100% efficient. The muons were generated from the nominal interaction region with randomly chosen values of θ and ϕ and momentum up to 10 GeV/c. Figure 2.6 shows that the measured superlayer efficiency is close to 100% but never quite reaches the input value.

The efficiency of the individual wire layers within each superlayer is shown in figure 2.7. The efficiency of the innermost wires[1], 1 and 2, are several percent lower than the other wires. This effect is observed to be 7-9% in superlayer 1;

[1]The wires are numbered in increasing radius from 1 → 8

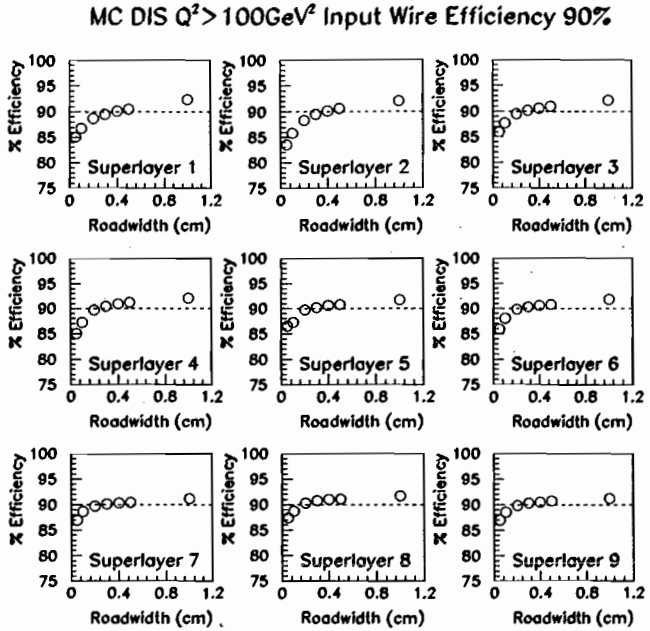

Figure 2.4: *Measured efficiency of each of the 9 superlayers plotted against roadwidth. Efficiencies* > 90% *are achieved when the road is too wide and includes hits associated with other segments.*

5-7% in superlayer 2 and 3-4% in superlayer 3. No such effect is seen in the outer superlayers, however the overall level of efficiency is ∼ 2% lower than the input value.

Visual scanning was used to identify if there was some feature of the method used which systematically degraded the measurement on these wires. Results from the scanning showed that hits are missing in cell corners and at the field-wire boundaries between cells despite the input efficiency of 100%. Figure 2.8 is a close-up view of the cells in 6 superlayers through which the single muon

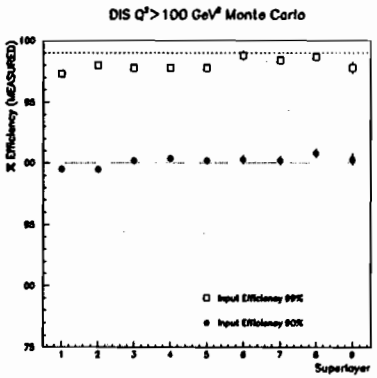

Figure 2.5: *The measured efficiency of each superlayer when the input hardware efficiency is* 90% *and* 99%.

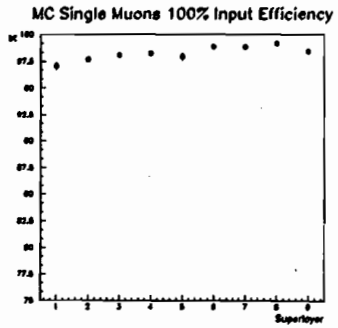

Figure 2.6: *Measured efficiency of the superlayers from Monte Carlo studies with single muons where the input efficiency was* 100%.

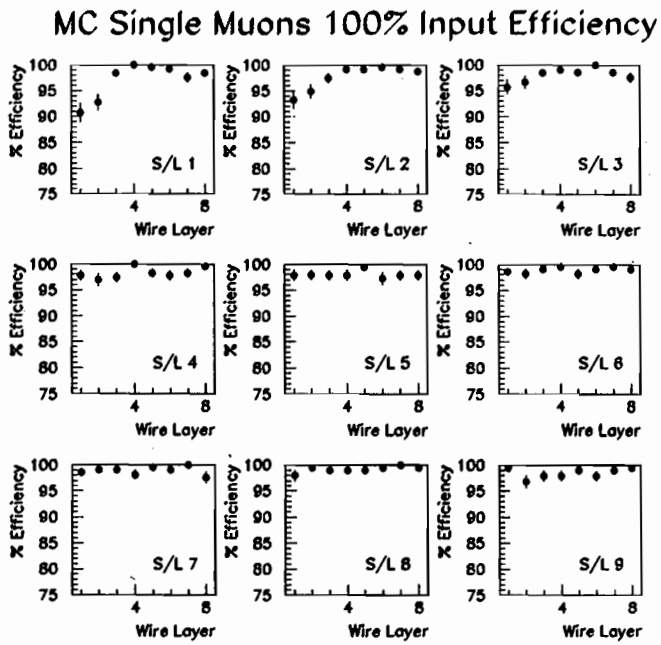

Figure 2.7: *Efficiency of each of the wire layers for generated single muons. The input efficiency was* 100% *but the measured efficiency of the inner wires in superlayers 1, 2 and 3 is significantly lower.*

passes. Hits, including the ghost hits, are indicated by the +'s. The reconstructed segments which satisfy the previously described selection criteria are indicated by the solid lines drawn from the centre of the cell in one superlayer to the centre of the next superlayer. Segments 4, 6 and 8 do not appear to line up with the others due to the stereo angle through which the wires in these superlayers are rotated. In superlayer 1, in which segment 9 has been reconstructed, the muon crosses a boundary between cells. At this boundary, the hit which should correspond to the 2^{nd} wire layer is missing. A similar observation is made in superlayer 3 in

which segment 7 is reconstructed. In superlayer 2 (segment 8), the muon deposits ionisation on seven wires ($2 \rightarrow 8$) in one cell. The same muon crosses the "acute-angled" corner of the adjacent cell and should produce a signal on wire 1. The hit, however, is missing.

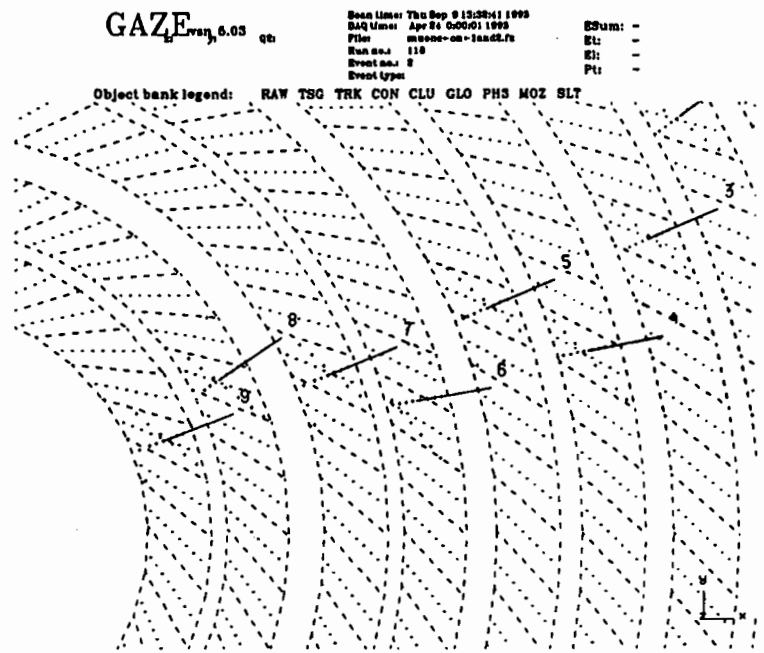

Figure 2.8: *A single muon generated by Monte Carlo with* 100% *input wire efficiency. The sense wires within the drift cells are shown, and the "real" and ghost hits are illustrated by the +s. The segments which satisfy the selection criteria are shown by the dark lines and are labelled. Hits are missing at the boundaries between cells and in cell corners.*

Similar observations are made in data as shown in figure 2.9. The cause was traced by considering the actual electron drift trajectories in superlayer 1

as shown in figure 2.10. In the acute-angled corner of the unit cell shown, the field configuration is such that there are no drift lines. Electrons produced in this region by a charged particle will tend to drift towards field wires rather than the inner sense wire. At cell boundaries, the charge produced can be shared between two cells such that the pulse produced on each wire can be too small to pass the discriminator thresholds.

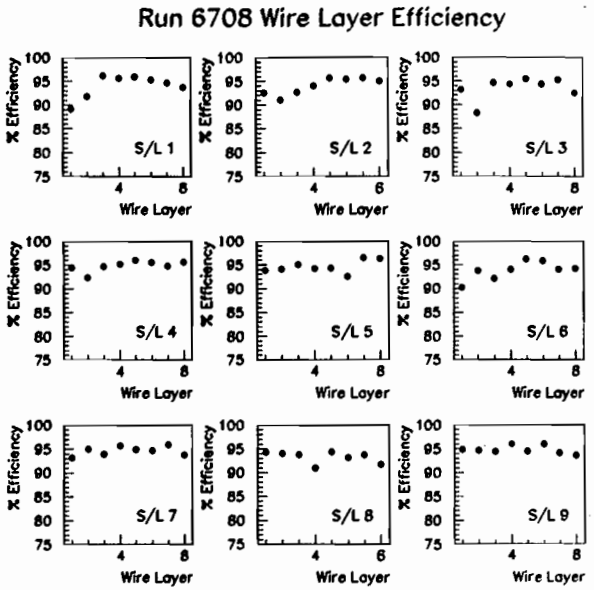

Figure 2.9: *Efficiency of the wire layers within each superlayer, measured using data. Wires 1 and 2 in superlayer 1 are seen to be inefficient compared to the others in the same superlayer.*

In the Monte Carlo, these effects are modelled in GEANT. The active volume which models the drift region does not extend into the cell corners in the inner superlayers. Particles which therefore cross this region do not produce any ionisation which in turn would simulate a pulse on the sense wires. Additionally,

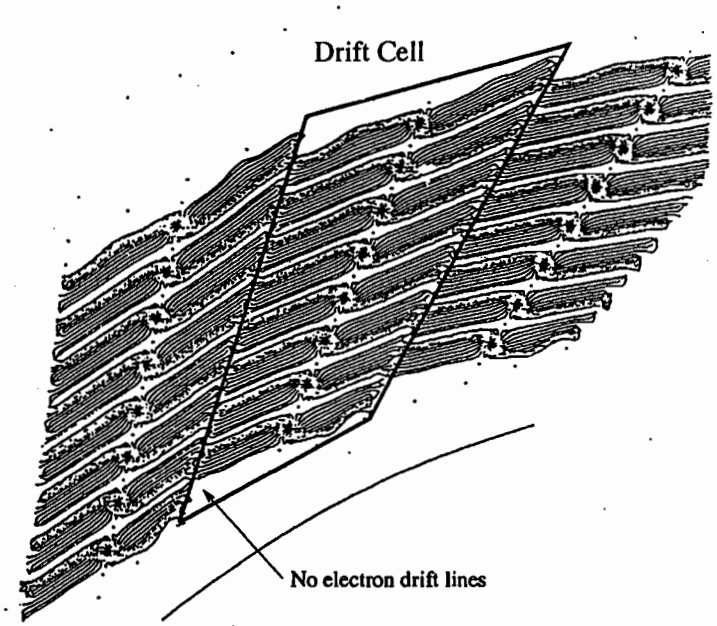

Figure 2.10: *Electron drift trajectories in a unit drift cell in superlayer 1. There are no drift lines in the acute-angled corner of the cell which reduces the efficiency of wire 1.*

at the boundaries between cells, there are discontinuities between these active volumes through which the particle can slip without any simulation of ionisation.

The cell-corner effects are not as important in the outer superlayers. Figure 2.8 shows that as the radius of the superlayers increase, the inter-cell boundaries approach parallel lines rather than the tapered shape which cells in superlayer 1 and 2 possess. This, in turn, results in the field lines filling the "field free" region which exists in superlayers 1 and 2.

2.3 Efficiency During Data Taking

Since the efficiency algorithm has been shown to be sensitive to different input hardware efficiencies simulated in the Monte Carlo, it was applied to data in order to determine the optimum conditions with which the chamber should be operated.

2.3.1 Sense Wire Voltage

The voltage applied to the sense wires controls the gain and therefore the size of pulses produced on the sense wires. The voltage has to be tuned to provide the optimum pulse size. If the voltage is too low, the size of the pulses produced may not exceed the threshold level which has been set to reduce the amount of measurable noise. Running at too high a voltage increases the risk of discharges which can reduce the lifetime of the chamber. In addition, the pulses can be too large for the FADC system to measure their height. This would distort the shape of the pulses which would in turn degrade the measurement of the arrival time of the pulse and dE/dx.

The efficiency of the chamber was measured in three consecutive runs in which the voltage on the sense wires was changed. During these runs, the discriminator thresholds were kept constant and the variation in atmospheric pressure, which has been observed to affect the size of pulses, was negligible. Since the corresponding field voltage was not changed, the electric field configuration within the drift cell was not optimised for the different voltages.

Figure 2.11 presents the results from running at 94%, 96% and 98% of the design sense wire voltage. The efficiency measurement is observed to increase by 1-4% as the voltage is raised from 94% to 98%. At 94% and 96% superlayers 1, 3 and 5 which have both FADC and z-by-timing readout are typically 2% more efficient. This effect which is removed when the voltage is raised to 98% suggesting that the FADC system may be inefficient in comparison.

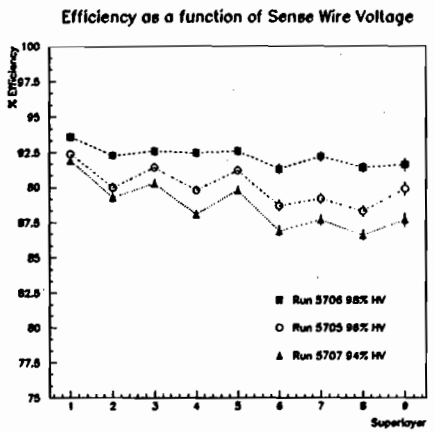

Figure 2.11: *Efficiency of each of the 9 superlayers plotted against superlayer number. The results are from 3 luminosity runs taken with different sense wire high voltage settings.*

2.3.2 Relative Efficiency of FADC System

In order to further investigate the difference between the efficiency of the superlayers which have FADC-only readout and combined FADC and z-by-timing readout, segments were reconstructed from

- hits from the FADC system only; and
- hits from both readout systems.

The efficiency was measured for a run in which the high voltage was set to 96%. The results, shown in figure 2.12, confirm that the increased efficiency in superlayers 1, 3 and 5 is due to additional hits found only by the z system which has its own discriminator threshold levels, independent of the FADC system.

At 98% high voltage, the rate of larger pulses which pass the FADC discriminator thresholds has increased such that the efficiency of the FADC-only and

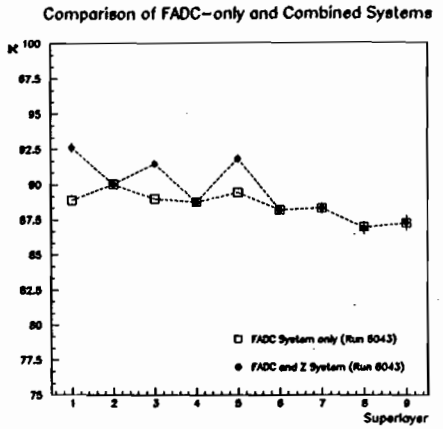

Figure 2.12: *Efficiency calculated using the combined z and FADC readout systems, and the FADC-only system. A systematically higher efficiency was observed in the superlayers instrumented with both z and FADC electronics.*

combined systems becomes comparable.

2.3.3 FADC Discriminator Thresholds

The previous results suggested that the FADC discriminator thresholds were too high, making superlayers with FADC-only readout inefficient in comparison to those with combined readout. Analysis of the pulse sizes for various discriminator thresholds suggested that the threshold level could be lowered to half its value without any substantial increase in the level of noise. Successive runs were taken with the following operating conditions so that the effects of changing the thresholds and high voltage could be monitored separately.

- 96% high voltage and "high" discriminator thresholds (15 counts);
- 96% high voltage and "low" discriminator thresholds (8 counts); and

- 98% high voltage and "low" thresholds.

In addition to changing the sense wire voltage, the field wire voltage was tuned to optimise the drift. The measured efficiencies shown in figure 2.13 indicate that on lowering the thresholds, the discrepancy between the superlayer efficiencies of the FADC-only and the combined readout system lessens. The overall efficiency is higher compared to the run with higher threshold levels as more pulses are measurable. Finally, increasing the gain raises the overall efficiency by a further 3% and provides an approximately constant response across the nine superlayers. This provided the optimum high voltage and discriminator thresholds for operation during 1993.

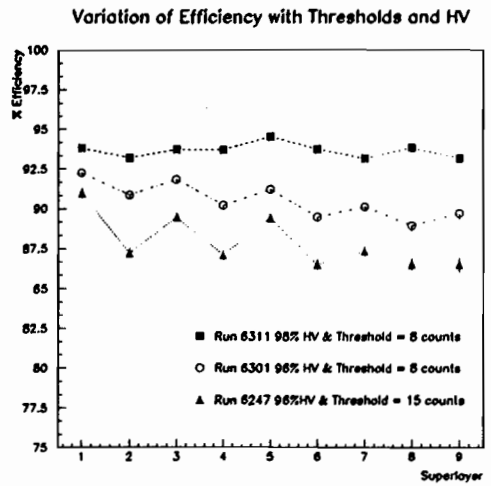

Figure 2.13: *The effect of changing the discriminator thresholds and the high voltage on the measured superlayer efficiency.*

2.4 CTD Efficiency during 1993

The efficiency was monitored throughout the 1993 running period and is plotted as a function of run number in figure 2.14. Throughout the majority of the running period, the chamber was operated at 98% high voltage and with the lower discriminator threshold setting. The mean efficiency of the chamber was typically 93.5-95% with fluctuations mainly due to variations in atmospheric pressure, as shown in figure 2.15. During periods where the rate of beam-induced background increased above an acceptable level and caused the chamber to trip frequently, the voltage was lowered to the 96% setting and the efficiency of the chamber subsequently dropped.

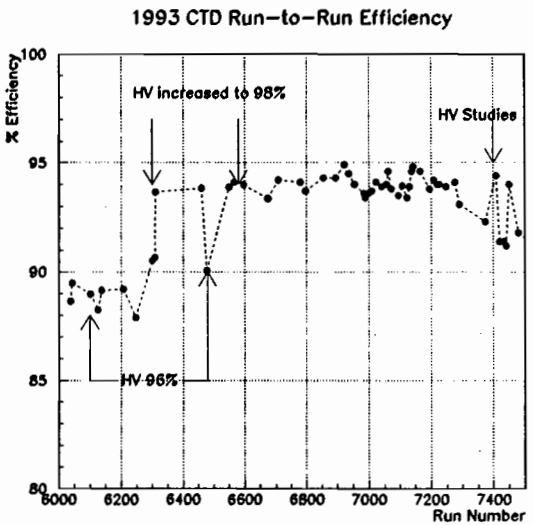

Figure 2.14: *Efficiency of the CTD as a function of run number as monitored throughout the 1993 running period.*

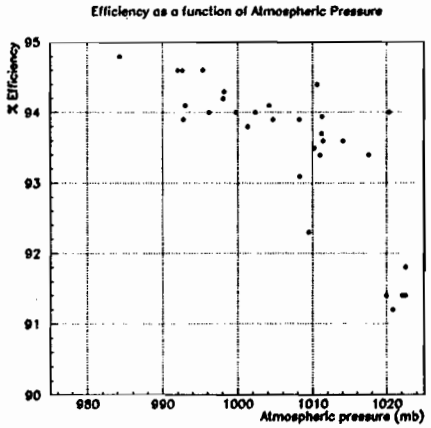

Figure 2.15: *Efficiency of the CTD as a function of atmospheric pressure.*

2.5 Summary

An algorithm to measure the relative hardware efficiency, designed to provide an estimate of the absolute value, has been developed and tested using Monte Carlo events in which the hardware efficiency is an input parameter. The measured efficiency reproduces the input efficiency. The maximum achievable efficiency is limited by hit losses at cell boundaries and in cell corners due to field-shaping effects. The measurement was used to define the CTD sense wire voltage, and FADC discriminator threshold level for the majority of the 1993 running period. Monitoring this efficiency throughout the year with these conditions has indicated that the efficiency is typically between 93-95% with fluctuations predominantly due to atmospheric pressure.

Chapter 3

Reconstruction of Deep Inelastic Scattering Events

In this chapter the kinematic quantities by which DIS events are characterised are introduced. A variety of experimental methods can be used to calculate these quantities; however, relevant formulae are given for the main reconstruction methods used at ZEUS. Emphasis is given to the accuracy of the so-called "double-angle method" which is adopted in the analysis presented in this thesis.

3.1 Kinematics of DIS

In DIS the incoming electron couples to the electroweak current which probes the structure of the proton. The exchanged boson is a virtual γ or Z^0 in neutral current, or a $W^{\pm}$ in charged current events. The mediating particle transfers momentum between the electron and proton. At sufficiently large values of momentum transfer, the current can resolve the proton constituents such that HERA is an electron-parton collider. The current then interacts with a quasi-free quark within the proton while the remnant constituents continue unperturbed.

The basic neutral current DIS process is illustrated in figure 3.1 where k and

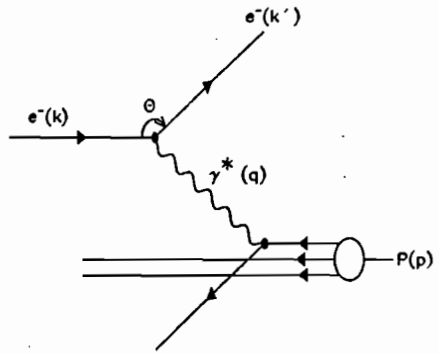

Figure 3.1: *Lowest order inelastic electron-proton scattering.*

k' are the four-vectors of the incident and scattered electron, and p is the four-momentum of the initial proton. The polar angle through which the electron is scattered, θ, is measured with respect to the proton direction.

Neglecting the masses of the electron and proton, a good approximation at HERA energies, the total centre of momentum energy squared is given by

$$s = (k + p)^2 \simeq 4E_e E_P \tag{3.1}$$

where E_e and E_P are the electron and proton beam energies.

The exchanged boson has four-momentum $q = k - k'$, and the momentum transfer, Q^2, is defined as

$$Q^2 = -q^2 = -(k - k')^2 \tag{3.2}$$

which describes the resolution with which the exchanged photon probes the structure of the proton. Q^2 can have values between 0 and s.

Two independent Lorentz invariant variables are used to describe the scattering process. The dimensionless variables x and y are defined as

$$x = \frac{-q^2}{2p.q} \tag{3.3}$$

$$y = \frac{p.q}{p.k}, \quad 0 \leq (x,y) \leq 1 \tag{3.4}$$

where x can be interpreted as the momentum fraction of the proton carried by the struck quark in the massless limit. y is the relative energy transferred from the electron to the proton in the proton rest frame.

A useful relationship between the kinematic variables is

$$Q^2 = xys \tag{3.5}$$

which demonstrates that only two independent variables need be known for the $2 \rightarrow 2$ scattering process to be fully described.

HERA extends the kinematic range accessed by previous fixed target experiments. The centre of momentum energy, $\sqrt{s}$, at HERA is 314 GeV at nominal beam energies, a factor of 10 greater than that achieved at the E665 experiment at Fermilab. This opens up the previously unexplored regions of high Q^2 and low x, extending the measurement by a factor of ~ 100 in both directions.

3.2 Reconstruction of Kinematic Variables

The kinematic variables x and Q^2 can be expressed in terms of two independent measurable quantities: a choice of energy and/or angle of the scattered lepton (E'_e, θ) and/or hadronic jet (F, γ_h) as shown in figure 3.2. The accuracy of these measured quantities is determined by the energy and angular resolution of the calorimeter.

E_e	Energy of incoming electron beam (26.67 GeV)
E_p	Energy of incoming proton beam (820 GeV)
E'_e	Energy of scattered electron
θ	Polar angle of scattered electron
F	Energy of hadronic system (struck quark)
γ_h	Polar angle of hadronic system (struck quark)

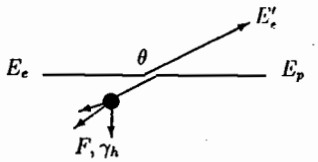

Figure 3.2: *Definition of E'_e, θ, F and γ_h.*

3.2.1 Reconstruction Methods

A precise determination of x and Q^2 is of importance to calculate the correct Lorentz transformation necessary to boost to the Breit frame. As discussed in chapter 7, the accuracy with which the kinematic variables can be calculated limits the resolution of the scaled momentum measurements presented in this thesis.

Electron Method

The conventional way to determine (x, Q^2) is from the energy and angle of the scattered electron. The kinematics are given by:

$$Q^2_{elec} = 2E_e E'_e (1 + \cos\theta) \tag{3.6}$$

$$x_{elec} = \frac{E_e}{E_p}\left(\frac{E'_e \cos^2(\frac{\theta}{2})}{E_e - E'_e \sin^2(\frac{\theta}{2})}\right) \tag{3.7}$$

$$y_{elec} = 1 - \frac{E'_e}{E_e}\sin^2(\frac{\theta}{2}) \tag{3.8}$$

Contours of constant electron energy and angle are shown on the (x, Q^2) plane in figures 3.3(a) and (b). For a given resolution on the measured energy E'_e and angle θ_e, the density of the lines indicates the relative accuracy with which (x, Q^2) can be measured: for contours with a relatively large separation, a small error on

the measured quantity E'_e or θ corresponds to a large error on the measured (x, Q^2) using this method. Also indicated on figure 3.3(b) are the selected (x, Q^2) analysis intervals (discussed in chapter 6) and dotted lines corresponding to $y = 0.04$ and the kinematic limit, $y = 1$.

Jacquet-Blondel Method

The Jacquet-Blondel method uses the hadronic energy, F, and angle, γ_h, shown in figure 3.3(c) and (d) to reconstruct the kinematic variables. This method has to be used when the scattered lepton is not detected, as in charged current DIS and photoproduction events. The four-momentum, W, which describes the sum of all outgoing hadrons from the quark and remnant jet is given by

$$W = \sum_h (E_h, p_{x_h}, p_{y_h}, p_{z_h}) = p + q \tag{3.9}$$

leading to

$$y_{JB} = \frac{\sum_h (E_h - p_{z_h})}{2E_e} = \frac{F(1 - \cos\gamma_h)}{2E_e} \tag{3.10}$$

from which expression for Q^2_{JB} and x_{JB} follow:

$$Q^2_{JB} = \frac{(\sum_h p^2_{x_h}) + (\sum_h p^2_{y_h})}{1 - y_{JB}} = \frac{F^2 \sin^2\gamma_h^2}{1 - y_{JB}} \tag{3.11}$$

$$x_{JB} = \frac{Q^2_{JB}}{s y_{JB}} \tag{3.12}$$

The direction of the hadronic energy flow (struck quark in the quark parton model) is derived from equations 3.10 and 3.11 as

$$\cos\gamma_h = \frac{Q^2_{JB}(1 - y_{JB}) - 4E_e^2 y^2_{JB}}{Q^2_{JB}(1 - y_{JB}) + 4E_e^2 y^2_{JB}} \tag{3.13}$$

which is experimentally determined by summing over calorimeter energy cells, except those associated with the scattered electron, using

$$\cos\gamma_h = \frac{(\sum_h p_{x_h})^2 + (\sum_h p_{y_h})^2 - (\sum_h (E_h - p_{z_h}))^2}{(\sum p_{x_h})^2 + (\sum p_{y_h})^2 + (\sum_h (E_h - p_{z_h}))^2} \tag{3.14}$$

The cancellation of the energy terms in equation 3.14 makes $\cos\gamma_h$ insensitive to any imperfections in the calorimeter energy scale.

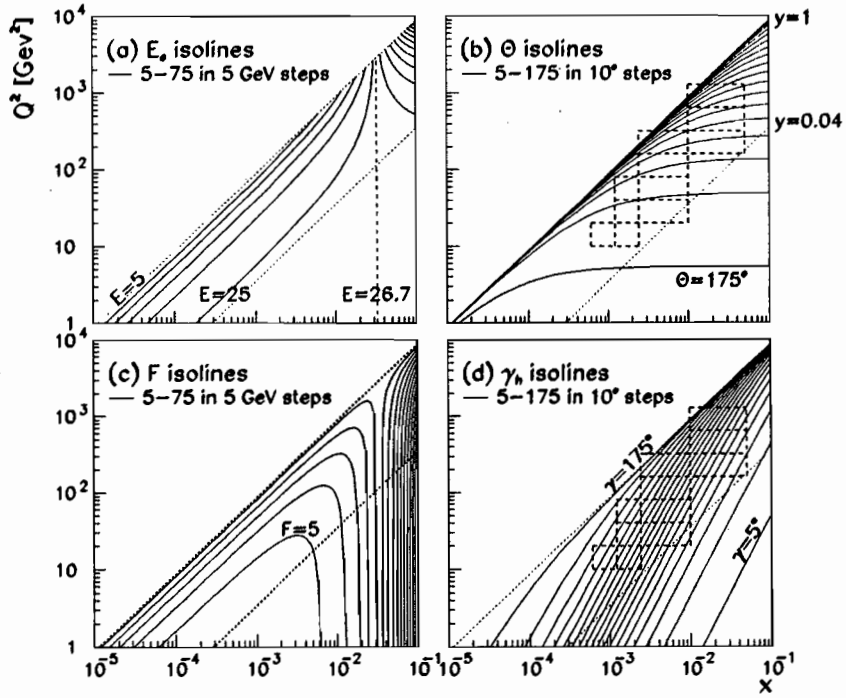

Figure 3.3: *Lines of constant a) outgoing electron energy in 5 GeV steps b) outgoing electron angle in 5° steps c) hadronic system energy and d) hadronic system angle in the (x, Q^2) plane.*

3.2.2 Double-Angle Method

The optimum x and Q^2 resolution over the majority of the kinematic plane [14] is provided by the double-angle method which uses the scattered electron angle

θ and the hadronic angle γ_h shown below. Similarly, studies showed that this reconstruction method provides the most accurate determination of the boost to the Breit frame in comparison to the other methods. Since x_{DA} and Q^2_{DA} have been used in the central analysis discussed in this thesis, the method is discussed here in more detail.

The kinematic variables are given by

$$Q^2_{DA} = \frac{4E_e^2 \sin\gamma_h(1+\cos\theta)}{\sin\gamma_h + \sin\theta - \sin(\theta+\gamma_h)} \quad (3.15)$$

$$x_{DA} = \frac{E_e}{E_p}\frac{\sin\gamma_h + \sin\theta + \sin(\theta+\gamma_h)}{\sin\gamma_h + \sin\theta - \sin(\theta+\gamma_h)} \quad (3.16)$$

$$y_{DA} = \frac{\sin\theta(1-\cos\gamma_h)}{\sin\gamma_h + \sin\theta - \sin(\theta+\gamma_h)} \quad (3.17)$$

The relative errors on x and Q^2 for this reconstruction method are

$$\left.\frac{\partial Q^2}{Q^2}\right|_{\gamma_h} = \frac{y-2}{\sin\theta}d\theta \qquad \left.\frac{\partial Q^2}{Q^2}\right|_{\theta} = \frac{-y}{\sin\gamma_h}d\gamma_h$$
$$\left.\frac{\partial x}{x}\right|_{\gamma_h} = \frac{-1}{\sin\theta}d\theta \qquad \left.\frac{\partial x}{x}\right|_{\theta} = \frac{-1}{\sin\gamma_h}d\gamma_h \quad (3.18)$$

Equation 3.13 contains terms in y_{JB}, the measurement of which is distorted by uranium noise in the calorimeter at low $y_{JB} < 0.02$. The resolution of γ_h (equivalent to $d\gamma_h$ in equation 3.18) is therefore expected to decrease as y decreases. At $y = 0.14$ the γ_h resolution is $\simeq 8.5°$ and degrades to $\simeq 15.5°$ at $y = 0.02$. In the analysis described in this thesis, a cut is imposed on the data at $y_{JB} = 0.04$ to improve the reconstruction of the hadronic variables (see chapter 6). Above this y_{JB} cut the resolution of γ_h is better than 13°.

The θ resolution was measured to be better than 0.5° in the analysis regions shown in figure 3.3(b). Beyond this analysis region, at very high electron angles the positional reconstruction of the electron is observed to degrade due to shower losses in the rear beam-pipe. The reconstructed position of the electromagnetic shower is systematically shifted towards larger distances from the beam-pipe, equivalent to smaller θ values. In the analysis presented, this is avoided by

imposing a minimum value of Q^2 and a minimum distance from the beam-pipe beyond which leakage of the shower is negligible (see chapter 6).

The formulae in equation 3.18 show that at very small or very large scattering angles for the electron or hadron flow the resolution in x_{DA} and Q^2_{DA} degrades. From figure 3.3(b) and (d), at low y the value of θ is high and γ_h is low making this region problematic for the determination of the variables. In contrast to the Q^2 resolution which is enhanced by the y term in the numerator of equation 3.18, the x resolution is expected to be particularly poor at low y.

3.2.3 Resolution of Double-Angle (x, Q^2)

To measure the resolution on x and Q^2 due to the double-angle reconstruction, Monte Carlo events were generated as discussed in chapter 5. The events were subject to the same series of kinematic cuts applied to the real data (see chapter 6) to obtain a fiducial sample of well-reconstructed DIS events.

The resolution was measured in terms of Δx and ΔQ^2 given by

$$\Delta x = \frac{x_{DA} - x_{gen}}{x_{DA}} \quad \text{and} \quad \Delta Q^2 = \frac{Q^2_{DA} - Q^2_{gen}}{Q^2_{DA}} \quad (3.19)$$

where x_{gen} and Q^2_{gen} are the generated values.

Figure 3.4 shows the Δx distributions in the eleven analysis regions. The x and Q^2 range explored by these regions is indicated at the bottom and right-hand side of the figure, and are the same intervals shown on figures 3.3(b) and (d). In each plot the Δx range shown is from -1 to 1. Each plot indicates the RMS of the distribution.

The Δx resolution is observed to improve as Q^2 increases. The resolution is enhanced by the $1/\sin\theta$ and $1/\sin\gamma_h$ terms in equation 3.18. The selection cuts and choice of analysis bins exclude the regions of phase space where the scattered electron and hadronic angles have very high or very low values. A further improvement is noted at high y where the γ_h resolution improves. The resolution improves from $\simeq 40\%$ at low (x, Q^2) to $\simeq 15\%$ at high (x, Q^2).

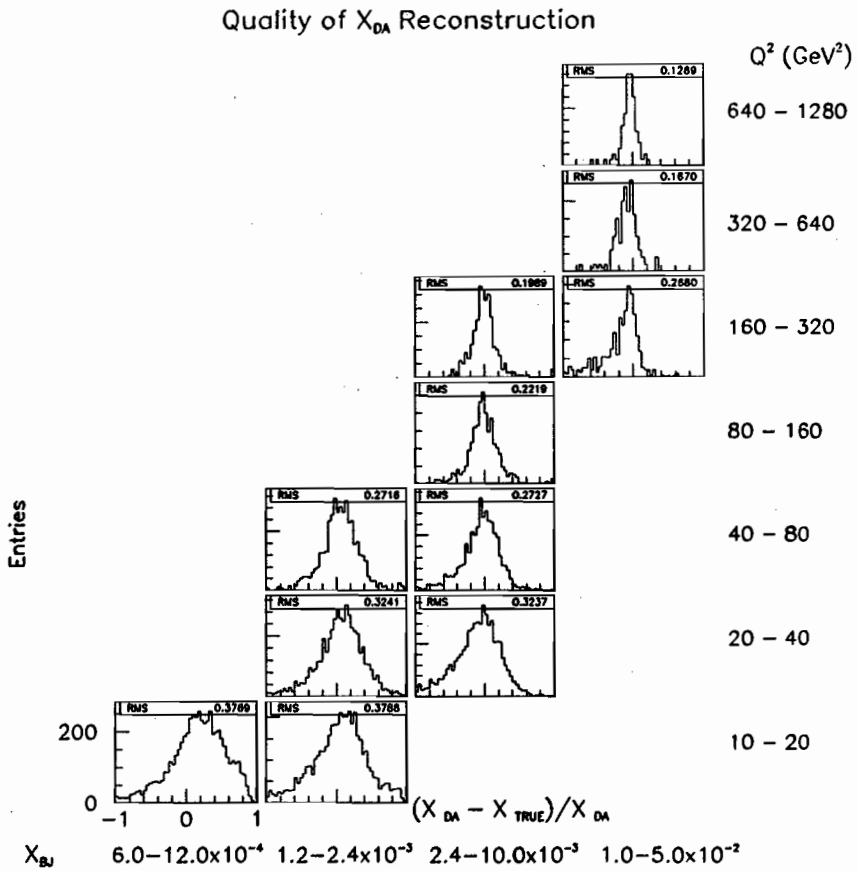

Figure 3.4: *Resolution of x_{DA} in eleven analysis regions on the x,Q^2 plane.*

In the low (x, Q^2) region, $\Delta x > 0$ indicating that the reconstructed value of x is greater than the generated value. Furthermore, events were observed to migrate from very low values of x, outside the specified analysis range, into the analysis bin due to the relatively poor x reconstruction in this region.

The ΔQ^2 distribution is shown in figure 3.5 and is generally constant at $\sim 15\%$

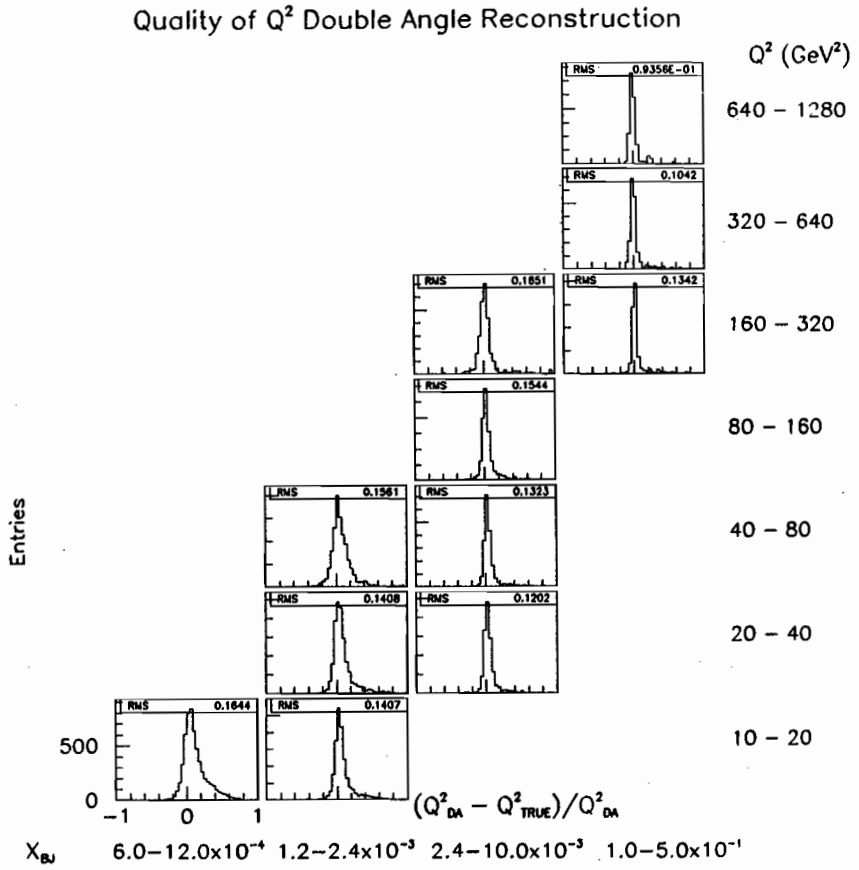

Figure 3.5: *Resolution of Q^2_{DA} in eleven analysis regions on the x,Q^2 plane.*

over the selected region of phase space. In fixed regions of x, there is a systematic tendency for the ΔQ^2 resolution to improve at lower values of Q^2. Although the $1/\sin\theta$ and $1/\sin\gamma_h$ terms increase in this region, the y term in the numerator of equation 3.18 enhances the Q^2 resolution.

Chapter 4

Theoretical Background

4.1 The Naïve Quark Parton Model

During the accumulation of data on baryon and meson resonances in the 1960's, regularities or patterns were noted among the observed hadron states. In 1961 Gell-Mann introduced a scheme, known as the Eightfold Way, which allowed baryons and mesons with the same spin to be grouped according to their charge and strangeness. The eight lightest spin 1/2 baryons including the proton and neutron form the baryon octet, whilst ten spin 3/2 baryons were predicted to comprise the baryon decuplet. At the time, however, only 9 of these baryon decuplet states had been observed. Three years after it had been predicted, the Ω^- was observed, heralding the success of this model.

In 1964, Gell-Mann and Zweig extended the model by proposing that the hadrons were composed of a new group of spin 1/2 particles called quarks which carry a fractional electric charge and transform according to $SU(3)_{\text{flavour}}$. The quarks were predicted to appear as three species: up (u), down (d) and strange (s) which could be combined to reproduce the structure of the known baryon and meson multiplets. As the Ω^-, Δ^- and Δ^{++} in the decuplet comprise of three like quarks each with spin 1/2, they appear to violate the Pauli principle.

An additional degree of freedom was therefore assigned to the quarks known as colour, of which there are three values, making the wavefunction of these baryons antisymmetric as required. As there was no evidence to suggest that colour is a measurable property of hadrons, the hadrons were postulated to be built from colourless combinations of quarks.

DIS experiments at SLAC in the late 1960's provided the first evidence that nucleons are composed of pointlike constituents, known as partons. The structure of the nucleons can be examined using a virtual photon with sufficiently high Q^2, equivalent to decreasing the spatial resolution within the proton. The proton structure function, $F_2(x, Q^2)$ was observed to be independent of Q^2 at a given value of x [15]. This scaling behaviour, predicted by Bjorken, was interpreted as evidence for the existence of the pointlike partons.

The differential cross-section for the DIS process can be written in terms of two dimensionless structure functions, $F_1(x, Q^2)$ and $F_2(x, Q^2)$

$$\frac{d^2\sigma}{dQ^2dx} = \frac{4\pi\alpha^2}{xQ^4}\left[(1-y)F_2(x,Q^2) + y^2xF_1(x,Q^2)\right] \tag{4.1}$$

Callan and Gross suggested that the structure functions should be related [16]:

$$2x\,F_1(x) = F_2(x) \tag{4.2}$$

reflecting the hypothesis that the charged constituents of the proton are spin 1/2 particles. This was later confirmed experimentally [17].

Evidence that the partons carry fractional electric charge came from the comparison of F_2 measured in neutrino-nucleon scattering in bubble chamber experiments and from electron-nucleon scattering which confirmed that $F_2^{\nu N} \simeq \frac{18}{5}F_2^{eN}$ as predicted for fractional quark charges [18].

The experimental verification of Bjorken scaling, the Callan-Gross relation and the fractional electric charges in DIS provided compelling evidence that the partons within the proton are quarks. In a frame where the momentum of the proton is much greater than its mass, relativistic time dilation slows down the rate

at which the partons within the proton interact with one another such that during the short time that the virtual photon interacts with the parton, $t_{int} \sim \hbar/Q$, it is essentially a free particle within the proton so that deep inelastic $e-p$ scattering is equivalent to elastic $e-$ parton scattering.

The Quark Parton Model (QPM) was developed on the basis of these results. In this model the proton consists of three non-interacting valence quarks (uud) accompanied by many quark-antiquark pairs, mainly $u\bar{u}$, $d\bar{d}$ and $s\bar{s}$ known as sea-quarks. In the QPM each parton i carries a momentum fraction x_i of the proton's momentum and is assumed to be massless. The structure function, F_2, is then interpreted as

$$F_2(x) = \sum_i e_i^2 x f_i(x) \tag{4.3}$$

where $f_i(x)$ is the probability that parton i with electric charge e_i carries a fraction x of the proton's momentum.

4.2 QCD Improved QPM

Summing over the momenta of all the partons in the proton, $\int F_2\,dx$, directly reveals the momentum fraction of the proton carried by the charged partons. In the QPM where the proton consists solely of charged quarks $\int F_2\,dx = 1$. Measurement of $\int F_2\,dx$, however, indicated that the quarks account for only $\sim 50\%$ of the total momentum of the proton. The remaining fraction is carried by charge-neutral, spin 1 particles called gluons which are responsible for mediating the strong force which binds the quarks within the proton. The gluons produce the many quark-antiquark pairs, requiring the QPM picture to be modified. The presence of gluons introduces a logarithmic dependence on Q^2 to $F_2(x, Q^2)$ which was experimentally observed at SLAC [19]. This violation of Bjorken scaling is a major prediction of Quantum Chromodynamics (QCD), the theory which describes the interactions between quarks and gluons.

The QPM completely ignores the role of gluons as carriers of the strong force associated with the coloured quarks. In particular any interaction between the quarks and gluons is neglected. Such interactions allow for the possibility that the quark may radiate a gluon before or after being struck by the virtual photon $\gamma^* q \rightarrow qg$. Another possible interaction, neglected in the QPM, is that a gluon in the proton can contribute to DIS by producing a $q\bar{q}$ pair one of which couples to the virtual boson $\gamma^* g \rightarrow q\bar{q}$. These leading-order processes are known as QCD Compton (QCDC) and Boson-Gluon Fusion (BGF) respectively (figures 4.1(a) and (b)) and their matrix elements have been calculated exactly.

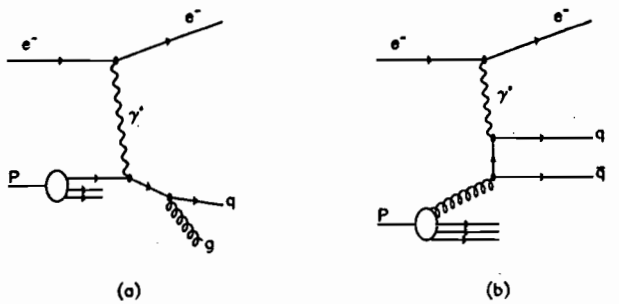

Figure 4.1: *Feynman Diagrams for the $\mathcal{O}(\alpha_s)$ processes. (a) Final-state QCD Compton and (b) Boson-Gluon Fusion*

The major difference between electromagnetic and strong interactions is that the gluons themselves carry colour charge, and so they can interact with other gluons. The fact that gluons carry approximately twice as much colour charge as the quarks makes gluon-gluon interactions prevalent. This leads to a "running" coupling constant, α_s, which decreases at short distances such that the partons within the nucleon essentially behave as free, non-interacting particles. In this

regime in leading-order processes, α_s is given by

$$\alpha_s(Q^2) = \frac{12\pi}{(33 - 2N_f)\ln(Q^2/\Lambda^2_{\rm QCD})} \tag{4.4}$$

where N_f is the number of quark flavours. $\Lambda^2_{\rm QCD}$ can be thought of as the value of Q^2 which marks the boundary between the world of quarks and gluons where perturbative QCD calculations are valid and that of the observed hadrons. At $Q \lesssim \Lambda \sim 100 - 400$ MeV the coupling is so strong that non-perturbative methods need to be applied.

As $Q^2 \to \infty$, $\alpha_s \to 0$, a property known as asymptotic freedom. This allows interactions involving coloured partons to be calculated at large momentum transfers, where α_s is small, using perturbative techniques. Perturbative QCD calculations are therefore a series of approximations involving logarithmic and double-logarithmic terms in (Q^2/Λ^2). Due to the running of α_s, the next-to-leading-order corrections are smaller than the leading-order corrections if the momentum transfer is large.

When a quark is knocked out of the proton as a result of a high energy collision, it rapidly moves away from the remnant coloured quarks. QCD predicts that the quark is accompanied by a cloud of virtual partons. The 4-momentum of the struck quark can be split between a quark and a gluon: the quark having momentum zp and the gluon the remaining $(1 - z)p$. In the leading-logarithmic approximation (LLA), valid in the relativistic limit, the probability for this is proportional to

$$\alpha_s(Q^2) P_{q \to qg}(z) \tag{4.5}$$

where

$$P_{q \to qg}(z) = \frac{4}{3}\left(\frac{1 + z^2}{1 - z}\right) \tag{4.6}$$

$P_{q \to qg}(z)$ describes the probability that a quark of 4-momentum zp will be found in what started as a quark of momentum p. Equation 4.6 is one of the Altarelli-Parisi Splitting functions [20] which also describe the variation with Q^2 of finding

a gluon in a gluon, or a quark in a gluon. These functions reflect the underlying processes such as $q \to gq, g \to q\bar{q}$ and $g \to gg$ *ie* the way in which high momentum quarks and gluons become quarks and gluons of lower momentum via splitting and radiating. The functions govern the development in time of the decelerating struck quark and the shower of partons it produces.

As the quark evolves in time, its virtuality, Q^2, decreases leading to a stronger α_s coupling and more radiation, predominantly soft gluons, being produced. The perturbative approach to QCD eventually breaks down after a large time interval $(t \sim \hbar/\Lambda)$ when the value of α_s becomes too large. At this point the non-perturbative hadronisation phase begins where the coloured partons are combined to form colourless hadrons.

As the separation between colour charges increases, the force between them increases and an increasing energy is stored in a narrow region of colour field between the charges. Eventually it is energetically more favourable for a colour-anticolour pair of quarks to be created from the vacuum, each of which combine with the appropriate part of the original to form two colourless objects between which there is no colour force. This hadronisation process continues to create more hadrons providing the energy is sufficient to provide the invariant mass of the produced hadron.

4.3 Coherence in Parton Showers

The effect of quantum mechanics acting on the partons within the cascade is to suppress the emission of gluon bremsstrahlung at wide angles, known as coherence. Coherence restricts successive gluon emissions to decreasingly smaller angles, known as angular-ordering, as shown in figure 4.2.

In order to elucidate this coherence phenomenon, an analogy is drawn between photon bremsstrahlung from an e^+e^- pair. Figure 4.3 shows an e^+e^- pair with an opening angle of $\theta_{e^+e^-}$ created by pair-production. A photon with four-

Figure 4.2: *Angular-ordering of gluon emissions*

momentum k is subsequently emitted at time, t, by the electron and at angle $\theta_{\gamma e^-}$ with respect to the e^- direction.

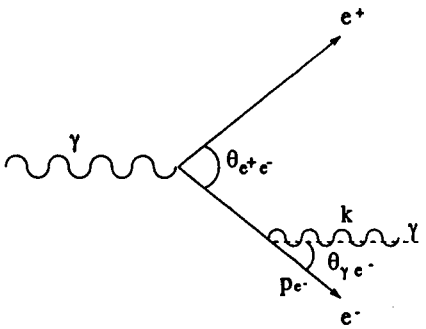

Figure 4.3: *Bremsstrahlung radiation of a photon after e^+e^- pair-production*

Using the uncertainty relation to estimate the "lifetime" of the intermediate electron which has virtual mass, $M = \sqrt{(p_e + k)^2}$, provides an estimate of the time interval required for the radiated γ to be formed.

$$t \sim \frac{1}{M}\frac{|\vec{p}_e|}{M} = \frac{|\vec{p}_e|}{(p_e+k)^2} \sim \frac{1}{|\vec{k}|}\frac{1}{\theta^2_{\gamma e^-}} \sim \frac{\lambda_\perp}{\theta_{\gamma e^-}} \tag{4.7}$$

where $\lambda_\perp$ is the transverse wavelength of the radiated photon, and the angle $\theta_{\gamma e^-}$ and mass of the final-state electron were assumed to be small.

During this time the e^+e^- pair separates a transverse distance

$$\rho_\perp^{e^+e^-} \sim \theta_{e^+e^-} t \sim \theta_{e^+e^-}\frac{\lambda_\perp}{\theta_{\gamma e^-}} \tag{4.8}$$

If the photon were emitted at large angles such that $\theta_{\gamma e^-} > \theta_{e^+e^-}$, the separation of the e^+e^- pair would be much smaller than the wavelength of the photon, $\rho_\perp^{e^+e^-} <$

$\lambda_\perp$. Wide-angle photons would therefore not resolve the individual charges of the e^+e^- pair but would probe the net electric charge which is zero. The emission of photons at large angles is therefore strongly suppressed, an effect which was first observed in cosmic ray studies [21].

A similar physical picture can be drawn for QCD cascades where a gluon is emitted from a quark. Although the net colour charge probed by a gluon emitted at large angles is non-zero, emissions of this kind are also strongly suppressed. As the phase space for successive gluons is reduced, gluons in the cascade are emitted with decreasing opening angles such that

$$\theta_1 > \theta_2 > \ldots > \theta_n.$$

The suppression of soft (low p_T) gluon emissions at wide angles leads to a modification of the inclusive momentum spectrum of partons within the cascade, the so-called "hump-backed plateau" [22]. This phenomenon can be understood as the result of two conflicting effects. Firstly, owing to the restriction $k_\perp > 1/R$ a soft particle is "forced" to be emitted at large angles, $\theta > 1/kR$ where R is the size of a hadron, typically a few hundred MeV. This restriction arises because the formation time of a parton, $t_{\text{form}} = k/k_\perp^2$ (from equation 4.7), must be less that the time interval elapsed before hadronisation takes place, $t_{\text{hadron}} \sim kR^2$. Coherence, however, limits the opening angle to small values after a few successive angular-ordered parton branchings. The net result is shown in figure 4.4: particles with intermediate values of momenta multiply most effectively in the QCD cascade. These effects result in a suppression of large multiplicity events and a modified peak position with respect to the incoherent case.

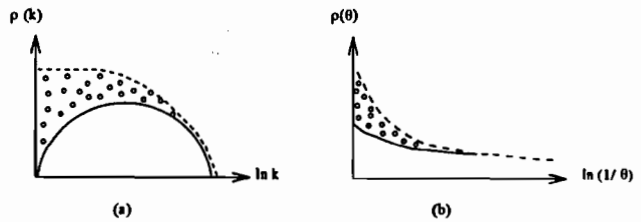

Figure 4.4: *The effect of colour coherence on the (a) energy and (b) angular distributions. The dotted area corresponds to the contribution which is removed from the incoherent (dashed) case to the coherent (solid) case.*

4.4 Predictions of the Modified Leading-Log Approximation

The Modified Leading Log Approximation (MLLA) of perturbative QCD has been developed to provide a quantitative description of the properties of soft particles with relatively small momenta ($z < 1$) which are radiated from high energy quarks and gluons [23]. The MLLA is required as the Double Logarithmic Approximation (DLA), which attempts to describe soft particle production, overestimates the multiplicity of particles produced within the parton cascade and the energy with which they multiply most actively. To control the parton production, the MLLA takes account of single logarithmic terms and coherence effects within the parton shower as discussed in the previous section.

The MLLA predicts the form of the inclusive momentum distribution for massless partons radiated from a high energy source, of energy $E \equiv Q/2$. At high energies and in the relativistic limit, the analytical form is given by the limiting-spectrum, $\bar{D}^{\lim}(\ln(1/x_p), Y)$, described in reference [23]. The variables are $\ln(1/x_p)$ where $x_p = p/E = 2p/Q$, known as the scaled momentum, and $Y = \ln(E/\Lambda_{\rm EFF}) = \ln(Q/2\Lambda_{\rm EFF})$. The free parameter $\Lambda_{\rm EFF}$ is an effective QCD scale and cannot be compared to exact QCD calculations *eg* $\Lambda_{\overline{\rm MS}}$ since there is no

present theoretical calculation which describes $\Lambda_{\rm EFF}$ beyond leading logarithmic terms in a specific renormalisation scheme.

The MLLA predictions are used in conjunction with the hypothesis of Local Parton-Hadron Duality (LPHD) [24], in which the observed hadron distributions are related to calculated parton distributions by a constant of proportionality, which is predicted to be independent of the energy of the hard scattering process.

This means that the hump-backed plateau is not only predicted to be experimentally observed but the MLLA results can be directly applied to the observed distributions such that

$$\frac{1}{\sigma}\frac{\mathrm{d}\sigma}{\mathrm{d}\ln(1/x_p)} = \kappa^{\rm ch}\bar{D}^{\lim} \tag{4.9}$$

where the parameter $\kappa^{\rm ch}$ is the constant of proportionality used to relate the hadron spectrum to the analytical spectrum from the MLLA.

Around the peak position the exact MLLA result can be approximated by a Gaussian distribution

$$\frac{1}{\sigma}\frac{\mathrm{d}\sigma^{e^+e^-}}{\mathrm{d}\ln(1/x_p)} = N(Y)\left(\frac{36N_c}{\pi^2 bY^3}\right)^{1/4}\exp\left[-\sqrt{\frac{36N_c}{b}}\frac{(\ln(1/x_p)-\ln(1/x_p)_{\rm max})^2}{Y^{3/2}}\right] \tag{4.10}$$

where $b = \frac{11}{3}N_c - \frac{2}{3}N_f$ is a constant which depends on the number of colours, N_c, and flavours N_f. $N(Y)$ is the average charged particle multiplicity which, within the assumptions of LPHD, is proportional to the soft parton multiplicity predicted by the theory.

Perturbative QCD not only predicts the shape of the limiting spectrum but also describes its energy evolution with Q. Analysis of the energy evolution of the hadron spectrum with Q should provide direct evidence on the energy evolution of the underlying parton spectrum. The peak position of the distribution is predicted to evolve as

$$\ln(1/x_p)_{\rm max} = 0.5Y + \sqrt{cY} - c + \mathcal{O}(Y^{-\frac{1}{2}}) \tag{4.11}$$

where $c = \frac{11}{48}\frac{(1+2N_f/11N_c^3)^2}{1-2N_f/11N_c} = 0.29(0.35)$ for $N_f = 3(5)$ and $\mathcal{O}(Y^{-\frac{1}{2}})$ contains

higher-order corrections. In equation 4.11, apart from the higher-order correction, Λ_{EFF} is the only free parameter: once a value for Λ_{EFF} is established the peak position at any Q can be predicted. This will be discussed in chapter 8.

4.5 Coherence in e^+e^- Annihilation

Several e^+e^- annihilation experiments have studied the inclusive scaled momentum distribution, $\ln(1/x_p)$, of charged particles in the reaction $e^+e^- \rightarrow$ hadrons [25][26][27] and its evolution with $Q \equiv \sqrt{s}$. An approximately Gaussian distribution has been observed at several values of $\sqrt{s}$ as shown in figure 4.5, although the hump-backed shape of the distribution alone does not indicate the presence of gluon coherence [28]. Coherence does, however, modify the peak position and the degree of fall-off on the right-hand side of the peak, corresponding to the low momentum end of the spectrum, in comparison to the incoherent case. Results from the OPAL collaboration [26] obtained by fitting the limiting spectrum to their data yield values of $\Lambda_{EFF} = 253 \pm 30$ MeV and $\kappa^{ch} = 1.28 \pm 0.01$.

The peak position, $\ln(1/x_p)_{max}$, can best be studied by considering its evolution with increasing values of $\sqrt{s}$. This has been achieved by combining results from several different experiments at different beam energies *eg* from TASSO and OPAL. The value of Λ_{EFF} obtained from OPAL from fitting equation 4.11, in which the $-c$ and higher-order term were combined into a single free parameter in the fit, is 203 ± 30 MeV. The results from the e^+e^- experiments are compared to the ZEUS measurements in chapter 8.

The results from the e^+e^- annihilation experiments are described by the MLLA, thereby supporting the concept of coherence, one of the basic predictions of perturbative QCD, and the assumption of LPHD.

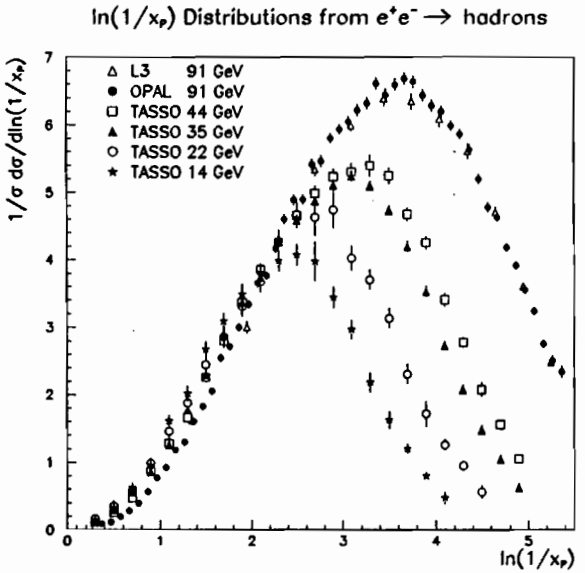

Figure 4.5: $\ln(1/x_p)$ *distribution of charged particles from the reaction* $e^+e^- \rightarrow$ *hadrons measured at various centre-of-momentum energies*

4.6 Coherence in Deep Inelastic Scattering

The kinematic region accessible by HERA allows tests of perturbative QCD to be made over a large kinematic range. Hence the energy evolution of the $\ln(1/x_p)_{max}$ can be determined over a large range in Q by a single experiment.

The observed particles in DIS emanate from the evolution of partons from the struck quark and the proton remnant. The evolution of the partons from these two regions is quite different and it is therefore advantageous to separate the two for independent study [29]. This is not readily achieved in the laboratory frame and requires the event to be transformed to the Breit frame of reference [30].

In this frame the exchanged current, q, is completely space-like, having zero energy component and components of momentum which are conventionally aligned in the negative z direction so that $q = (q_0, \vec{q}) = (0, 0, 0, -Q)$.

In the naïve QPM, the incoming quark, which has fraction x of the proton's momentum, collides elastically with the virtual boson and is scattered in the opposite direction $p'_{\text{quark}} = -xP'$ as shown in figure 4.6b. The proton remnant continues in the direction of the incident proton with momentum $p'_{\text{remnant}} = (1-x)Q/2x$. The Breit frame separates into two hemispheres into which particles are assigned by virtue of their longitudinal momentum component in this boosted frame. Particles with $p'_z < 0$ form the current region, corresponding to the direction of the struck quark in the QPM; whilst particles with $p'_z > 0$ form the target region.

4.6.1 Current Fragmentation Region

The current region is analogous to a single hemisphere in e^+e^- annihilation, as shown in figure 4.6. This leads to the conclusion that the evolution of soft QCD radiation from the struck quark in DIS should be identical to that from the q or $\bar{q}$ in e^+e^- [31]. While a "jet-axis" is required to define the hemisphere associated with the jet initiated by the q or $\bar{q}$ in e^+e^-, in DIS the virtual photon defines the analogue of this axis.

In this thesis, the sensitivity of soft QCD radiation to the energy of the hard scattering process is studied by considering the $\ln(1/x_p)$ distributions measured in the current region of the Breit frame. The DIS results are compared to the inclusive $\ln(1/x_p)$ distributions measured by TASSO and OPAL in chapter 8. As there is only one quark jet produced in the current region (CR), compared to two quark jets in the inclusive e^+e^- process, the overall normalisation of the distributions should differ by a factor 1/2 with respect to those in e^+e^- such that

$$\frac{1}{\sigma}\frac{d\sigma^{CR}}{d\ln(1/x_p)} = \frac{1}{2\sigma}\frac{d\sigma^{e^+e^-}}{d\ln(1/x_p)} \qquad (4.12)$$

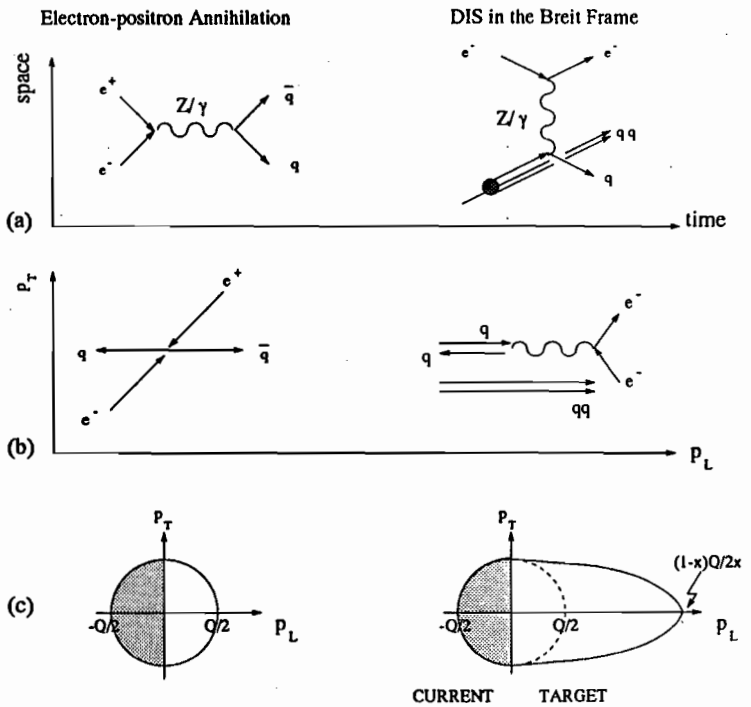

Figure 4.6: *Comparison of lowest order processes in e^+e^- annihilation into hadrons and DIS: (a) the space-time picture; (b) the space picture and the similarity of the current region in the Breit frame to a single hemisphere in e^+e^-; and (c) the phase space diagram for each process. Phase space for e^+e^- evolves with $Q/2 \equiv \sqrt{s}/2$. Similarly the current hemisphere in the Breit frame evolves with $Q/2$*

The evolution of the peak position of the $\ln(1/x_p)$ distribution, $\ln(1/x_p)_{max}$, is studied as a function of Q and x. An important property of successive soft emissions in the current region is the predicted x-independence. In practice, however, it is possible that some x-dependence may be observed due to hard parton emissions described in the following section.

4.7 Higher-Order Processes in the Breit Frame

The QPM picture of the Breit frame discussed so far is modified when $\mathcal{O}(\alpha_s)$ QCD corrections to the QPM are applied. Since the invariant mass of the $q\bar{q}$ or qg pair produced in these processes is no longer considered to be negligible, the incoming parton carries a fraction $p_p = \xi P$ of the proton's momentum, P, and $\xi > x$ to allow for the emission of the parton pair.

The cross section for these $\mathcal{O}(\alpha_s)$ processes depends on five variables: x, Q^2, the ratio x/ξ[1], z_p and ϕ^*. The variable ϕ^* is the azimuthal angle of the jet plane with respect to the virtual photon in the γ^*-parton centre of momentum system (CMS). The scaling variable x/ξ is given by

$$\frac{x}{\xi} = \frac{Q^2}{2p_p.q} = \frac{Q^2}{m^2+Q^2}, \quad (x \leq \frac{x}{\xi} \leq 1) \tag{4.13}$$

where m is the invariant mass of the qg or $q\bar{q}$ system.

The second scaling variable z_p is given by

$$z_p = \frac{P.p'_p}{P.q} = \frac{1}{2}(1-\cos\theta^*), \quad (0 \leq z_p \leq 1) \tag{4.14}$$

where p'_p is the momentum of the final state quark/gluon. z_p is related to the polar angle distribution of the jet plane θ^* in the γ^*-parton CMS, equivalent to the Breit frame when $m^2 = Q^2$.

[1]The variable x/ξ is often referred to as x_p [32]. This notation has deliberately been avoided so as not to be confused with the scaled momentum $x_p = 2p/Q$.

The singularities in the BGF and QCDC contributions to the $\mathcal{O}(\alpha_s)$ cross section are given by

$$f_{\rm BGF} \propto \frac{1}{z_p(1-z_p)} \quad \text{and} \quad f_{\rm QCDC} \propto \frac{1}{(1-x/\xi)(1-z_p)} \tag{4.15}$$

The poles at $x/\xi = 1$ and $z_p = 1$ in the QCDC case are identical to the pole-structure of the $\mathcal{O}(\alpha_s)$ e^+e^- cross section. Hard QCD radiation gives rise to three event topologies [32] which populate different regions in the $(x/\xi, z_p)$ plane as shown in figure 4.7.

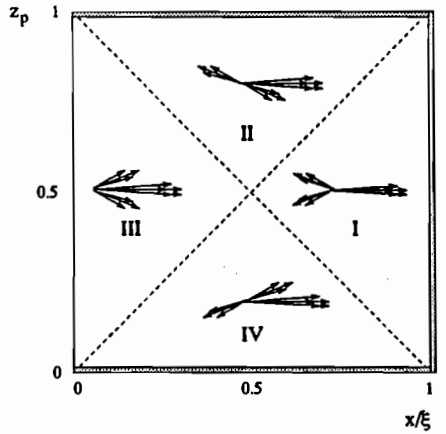

Figure 4.7: *Event topologies on the $(x/\xi, z_p)$ plane. Region I shows two jets in the current region and one in the target. In regions II and IV there is one jet in the current and two in the target, whilst in region III all three jets are in the target direction. The shaded regions indicate the singularities in the cross section at $x/\xi = 1$, $z_p = 0$ and $z_p = 1$.*

The singularities given in (4.15) indicate the relative rates with which each of the topologies occur in the Breit frame. For QCD Compton events, these occur at $x/\xi = 1$ and $z_p = 1$. The $x/\xi = 1$ pole enhances qg jets with a low mass, m^2, therefore favouring the event topology with two jets in the current region which

balance in p_T (region *I* in figure 4.7). The $z_p = 0$ pole in the QCD Compton events corresponds to the plane of the q and g jets making an angle of $\theta^* = 0$ or π to the photon axis, analogous to the collinear emission of the gluon to the q or $\bar{q}$ in e^+e^-.

The difference between $\mathcal{O}(\alpha_s)$ processes in DIS and e^+e^- is the additional BGF contribution. The poles from the BGF contribution are at $z_p = 0$ and 1. As the mass of the $q\bar{q}$ pair is no longer suppressed, BGF can contribute to the depopulation of particle multiplicity in the current region (region *III* in figure 4.7). The cross section for BGF increases at low x where this topology is expected to be more significant. The overall normalisation which measures the average multiplicity per event is therefore expected to be sensitive to these different topologies.

4.7.1 Rapidity Gap Events

As discussed in reference [33], events with a large rapidity gap are observed in DIS. Such events are consistent with the exchange of a colourless object, conventionally called the pomeron, whose constituents take part in the hard scattering process with the virtual photon. In contrast to the non-rapidity gap events in which there is QCD radiation between the struck quark and the proton remnant, QCD radiation is suppressed in this class of events [34]. This means that in the Breit frame there is less QCD radiation available to depopulate the current region. Selecting LRG events is, therefore, equivalent to suppressing events with large $m^2 > Q^2$. The effect of this subsample of events on the inclusive $\ln(1/x_p)$ distribution is discussed in chapter 8.

4.7.2 Target Fragmentation Region

The coloured parton in the initial state means that the contribution to the target region is more complicated compared to the current region. Three contributions

are considered in analytical calculations for parton emission in this region and are shown in figure 4.8. Full details of these are given in [35] [36] and only a brief description is included here.

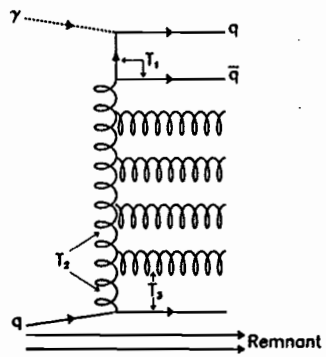

Figure 4.8: *Radiation in the initial state provides three contributions to the target region in the Breit frame*

The first of these, T_1, comes from parton emissions from the quark-antiquark pair; the second contribution, T_2 is due to soft coherent radiation from the vertical gluon lines. Partons produced due to these two contributions have momentum $p' \lesssim Q/2$ and therefore populate the circular region of phase space in the target region. The third contribution, T_3, corresponds to hard emissions from the horizontal rungs in the ladder which populate the $Q/2 \lesssim p' \lesssim (1-x)Q/2x$ region of phase space. An additional contribution to the target region will come from the fragmentation of the spectator target remnant. The detector acceptance for tracks produced in the target region is relatively poor as shown in chapter 6 and is therefore not considered in this thesis.

Chapter 5

Simulation of Deep Inelastic Scattering

5.1 Overview

Monte Carlo simulation is an indispensable tool with which a direct comparison between theory and experiment can be made. The basic lepton-quark scattering process is well understood, however in order to describe the hadronic final state in DIS it is necessary to include higher QCD corrections to this simple QPM as well as hadronisation. This results in a variety of theoretical models which aim to describe as closely as possible the observed distributions in DIS.

The event generators simulate the physical processes according to these models using the Monte Carlo prescription, and produce four-vectors of the complete final state which can be input into the detector simulation program. This models the response of the detector and its effect on the particles which pass through it, allowing a direct comparison of uncorrected data and Monte Carlo. In addition the acceptance and resolution effects of the detector on a measurement can be unfolded from the data to determine the true nature of the measured distribution. Corrected distributions can then be compared to the generator level in order to

interpret the underlying physical processes.

Event generation is simulated in three distinct stages.

- The cross-section for partons involved in the hard scattering process is calculated with an exact matrix element which may include first-order $\mathcal{O}(\alpha_s)$ QCD corrections. The distribution of partons within the proton are provided separately;
- The simulation of higher-order corrections is achieved using models based on the LLA, giving rise to a parton cascade. Modifications are included in the LLA to simulate coherence effects and are discussed in section 5.3.
- Hadronisation of the coloured partons into colourless hadrons and their subsequent decays.

Each of the generated event samples described below are passed through the ZEUS detector simulation program MOZART, based on the GEANT 3.13 [13] program which incorporates knowledge of the apparatus and trigger response based on previous running experience and test beam results.

5.2 Monte Carlo Models

ARIADNE

A sample of 200 K neutral current DIS events with $Q^2 > 4\text{GeV}^2$ was generated using LEPTO 6.1 [37] to generate the hard scattering process. The generation included the effects of initial and final state photon radiation which were calculated with the HERACLES 4.4 program [38] and interfaced to LEPTO via the DJANGO 6.0 [39] program. The proton structure function was parameterised by the MRSD'_ [40] set of parton distribution functions which provide a reasonable description the proton structure function, F_2, as measured at HERA [41].

The QCD cascade simulation was interfaced to LEPTO using the colour-dipole model (CDM) as implemented in ARIADNE 4.03 [42]. In this model the gluon emission is treated as radiation from the point-like struck quark and the extended proton remnant. Further emissions can occur between dipoles formed between the gluon and struck quark, and the gluon and proton remnant *etc.* Since the boson-gluon fusion process is not accounted for in the CDM, provision is made in ARIADNE to include this process as given by the first order matrix element within LEPTO.

The final state quarks and gluons are combined to form colourless hadrons via the Lund string model [43] as implemented in the JETSET [44] program. In the string model, the coloured quarks are connected by coloured 'strings' with 'kinks' in the string representing the gluons. The string is stretched as the struck quark moves away from the proton remnant until it is energetically more favourable for the string to break into colourless hadrons.

This Monte Carlo was found to give the best overall description of the observed energy flow [45] and has been used in the central analysis to correct and unfold the measured $\ln(1/x_p)$ distributions as discussed in chapter 8.

Comparisons of the measured $x_{\rm DA}, Q^2_{\rm DA}$ distributions from uncorrected data and the ARIADNE Monte Carlo at the detector level are shown in figures 5.1(a) and (b). Both the data and Monte Carlo satisfy the selection cuts described in chapter 6. The observed discrepancy at low x and Q^2 is attributed to the difference between F_2 from the MRSD'_ set and the measured value.

Figure 5.1(c) shows the electron energy spectrum, $E'_{\rm DA}$, calculated from $Q^2_{\rm DA}$ and the scattered electron angle, θ. The polar angle distribution of the scattered electron is shown in figure 5.1(d). Both distributions are reasonably well described by the ARIADNE Monte Carlo.

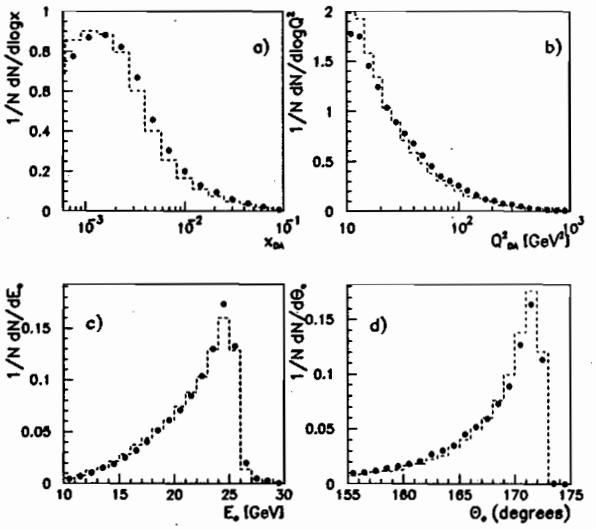

Figure 5.1: *Comparison of $x_{\rm DA}$, $Q^2_{\rm DA}$ and the energy and θ distribution of selected ZEUS DIS data with the ARIADNE Monte Carlo.*

ARIADNE and POMPYT

The ARIADNE 4.03 Monte Carlo does not describe the observed $(8-10\%)$ contribution from events with a large rapidity gap (LRG). Figure 5.2 shows the η_{max} distribution for data, and Monte Carlo, where η_{max} is defined as the maximum pseudorapidity $\eta = -\ln(\tan\frac{\theta}{2})$ of all calorimeter condensates[1] which have energy greater than 400 MeV. ARIADNE provides a reasonably good description of the majority of the data, however, the data show a clear excess of events with $\eta_{max} < 1.5$. These events are consistent with a diffractive mechanism

[1] A condensate is an isolated set of adjacent calorimeter cells.

in which a colourless pomeron is exchanged between the virtual photon and the proton. The excess of events with a large rapidity gap can be reasonably described [34] by the diffractive Monte Carlo, POMPYT [46], in which the beam proton emits a pomeron whose constituents take part in the hard scattering process. The diffractive events were generated with a hard quark momentum density within the pomeron [47].

Figure 5.2 shows that the mixture of 10% POMPYT and 90% ARIADNE provides a better description of the data at low η_{max}. The contribution of this class of events to the inclusive scaled momentum measurements presented in this thesis are discussed in chapter 8.

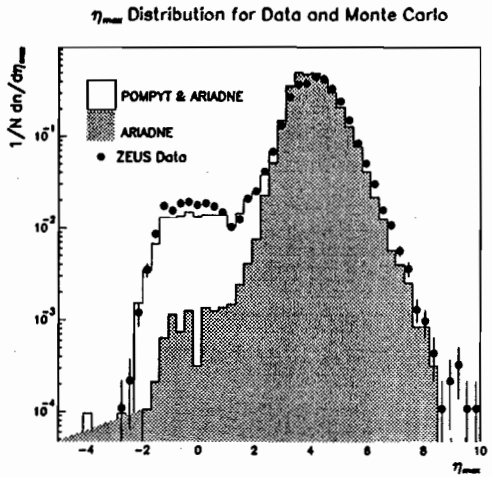

Figure 5.2: *η_{max} distribution of uncorrected data. Most of the data is well described by ARIADNE; however, the excess of events with a large rapidity gap can be better described by including a* 10% *contribution of diffractive events from POMPYT.*

MEPS

Additional samples of Monte Carlo events were generated in order to test the sensitivity of the final results to the model which was used to correct the data. A second sample of 200 K DIS events with $Q^2 > 4$ GeV^2 was generated using the hard scattering process calculated from LEPTO as before and with electroweak corrections. The GRV(LO) [48] parton distribution functions were used to describe the structure of the proton. The parton cascade was simulated within LEPTO using the option in which the available phase space for the parton showering process in the initial and final states is restricted by the first-order matrix element. This matching is hereafter known as MEPS. Following reference [45], the MEPS option provides a better description of the hadronic final state as opposed to the matrix element or parton showering processes alone. Again, the Lund string model was used to perform the hadronisation.

HERWIG

A third sample of 100 K DIS events with $Q^2 > 4$ GeV^2 was generated using the HERWIG 5.7 generator [49] without electroweak radiative corrections. The MRSD'_ set of parton distribution functions were again used.

In the HERWIG model the QCD cascade is modelled using parton showers alone. After the perturbative QCD process, hadronisation is achieved using a cluster model [50] rather than string fragmentation.

5.3 Monte Carlo Simulations of Coherence

Coherence has been explicitly included in these models as follows:

- In the parton shower approach to the cascading process adopted by LEPTO and HERWIG, the opening angle between successive parton branchings becomes smaller as the cascade evolves in time.

- In ARIADNE there is a distinct region of phase space in which an emission from the dipole can occur. After emitting a gluon, this phase space is reduced for the next emission and so on. This is exactly the effect that coherence has on the parton cascade, reducing the phase space for successive gluon emissions to an angular ordered region.

Chapter 6

Selection of Deep Inelastic Scattering Events

6.1 Overview of 1993 Data Taking

During the 1993 running period an integrated luminosity of $\simeq$ 554 nb^{-1} was recorded by ZEUS from over 6 million third level triggers. Only a relatively small proportion of this data, however, consists of neutral current DIS events of interest to this analysis. The main bulk of the data comprises background due to beam-gas, cosmic ray and photoproduction events.

It is the aim of the selection cuts to reduce the level of background in order to obtain a fiducial sample of neutral current DIS events. These cuts are formulated based on the differences between the kinematic properties of DIS events and the various types of background.

The selection procedure is carried out in several stages from the online trigger through to the final offline event selection, tightening the cuts from one stage to the next. After the preselection, defined in appendix A, a sample of 91.34 K neutral current DIS events remain. Final cuts are applied to remove any remaining background and to ensure that the event kinematics can be

reconstructed reliably.

In this chapter, a description of the various experimental techniques used to recognise and reject background events is given. The event selection cuts stated, based on these techniques, are the final values applied in this analysis. Results from an investigation using Monte Carlo generated events to define regions in the (x, Q^2) plane which offer a high acceptance are also presented.

6.1.1 Description of the Backgrounds

The principal sources of background events are due to synchrotron radiation from the electron beam, collisions between stray protons and beam-line components (beam-wall), and interactions between the proton bunch and residual gas molecules in the beam-pipe vacuum (beam-gas). The beam-induced interactions can occur anywhere in the HERA ring, although synchrotron radiation is predominantly produced on the curved sections of the HERA accelerator far from the experiments. A series of masks and collimators in the electron accelerator absorb the synchrotron emissions and reduce the rate of this type of background in the detector considerably.

Beam-gas events generated many metres upstream from the interaction region are characterised by a high number of tracks with an apparent upstream vertex, and large early-arriving energy deposits in the RCAL (see section 6.2.2).

The proton beam can be accompanied by a large number of halo muons (beam-halo), which are caused by decaying pions created in beam-wall or beam-gas collisions. These halo muons are readily recognisable in the detector by the energy deposits they produce along the length of the CAL and muon chambers and the absence of primary vertex tracks. Halo muons can, in turn, collide with the beam-line components causing a spray of secondary particles in the forward direction in the same way as beam-gas interactions. The rate of beam-gas interactions is highly dependent on the beam conditions and pressure in the

beam-pipe. Estimates of the background production rates for design conditions and a luminosity of 1.5×10^{31} cm^{-2}s^{-1} are compared to the rate of physics events in table 6.1.

Source	Event Rate (Hz)
Neutral Current DIS:	
$Q^2 > 3$ GeV^2	3
$Q^2 > 5000$ GeV^2	10^{-4}
Photoproduction $Q^2 \to 0$:	
All Events	10^3
Visible in Detector	200
Background:	
Beam-gas interactions m^{-1}	300
Beam Halo	10^4
Synchrotron radiation	$8 \times 10^{17}(\gamma/s)$
Cosmic Rays	~ 20

Table 6.1: *Main physics and background rates at HERA, assuming a design luminosity of* 1.5×10^{31}cm^{-2}s^{-1}.

At HERA the dominant physics process is photoproduction where, as $Q^2 \to 0$, the exchanged photon is quasi-real and is not detected in the main detector. Whilst photoproduction is an interesting physics topic itself, it constitutes a high-rate background to the DIS process and a series of selection cuts are required to reduce the contamination from such events. Since only $\sim 20\%$ of photoproduction events can be tagged in the luminosity monitor upstream, the absence of the scattered electron is used to distinguish photoproduction events from neutral current DIS using the techniques discussed in the following section.

6.2 Background Rejection

6.2.1 Detector Operation

The components essential to this analysis are the CTD, calorimeter, the magnet and the luminosity monitor. For each run the status of these components was examined. The following requirements were necessary:

- the CTD should be at full high voltage with no large dead regions;
- the magnet should be switched on;
- the calorimeter should be operational without a significant number of adjacent dead channels (holes); and
- the luminosity monitor should be functioning.

Runs in which these conditions were not satisfied were removed from the event sample in the preselection stage.

6.2.2 Calorimeter Timing

As discussed in chapter 1, the use of plastic scintillator tiles in the calorimeter results in a fast response-time to electromagnetic and hadronic showers. The resulting timing measurement from the calorimeter has a resolution better than 1 ns, which, in conjunction with the hermeticity of the CAL, permits DIS events to be distinguishable from cosmic ray and beam-induced background. By comparing the calorimeter timing with the HERA clock, random events which do not correspond to a HERA $e-p$ bunch-crossing can be rejected. The rate of electron-gas, proton-gas and cosmics can be reduced this way. The rate of cosmic events can also be reduced by comparing separate time measurements from the upper and lower halves of the BCAL in cosmic-rejection algorithms.

The timing measurement for each of the calorimeter sections, FCAL, BCAL and RCAL is evaluated by calculating the energy-weighted time averaged over all the PMTs associated with a particular calorimeter section. The timing measurement is calibrated with respect to the HERA clock such that collisions which occur at the nominal interaction point, $z = 0$, such as DIS events ideally, correspond to t=0 ns in FCAL and RCAL as illustrated in figure 6.1. In contrast, proton beam-gas events which occur many metres upstream deposit energy in the RCAL $\simeq$ 10 ns earlier than those events from the nominal interaction vertex. The length of the proton bunch was relatively small, typically $\simeq$ 20 cm, in comparison to the length of the detector during the 1993 running period. Genuine $e-p$ collisions therefore occurred within an interaction region rather than at a well-defined interaction point.

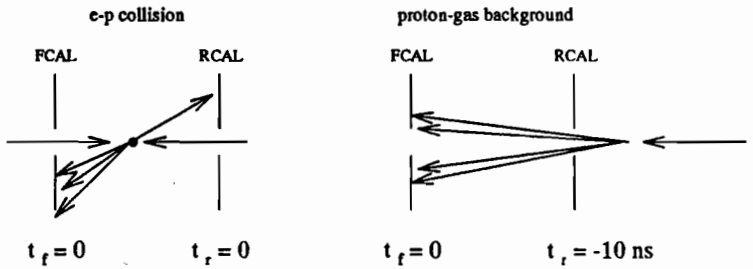

Figure 6.1: *Illustration of how calorimeter timing can be used to distinguish between $e-p$ collisions at the nominal interaction region and upstream beam-gas background.*

The calorimeter timing requirements were chosen as follows for the final event selection sample:

$$|t_R| < 3 \text{ ns, for } E_{RCAL} > 5 \text{ GeV or;}$$
$$|t_F - t_R| < 5 \text{ ns}$$

A looser timing cut for events with $E_{RCAL} < 5$ GeV ensures that high Q^2 events, in which the scattered electron is detected in BCAL or FCAL, are not removed from the sample.

6.2.3 Momentum Conservation

Another technique employed to discriminate against background events is the quantity

$$\delta = E - p_z + 2E_\gamma = \sum_i E_i(1 - \cos\theta_i) + 2E_\gamma \qquad (6.1)$$

where the sum is over all calorimeter cells, i, and E_γ is the energy measured in the photon calorimeter of the luminosity monitor. One of the advantages of such a formula is the insensitivity of δ to the proton remnant since it continues in the forward direction.

For neutral current DIS events in which the scattered electron is measured in the calorimeter, δ should be nearly twice the electron beam energy. The E_γ term in equation 6.1 means that this technique is applicable to events in which an initial state photon is radiated. In contrast, the scattered electron in photoproduction events remains undetected in the calorimeter due to the small momentum transfer involved, and so the value of δ is significantly lower than for DIS events. The final selection requires events to have

$$\delta > 35 \text{ GeV}.$$

6.2.4 Electron Identification

The signature of neutral current DIS events is the presence of the scattered electron in the final state. Correctly identifying the electron and measuring its position and energy are crucial elements of this analysis as discussed in chapter 7.

Conservation of momentum results in event topologies where the transverse momentum and azimuthal angle of the scattered electron balance the current jet. Generally the electron is well-isolated from the hadronic final state over

much of the (x, Q^2) plane (see figure 6.2) making electron identification relatively straightforward. At low x, however, the current jet is scattered in the rear

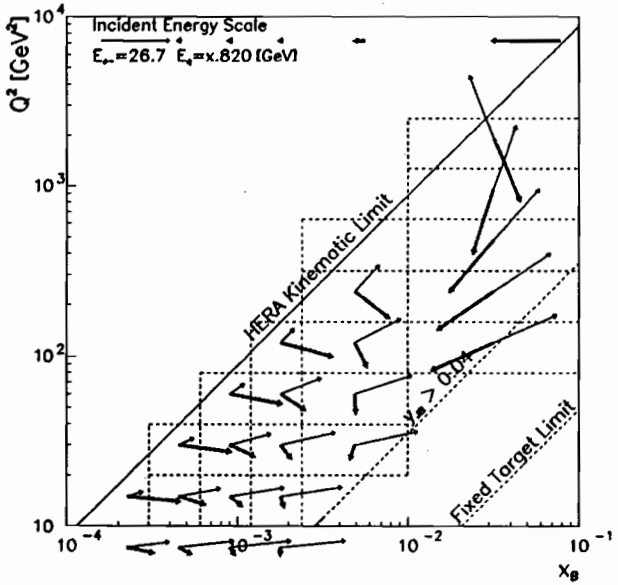

Figure 6.2: *Direction of the scattered electron (thin line) and struck quark (thick line) across the (x, Q^2) plane in lowest order DIS events. The length of the vectors is proportional to the electron and quark energy.*

direction and the electron has relatively lower energy. The increased hadronic activity in the vicinity of the scattered electron makes its identification more problematic.

Electron identification in the low x, high y region suffers an additional complication due to the low energy of the scattered electron. Electromagnetic showers from π^0 decays in the calorimeter may be mistaken for low energy electrons by the electron-finding algorithms. Normally, at higher x and lower y, the scattered electron deposits a greater amount of energy than the π^0 shower,

but in photoproduction events where there is no detectable scattered electron, mistaking a π^0 shower for a low energy DIS electron becomes more probable.

Several electron finding algorithms, the details of which are given elsewhere [51], have been formulated entirely from calorimeter information. The identification procedure is based on the differences between the shower profiles formed by electrons, hadrons and muons in the calorimeter. The quality of a particular algorithm is measured using Monte Carlo techniques in terms of purity and efficiency:

$$\text{Efficiency} = \frac{\text{Number of electrons correctly identified}}{\text{Number of generated electrons}} \quad (6.2)$$

$$\text{Purity} = \frac{\text{Number of electrons correctly identified}}{\text{Number of electrons identified}} \quad (6.3)$$

The ideal electron finding algorithm has both a high efficiency and purity over the full kinematic plane. Since the rate of photoproduction events is high in comparison to DIS, an algorithm which offers high purity (EEXOTIC) rather than high efficiency has been chosen for this analysis.

It is clear from the above discussion that the efficiency and purity of the electron-finder improves at increased electron energy. For the final event selection the identified scattered electron was required to have

$$E'_e > 10 \text{ GeV}.$$

At $E'_e = 10$ GeV the efficiency and purity of the electron finder are 67% and 97% respectively [52]. For $E'_e > 20$ GeV the efficiency and purity rise to $\geq 98\%$ and $\geq 99\%$.

Photoproduction events tend to produce low energy fake electrons primarily in the forward direction. Since the expected DIS rate for such events is low, these events are removed by requiring

$$y_{elec} < 0.95.$$

This cut has little or no effect for BCAL and RCAL electrons, since for $E'_e > 10$ GeV only electron candidates with $\theta < 42.8°$ are removed.

6.2.5 Event Vertex Position

The z-position of the event vertex provided from the tracking system is used to remove events which do not originate near the nominal interaction region. Typically, the types of background removed using this cut are upstream beam-gas events and cosmic rays.

In the final selection cuts all the kinematic variables and electron properties are measured with respect to this vertex position. It is therefore vital that the reconstructed track vertex provides a reliable measurement. Figure 6.3 shows the z_{vtx} distribution for the preselected DIS data sample and shows the contribution at $z = +60$ cm from the proton satellite bunch, a $\sim$3% spill-over of protons from the main bunch. The shaded area shows the z_{vtx} distribution with which the Monte Carlo events were generated to reproduce the data.

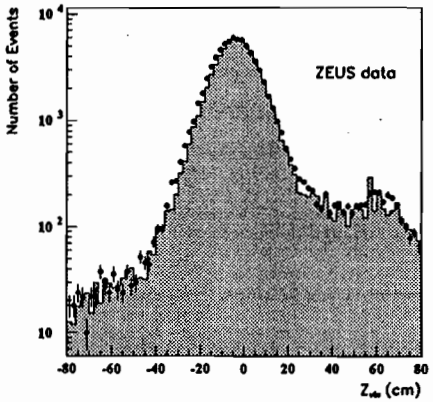

Figure 6.3: *The z_{vtx} distribution of the preselected DIS data (points) and the ARIADNE Monte Carlo (histogram). The peak at +60cm is the contribution from the proton satellite bunch and is included in the Monte Carlo simulation.*

A Gaussian fit to the main peak has an RMS of 10.4 cm [53]. For the final selection, data were required to have a tracking vertex reconstructed by

the VCTRAK package which satisfied

$$-50 < z_{vtx} < 40 \text{ cm} \quad \text{and} \quad r_{vtx} = \sqrt{x_{vtx}^2 + y_{vtx}^2} < 10 \text{ cm}.$$

The cut is asymmetric in z to account for the shift in vertex position from zero and to reduce the contribution from the proton satellite peak. The loose cut on r_{vtx} ensures that the primary vertex has been reconstructed within the beam-pipe region.

6.2.6 QED Compton Rejection

Elastic QED Compton events, $ep \rightarrow ep\gamma$, where the proton is elastically scattered, are not simulated in the Monte Carlo. These events were removed from the data sample using offline algorithms based on their event topology of two calorimeter energy deposits balanced in p_T, one of which typically has an associated track.

6.3 Improvement of Reconstruction Accuracy

The previously described cuts have selected a relatively clean sample of DIS events. In this analysis the double-angle method is used to reconstruct x and Q^2, the formulae for which are given in chapter 3. Additional kinematic cuts, however, are applied to ensure that these kinematics can be reconstructed reliably.

6.3.1 Box Cut

In events where the scattered electron impinges the RCAL near the beam-pipe hole, partial losses of the electron shower can occur which degrade the measurements of the electron energy and angle. To ensure that the electron shower is well-contained within the calorimeter so that its position can be well-reconstructed, the impact point of the scattered electron on the face of the RCAL was required to be outside a square region of dimension 32 cm$\times$32 cm centred on

the beam axis[1]. Events were required to satisfy the box cut:

$$|x| > 16 \text{ cm and } |y| > 16 \text{ cm}$$

otherwise they were rejected at the preselection level.

6.3.2 Hadronic Activity

The other input to the double-angle formulae is the hadronic angle, γ_h. Since this is calculated from calorimeter cells except those associated with the scattered electron, a minimum hadronic activity in the calorimeter is required for γ_h to be reconstructed reliably. A suitable quantity for this purpose is the measurement of y from the hadronic energy, y_{JB}.

Noise from the depleted uranium and the electronics, can be mistaken for hadronic energy which in turn affects the accuracy of the γ_h measurement. Below y_{JB} of 0.02 the measurement of γ_h is distorted by uranium noise. As discussed in chapter 3, at increased values of y_{JB}, the resolution of γ_h and hence x improves.

For improved kinematic reconstruction, events are required to satisfy

$$y_{JB} > 0.04$$

6.4 Analysis Bins

The choice of bins in x and Q^2 in which the analysis is performed was based on a subset of those used to measure the proton structure function, F_2, using 1992 data [41]. At low (x, Q^2) the choice of F_2 analysis bins was motivated by the resolution on the DA-reconstructed x and Q^2. However at high (x, Q^2) the bins were enlarged to increase the event statistics in each bin.

A Monte Carlo study was performed at the generator level using ARIADNE 4.03 to measure the acceptance due to:

[1]Recall that a hole 20 cm×20 cm is required to accommodate the beam-pipe.

- the event selection cuts which explicitly exclude regions of the (x, Q^2) plane, namely: the scattered electron energy, $E'_e > 10$ GeV and $0.04 < y < 0.95$ cuts; and
- the track cuts which must be applied to ensure that tracks are measured in a region where the CTD acceptance is high. The CTD offers good acceptance for tracks which satisfy $p_T > 200$ MeV and $|\eta| = -\ln(\tan\frac{\theta}{2}) < 1.5$ [54], equivalent to the polar angular region of $25° < \theta < 155°$.

The event acceptance was defined in each (x, Q^2) bin by

$$\% \text{ Acceptance} = \frac{\text{No. of events which satisfy cuts}}{\text{No. of events generated}} \tag{6.4}$$

The track acceptance in the current and target regions of the Breit frame was defined separately in a similar way to equation 6.4.

Since the data are corrected back to the full phase space defined by the (x, Q^2) region using a correction factor technique as discussed in chapter 8, it is important that the acceptance is high to ensure the validity of the correction method. A lower limit of 75% due to the event and track acceptances was required for events in a particular interval to be further analysed.

Figure 6.4 shows the percentage event acceptance over the (x, Q^2) plane. The isolines of constant electron energy $E'_e = 10$ GeV, $y = 0.04$ and $y = 0.95$ are indicated on the plot. These illustrate how much of the (x, Q^2) phase space covered by each bin is removed. The x range covered by the high x bin was modified compared to the range described by the F_2 analysis: the upper limit was lowered from 1.0×10^{-1} to 5.0×10^{-2} to increase the track acceptance in the current region. The figures in brackets refer to the original F_2 bin acceptances.

Figures 6.5 and 6.6 show the percentage track acceptances in the current and target regions respectively. The Monte Carlo events used to measure these acceptances were generated within the scattered electron energy and y cuts. Also shown are isolines of $\eta(\gamma_h) = \pm 1.5$, the pseudorapidity of the struck quark

direction in the QPM. Although no $\eta(\gamma_h)$ cut is applied, these contours are included to illustrate the effect of the η cut on tracks emanating from the struck quark. The acceptance of the current region is high over much of the (x, Q^2) plane, although figure 6.5 shows that the $\eta = -1.5$ cut, *ie* in the rear direction, is more significant than the $\eta = +1.5$ cut due to the topology of events in the kinematic region under study.

The acceptance of the target region is clearly much poorer than the current region. Many of the particles in the target region are produced at small angles to the proton beam. A significant number, $\sim 45\%$ of particles produced in this region are lost in the beam-pipe whilst a further $\sim 30\%$ are removed by the η requirement.

x range	Q^2 (GeV^2) range	No. of events
$6.0 - 12.0 \times 10^{-4}$	10-20	4990
$1.2 - 2.4 \times 10^{-3}$	10-20	4250
	20-40	2420
	40-80	1134
$2.4 - 10.0 \times 10^{-3}$	20-40	3113
	40-80	2470
	80-160	1174
	160-320	294
$1.0 - 5.0 \times 10^{-2}$	160-320	546
	320-640	216
	640-1280	73

Table 6.2: *Number of selected events in the analysis (x, Q^2) intervals.*

The final choice of bins and the number of selected events in each bin is

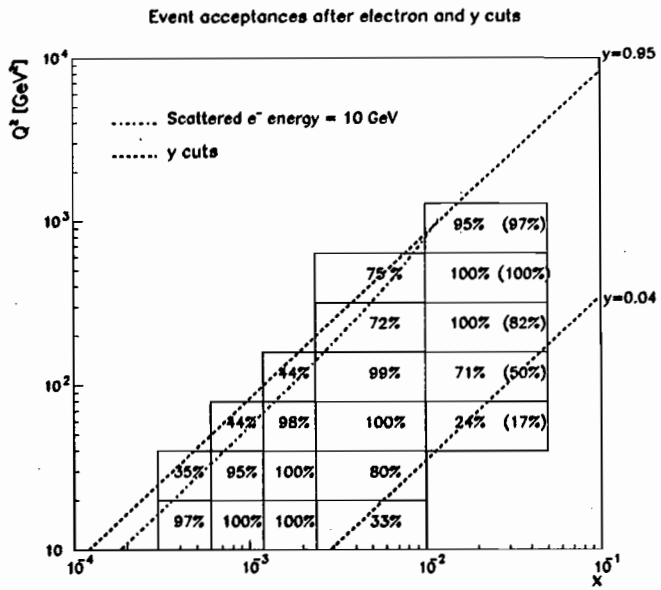

Figure 6.4: *Percentage event acceptances due the scattered electron energy, $E'_e >$ 10 GeV and $0.04 < y < 0.95$ cuts measured over the (x, Q^2) plane.*

presented in table 6.2. In chapter 8 the corrections factors in the $1.0 \times 10^{-2} < x < 5.0 \times 10^{-2}, 160 < Q^2 < 320$ GeV^2 bin transpire to be too large and this region is later excluded from the analysis.

6.5 Summary

A major challenge at HERA is to select the small number of DIS events which can be reconstructed reliably from the large number of background events. The selection cuts, the order in which they were applied and the number of events each cut rejects are summarised in table 6.3. The number of events remaining after the selection cuts is 31.29 K, of which 20.70 K occupy the analysis bins

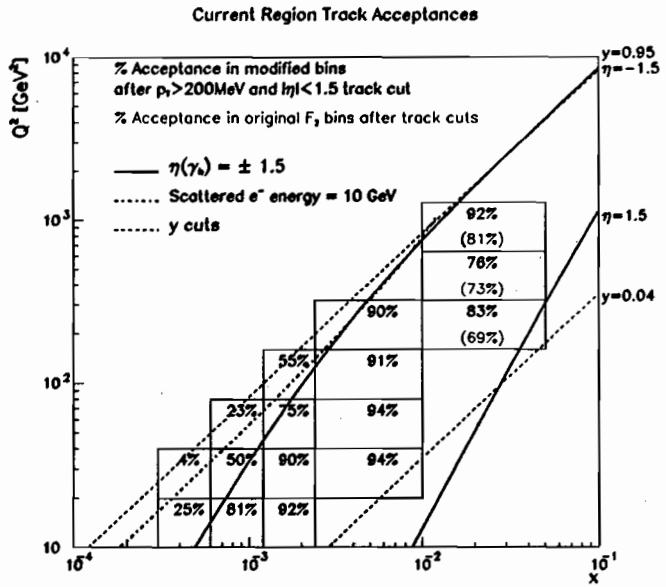

Figure 6.5: *Percentage track acceptances in the current region of the Breit frame due to the $p_T > 200$ MeV and $|\eta| < 1.5$ track selection cuts.*

selected for their high acceptance in the current region listed in table 6.2. The distribution of the selected events in the (x, Q^2) plane is presented in figure 6.7.

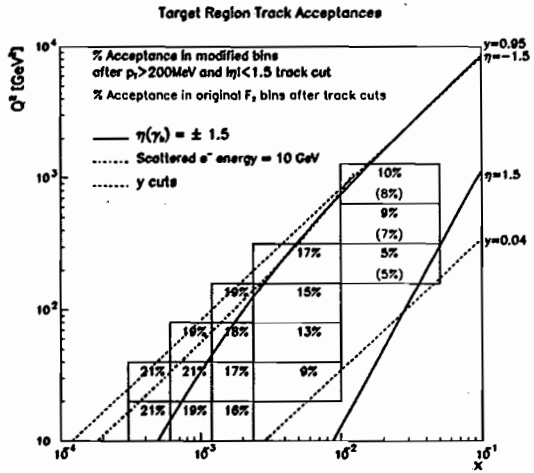

Figure 6.6: *Percentage track acceptances in the target region of the Breit frame due to the $p_T > 200$ MeV and $|\eta| < 1.5$ track selection cuts.*

Requirement	Number of events rejected
$e-p$ bunch crossing number	439
Electron found by EEXOTIC	22506
Electron energy > 10 GeV	5588
$\delta > 35$ GeV	583
$y_{elec} < 0.95$	19
$y_{JB} > 0.04$	17907
$Q^2_{DA} > 10$ GeV^2	11460
Tracking vertex with $-50 < z < 40$ cm	1409
Calorimeter timing	63
Not a cosmic μ	7
Not a QED Compton	77

Table 6.3: *Event selection cuts applied to the event sample and the number of events rejected by each cut.*

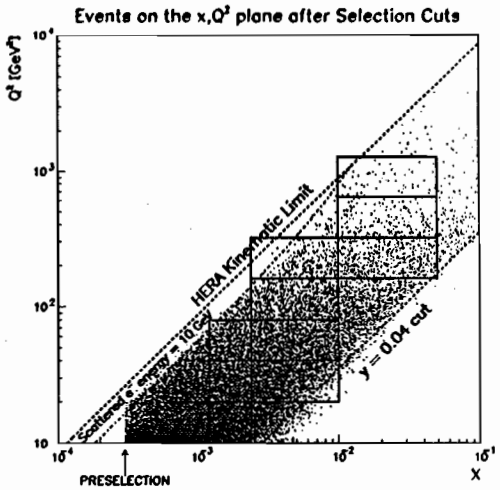

Figure 6.7: *The distribution of events on the (x, Q^2) plane which satisfy the selection criteria and have $x > 3 \times 10^{-4}$. The analysis bins are also indicated.*

Chapter 7

Reconstruction of the Breit Frame

In this chapter the transformation from the HERA laboratory system to the Breit frame and general properties of the boosted frame are described. Results from an investigation to identify the factors which limit the $\ln(1/x_p)$ measurement are presented. The investigation was restricted to the selected (x, Q^2) analysis regions and used the event selection cuts described in chapter 6 to optimise the resolution of the x and Q^2 measurements.

In principle, the reconstruction of charged tracks within the CTD as well as the reconstruction of the boost impose limits on the $\ln(1/x_p)$ resolution. This study shows that the resolution of the boost reconstruction dominates the resolution on this measurement.

7.1 The Transformation to the Breit Frame

The transformation from the HERA laboratory frame to the Breit frame is achieved by a Lorentz boost followed by rotations to align the virtual photon

with the negative z'[1] direction and the electron scattering plane in the $x' - z'$ plane as shown in figure 7.1. The lepton plane is rotated such that the outgoing electron has azimuthal angle, $\phi' = \pi$ with respect to the Breit frame x'-axis. Viewed from the laboratory frame, the Breit frame travels with velocity $\vec{\beta}$. If a

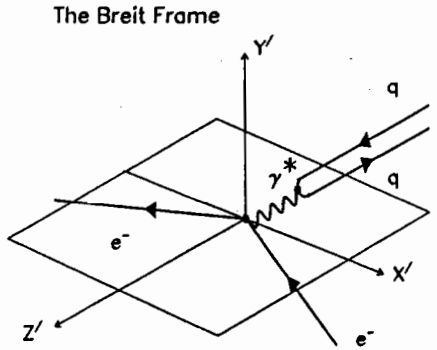

Figure 7.1: *The QPM picture of the Breit frame.*

particle with mass, M, is at rest in the Breit frame it has energy E and momentum $\vec{P}$ viewed from the laboratory system. $\vec{\beta}$ can then be expressed as $\vec{\beta} = \vec{P}/E$ and $\gamma = 1/\sqrt{1 - |\vec{\beta}|^2} = E/M$.

Particles with energy E and three-momentum $\vec{\mathrm{P}}$ in the lab frame can be boosted into the Breit frame and have resultant energy E′ and momentum $\vec{\mathrm{P}}'$ given by

$$\mathrm{E}' = \gamma(\mathrm{E} - \vec{\beta}.\vec{\mathrm{P}}) \quad \text{and} \quad \vec{\mathrm{P}}' = \gamma(\vec{\mathrm{P}} - \vec{\beta}\mathrm{E}) \tag{7.1}$$

[1] Breit frame quantities are indicated by the prime (′).

where $\vec{\beta}$ is given by

$$\vec{\beta} = \frac{\vec{q} + 2x\vec{p}}{q_0 + 2xp_0} \tag{7.2}$$

and $q = (q_0, \vec{q})$ and $p = (p_0, \vec{p})$ are the four-momenta of the virtual photon and the incident proton beam (ignoring the mass of the proton) measured in the laboratory.

The event is then rotated by the following angles:

1. $\Theta' = \pi - \theta'$ to align the virtual photon with the negative z' axis; and

2. $\Phi' = -\phi'$ to orientate the electron plane in the $\phi' = 0$ direction

where θ' and ϕ' are the usual spherical polar coordinates of the virtual photon measured with respect to the Breit frame axes. The rotation angles are defined by the momentum components of the virtual photon in the Breit frame.

Once the boost vector $\vec{\beta}$ has been established for each event, the four-vectors of reconstructed CTD tracks, determined from the momentum, polar and azimuthal angle measurements fitted at the primary vertex are boosted. As no particle identification was performed, *eg* using dE/dx information from the CTD, the energy of the tracks was calculated assuming the mass of the $\pi^{\pm}$.

7.1.1 Virtual Photon Reconstruction

Both the boost and the rotation are derived from the four-momentum components of the virtual photon. These are determined experimentally from the momentum components of the scattered electron.

The scattered electron is identified using a cone-based algorithm which is tuned to provide a sample of electrons with a high purity over a large range of x and Q^2. The polar and azimuthal angles are calculated at the centre of the shower development within the calorimeter, with respect to the reconstructed event vertex.

The optimum measurement of the scattered electron energy (in the lab frame) E'_e across the whole (x, Q^2) plane is provided by equation 7.3 which uses Q^2 measured by the double-angle formula discussed in chapter 3.

$$E'_e = \frac{Q^2_{\mathrm{DA}}}{2E_e(1 + \cos\theta_e)} \tag{7.3}$$

where E_e is the energy of the electron beam and θ_e is the angle of the scattered electron measured with respect to the proton direction. The use of the DA variables results in reduced sensitivity to the absolute calorimeter energy scale.

7.2 Properties of the Boost

In figure 7.2 the magnitude and direction of the boost, applied to transform particles from the laboratory to the Breit frame is plotted as a function of x and Q^2 [55][56]. The magnitude of the vectors is proportional to $\log\gamma$. The region of the (x, Q^2) plane over which the analysis is performed is also highlighted.

The figure shows that at high x, large negative longitudinal boosts are required to overcome the momentum imbalance between the high momentum parton and much lower momentum electron. This is required to make the incoming and outgoing partons collinear and the energy of the incident and scattered electrons equal. Conversely at low x the momentum of the parton is small in comparison to the incident electron and a substantial positive longitudinal boost is required. However, in the analysis region, indicated by the boxed area on the graph, the boost is relatively small and predominantly in the transverse direction.

In the quark parton model when $x = E_e/E_p$ the scattered electron has energy equal to the electron beam and the current therefore has a zero energy component, $q_0 = 0$. Since $\vec{\beta}.\vec{q} = q_0 = 0$ the boost vector is perpendicular to the virtual photon direction. Furthermore, at $y = 1$ a unique point in phase space is defined when the electron is back-scattered in the laboratory frame and the HERA and Breit system coincide. Events at this point cannot be experimentally detected, however,

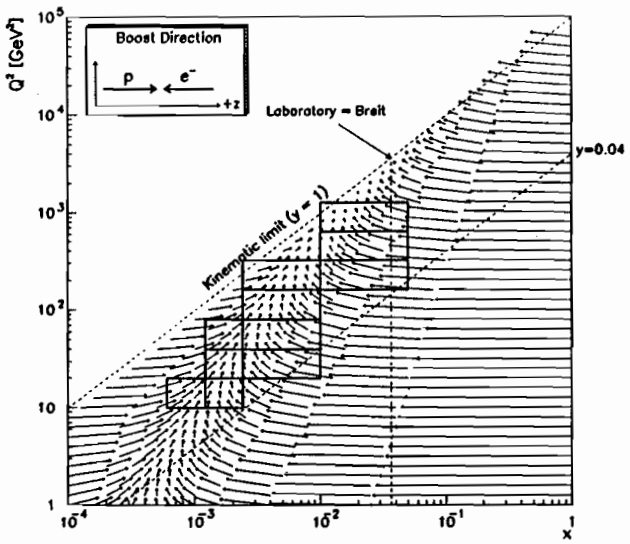

Figure 7.2: *A vector of magnitude* $\log\gamma$ *in the direction of the boost from the HERA laboratory frame to the Breit frame is shown.*

since the scattered electron and naïve parton are contained within the beam-pipe region.

Figure 7.3 shows an isotropic emission of massless 10 GeV particles with an angular separation of 6° in the laboratory frame. The shading distinguishes particles which are emitted with polar angles corresponding to the three calorimeter regions: FCAL (light grey), BCAL (black) and RCAL (dark grey). The angular coverage of the BCAL corresponds to the region of the CTD which has good acceptance for charged particle detection. The effect of boosting the particles into the Breit frame using $\vec{\beta}$ calculated at $Q^2 = 143$ GeV^2 and $x = 5.4 \times 10^{-3}$ is

shown in the lower plot.

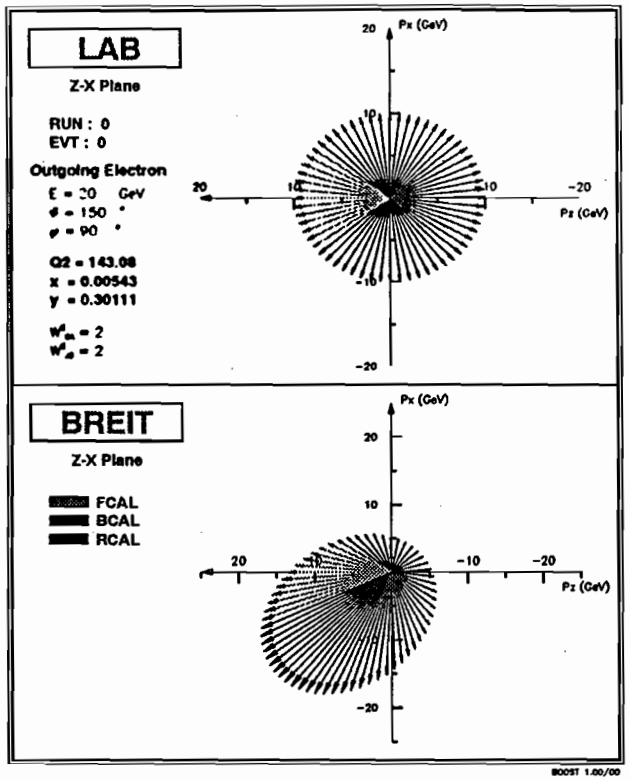

Figure 7.3: *Isotropic emission of a 10 GeV massless particle and the resultant transformation to the Breit frame.*

In the Breit frame the topology of the boosted isotropic emission varies for different x and Q^2 values from which the boost vector is calculated. However, particles emitted along the positive z axis in the laboratory frame remain in this direction in the Breit frame regardless of the magnitude and direction of the

boost [55].

A typical DIS event measured in the laboratory frame is shown in figure 7.4. A 15 GeV electron has been identified in the RCAL and the track corresponding to the electron has been reconstructed. Using the double-angle method the reconstructed x and Q^2 are 9×10^{-4} and 36 GeV^2 respectively.

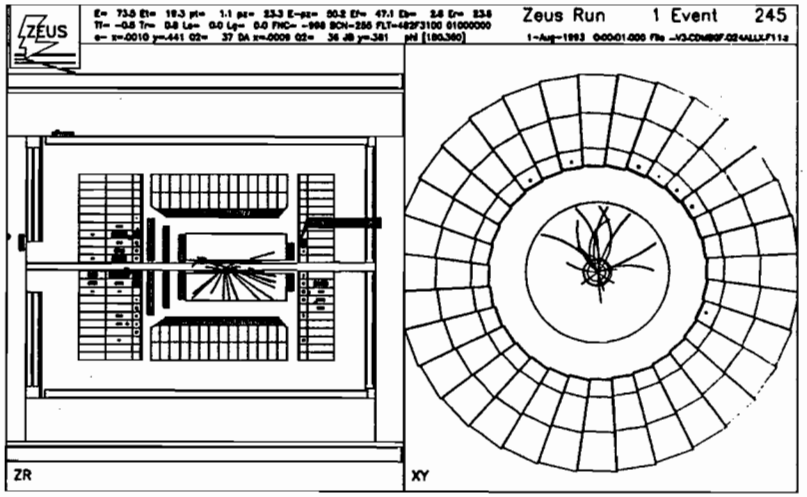

Figure 7.4: *The ZEUS event display illustrating a neutral current DIS Monte Carlo generated event.*

Selected track momentum vectors of the event are displayed again in figure 7.5. The upper plot shows the laboratory frame with the scattered electron in the negative z direction. The reconstructed incoming virtual photon is also indicated. The magnitude and direction of the reconstructed track momenta are displayed. Tracks with momentum components larger than the scale of the axes are illustrated by thicker lines and do not have an arrow indicating their direction.

The lower plot shows the event in the Breit frame. The incoming virtual

photon is shown in the target region, as are the incoming and outgoing electrons recognisable by their very large p'_z components. The majority of tracks have positive p'_z *ie* are in the target region, whilst a small number of tracks have been boosted into the current region. This is due to the increased phase space in the target region in comparison to the current (see figure 4.6 on page 64).

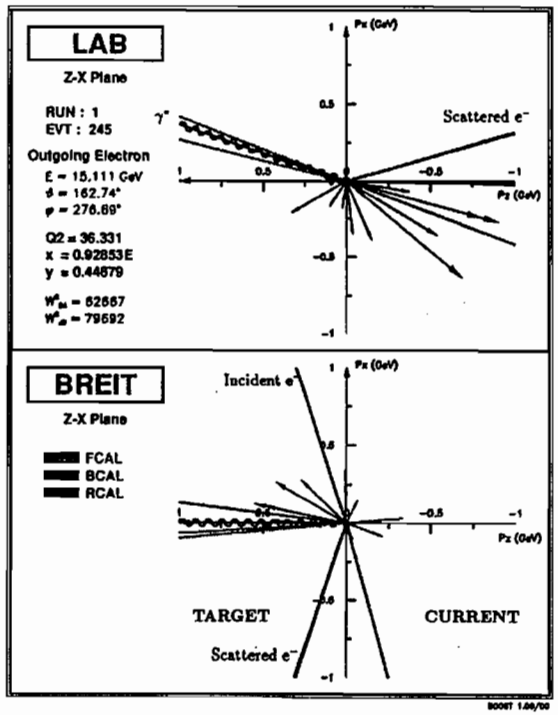

Figure 7.5: *The same event viewed in the laboratory and Breit frames.*

7.3 Reconstruction of the Boost

As seen in equation 7.2, the boost to the Breit frame is dependent on the correct reconstruction of $\vec{q}$ and x for each event. The distinction between the current and target regions necessarily relies on the Breit frame z-axis defined by

$$2xp'_0 - |\vec{q}| = 0 \tag{7.4}$$

where p'_0 is the energy of the incident proton in the boosted frame. Although the Breit frame is reconstructed such that equation 7.4 is satisfied, if the reconstructed values of xp'_0 and $|\vec{q}|$ deviate significantly from their true values the reconstructed and true axes will not coincide. If the reconstructed axes are translated and/or rotated with respect to the true axes, particles which were generated with $p'_z < 0$ can have $p'_z > 0$ in the reconstructed frame. The particle has migrated from the current region of the Breit frame to the target region. In addition to migrations between the current and target regions, misreconstruction of the axes leads to finite resolution of the momentum components in the boosted frame.

Figure 7.6 shows exaggerated examples of misreconstructing the axes in order to illustrate these points. The true Breit frame is shown in the first figure with a track vector measured in the current region. If the reconstructed axes are shifted with respect to the true axes the track vector has positive longitudinal momentum with respect to the reconstructed axes. Not only has it been reconstructed in the target region, but the magnitude of the momentum vector is smaller. Finally, if the measured axes are rotated with respect to the true ones, tracks can migrate from one region to another; however the magnitude of the track vector in the new frame is unchanged.

The level of migrations between the two regions was evaluated using the ARIADNE Monte Carlo events discussed in chapter 5 which have been passed through the detector simulation and satisfied the event selection cuts thereby ensuring the scattered electron had been reasonably well-reconstructed and $\vec{\beta}$

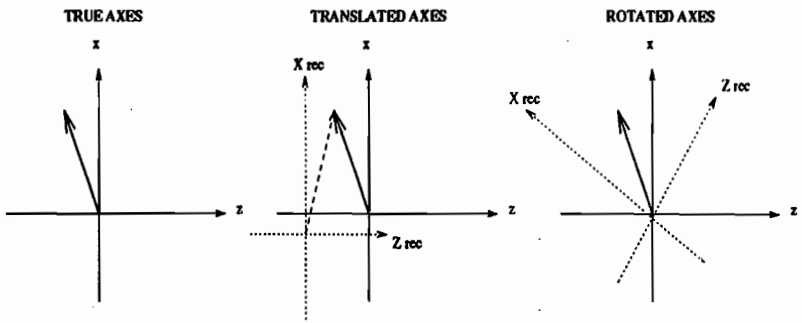

Figure 7.6: *A track vector generated in the current region can migrate to the target region by misreconstructing the axes such that they are translated or rotated with respect to the true frame.*

could be determined. The generated energy and momentum components of stable charged particles were boosted into the Breit frame using

- the generated virtual photon; and
- the virtual photon reconstructed from the scattered electron quantities.

Particles were assigned to the current or target region depending on the sign of their reconstructed longitudinal momentum component in the Breit frame.

Table 7.1 presents the number of particles generated in the current and target regions and the number of particles which migrate from one region to the other due to the boost reconstruction alone. The values are shown for a small sample of events and presented in each of the (x, Q^2) analysis bins.

The results presented in table 7.1 show that

- migrations from the current into the target region are more significant than those from the target into the current;
- migrations from the target region remain at a constant level $\simeq 3\%$ over the x, Q^2 plane; and

x	Q^2 (GeV^2) range	No. of particles in current		No. of particles in target	
		generated	migrate to target	generated	migrate to current
$6.0 - 12.0 \times 10^{-4}$	10-20	1434	302	6405	185
$1.2 - 2.4 \times 10^{-3}$	10-20	1525	389	4057	109
	20-40	1333	214	3477	116
	40-80	813	65	2013	68
$2.4 - 10.0 \times 10^{-3}$	20-40	2016	507	2615	50
	40-80	1793	235	1842	235
	80-160	1159	81	1396	27
	160-320	426	16	634	15
$1.0 - 5.0 \times 10^{-2}$	320-640	310	5	210	4
	640-1280	195	8	97	3

Table 7.1: *Comparison of the number particles generated in current and target region of the Breit frame and the number of particles which migrate from one region to the other due to the boost reconstruction.*

- migrations from the current region are greatest in bins at low y. In the three low y bins migrations from the current region can be as large as $\simeq 25\%$, however over most of the (x, Q^2) plane the migrations are much smaller, typically $\simeq 8\%$.

These findings are in accordance with the observation that the reconstructed value of x is typically greater than the generated value at low x.

To ascertain if particles migrate from a specific part of the $\ln(1/x_p)$ distribution, the generated $\ln(1/x_p)$ distribution current and target regions are plotted as shown in the upper half of figure 7.7. The shaded area highlights the particles which migrate out of the generated region after the track and boost reconstruction. The generated particles which migrate from the current region to the target region have a $\ln(1/x_p)$ distribution similar to the generated form with approximately the same mean. In the target region, however, particles tend to migrate from the high $\ln(1/x_p)$ end of the spectrum. For a fixed x and Q^2 this corresponds to the low momentum region.

Similarly the lower half of figure 7.7 plots the $\ln(1/x_p)$ distribution of reconstructed tracks which satisfy the track cuts and are assigned to the current and target regions. The shaded area corresponds to the contribution from tracks which were generated in the other region and have migrated. The $\ln(1/x_p)$ distribution from the target contribution to the current does not have as large a high $\ln(1/x_p)$ tail compared to the distribution of generated particles which migrate to the target. The $\ln(1/x_p)$ distribution of the contribution to the reconstructed target region from the generated current tends to populate the high $\ln(1/x_p)$ end of the spectrum. The shaded distribution in this plot, however, is broader with a mean position at a lower value of $\ln(1/x_p)$ compared to the generated region which migrates to the current.

A second way to study the quality of the boost is to consider the pull on $\ln(1/x_p)$ due solely to the boost reconstruction defined as

$$\sigma_{\mathrm{BOOST}}(\ln(1/x_p)) = \ln(1/x_p)_{\mathrm{REC}} - \ln(1/x_p)_{\mathrm{TRUE}} \tag{7.5}$$

where $\ln(1/x_p)_{\mathrm{TRUE}}$ is measured using true particles transformed to the current region of the Breit frame using the generated four-momentum components of the virtual photon. Similarly $\ln(1/x_p)_{\mathrm{REC}}$ is measured using true particles boosted using the reconstructed $\vec{q}$ for those particles which remain in the current region.

The profile of σ_{BOOST} is plotted as a function of the reconstructed $\ln(1/x_p)$ in figure 7.8 in each of the analysis bins. Points are plotted at the statistical mean of σ_{BOOST} in each $\ln(1/x_p)$ bin and the error bars represent the RMS spread on σ_{BOOST}.

Across the majority of the x, Q^2 plane the pulls due to the boost are flat as a function of $\ln(1/x_p)$ as shown in figure 7.8. In the bins at low y, however, low momentum particles are pulled to higher values of $\ln(1/x_p)$ in addition to the migrations into the target region which occur in these bins.

The Q^2 resolution shown in chapter 3 is sufficiently good, $10-15\%$, to assume

that $Q_{\rm REC}/Q_{\rm TRUE} \sim 1$ so that equation 7.5 can be approximated to

$$\sigma_{\rm BOOST} = \ln\left(\frac{p_{\rm TRUE}}{p_{\rm REC}}\right). \tag{7.6}$$

Since the shape of the $\sigma_{\rm BOOST}$ distributions indicate that low momentum tracks are affected most by the reconstruction of the boost and a rotation of the reconstructed axes with respect to the true axes alone does not affect the magnitude of the momentum vectors, the reconstructed axes must be shifted by an absolute amount $\vec{p}_{\rm DIFF}$ such that

$$\vec{p}_{\rm TRUE} = \vec{p}_{\rm REC} + \vec{p}_{\rm DIFF} \tag{7.7}$$

Clearly low momentum particles with $|\vec{p}_{\rm TRUE}| \simeq |\vec{p}_{\rm DIFF}|$ will be affected more by the translation of the axes than high momentum particles.

To investigate which particular aspect of the electron measurement the Breit frame transformation is most sensitive to, the Monte Carlo was used to study the pulls on $\ln(1/x_p)$ determined using electrons with the following properties:

- reconstructed energy, true θ_e and true ϕ_e;
- true energy, reconstructed θ_e and true ϕ_e; and
- true energy, true θ_e and reconstructed ϕ_e.

The pulls due to the individual reconstruction of the energy, θ and ϕ components of the electron are shown in figure 7.9. The resolution of $\ln(1/x_p)$ displays little sensitivity to the polar and azimuthal resolution of the calorimeter. It is the resolution with which the energy is measured that provides the most significant limiting factor.

The deterioration of the boost resolution at low y can be attributed to the problematic reconstruction of x and Q^2 at low y discussed in chapter 3. The double-angle method adopted here and discussed in chapter 3 is recognised as the technique which, in comparison to the electron or Jacquet-Blondel method,

provides the best x resolution over a large region of the (x, Q^2) kinematic plane and extends into the low y region. In the low y region, however, the γ_h angle given in equation 3.13 is in the very forward direction and therefore the p_T summed over all hadrons is relatively small. Hence the determination of γ_h is subject to a relatively large uncertainty. In addition, noise from the calorimeter affects the determination of y_{JB} at low y. These factors contribute to a less accurate determination in γ_h which is reflected in the x resolution in particular.

7.4 Resolution of $\ln(1/x_p)$

The resolution due to the overall measurement of $\ln(1/x_p)$ consists of a contribution from track reconstruction as well as the boost reconstruction discussed in the previous section. The pull on $\ln(1/x_p)$ due to the reconstruction of charged tracks is measured using the true boost throughout and calculating the difference between the $\ln(1/x_p)$ value of a measured track in the CTD and $\ln(1/x_p)$ from the corresponding generated particle. Figure 7.10 shows the profile plot of the pulls as a function of $\ln(1/x_p)$ in the measured regions of x and Q^2. The distributions are flat and show that the pulls on $\ln(1/x_p)$ due to the tracking measurement are small, particularly in comparison to the pulls due the boost reconstruction.

The overall pulls on the distributions measured in the reconstructed x and Q^2 bins are shown in figure 7.11.

A bin-by-bin correction technique is employed to correct the measured $\ln(1/x_p)$ distributions and is discussed fully in chapter 8. One of the requirements necessary to ensure that this technique is valid is to choose the width of the $\ln(1/x_p)$ bins commensurate with the resolution of $\ln(1/x_p)$ in the current region.

A binwidth of 0.25 $\ln(1/x_p)$ units was adopted and is shown on each of the plots. This is a conservative choice of binwidth except at high values of $\ln(1/x_p)$ where migrations between the $\ln(1/x_p)$ bins are largest. Since it is the position of the peak which of primary interest in this analysis the migrations in the tails

of the distribution do not affect the final results.

7.5 Summary

The resolution of the $\ln(1/x_p)$ measurement is dominated by the reconstruction of the boost from the laboratory to the Breit frame rather than the track reconstruction. Furthermore, it is the resolution with which the scattered electron energy is determined within the double-angle formula which governs the quality of the boost and not the angular resolution of the scattered electron. This is most noticeable at low y where the x resolution deteriorates. The consequences of misreconstructing the boost are migrations from the current to the target region. The chosen width of the $\ln(1/x_p)$ bins, 0.25 $\ln(1/x_p)$ units, is commensurate with the resolution around the peak position over a large area of the kinematic plane.

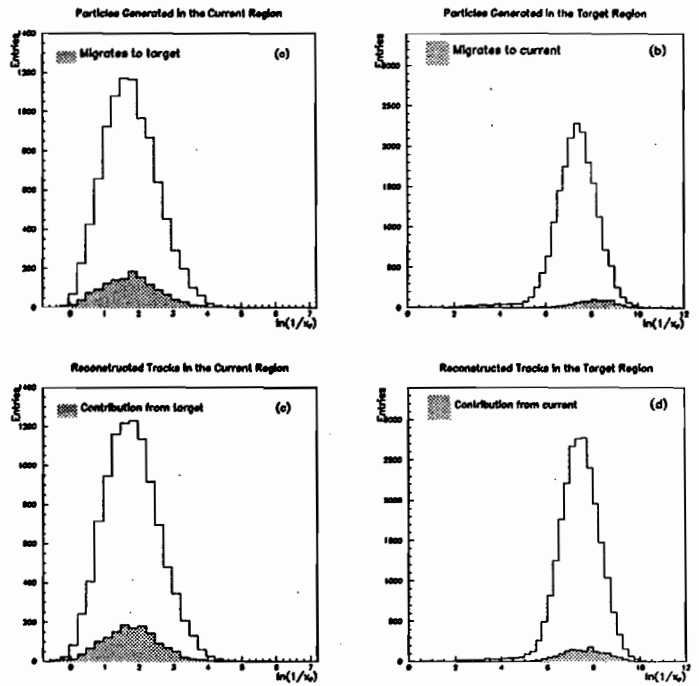

Figure 7.7: *Top:- True particle* $\ln(1/x_p)$ *distributions in the current (a) and target (b) regions. The shaded area indicates the* $\ln(1/x_p)$ *distribution of the particles which migrate to the other region when the boost is reconstructed. Bottom:- Reconstructed* $\ln(1/x_p)$ *distributions in the current (c) and target (d) regions. The shaded area highlights the contribution from particles generated in the other region which have migrated in due to the boost reconstruction.*

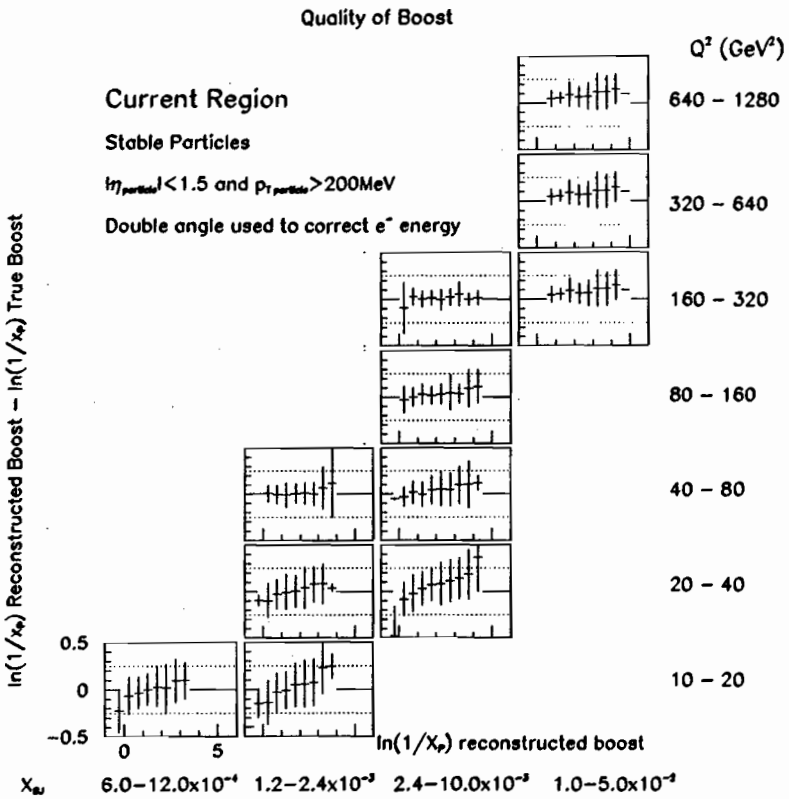

Figure 7.8: *Profile plot of the resolution of* $\ln(1/x_p)$ *as a function of* $\ln(1/x_p)$ *due to the boost reconstruction.*

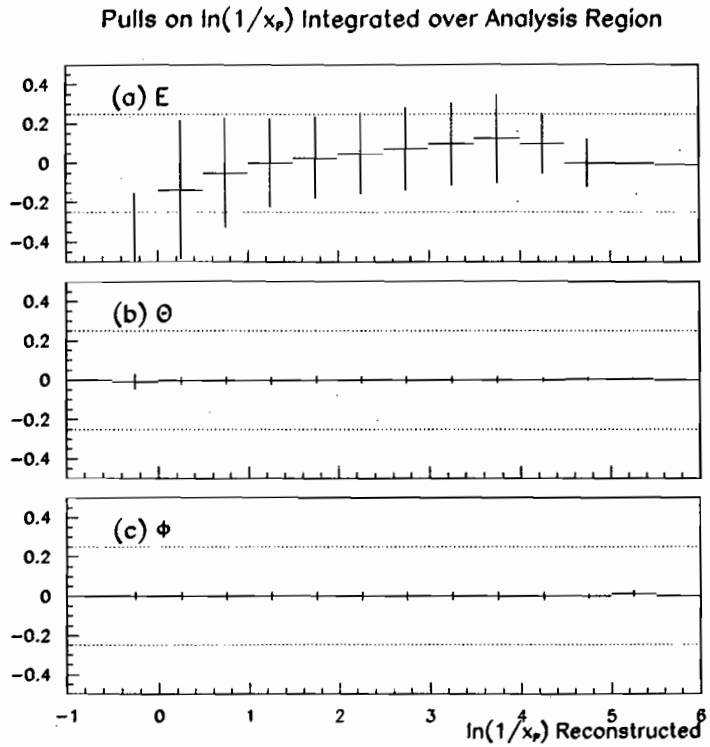

Figure 7.9: *Pulls on* $\ln(1/x_p)$ *due to the reconstruction of individual electron components. In (a) the electron energy is the only reconstructed quantity; in (b) it is the polar angle* θ*; and in (c) it is the azimuthal angle,* ϕ*. The plots are integrated over the analysis region.*

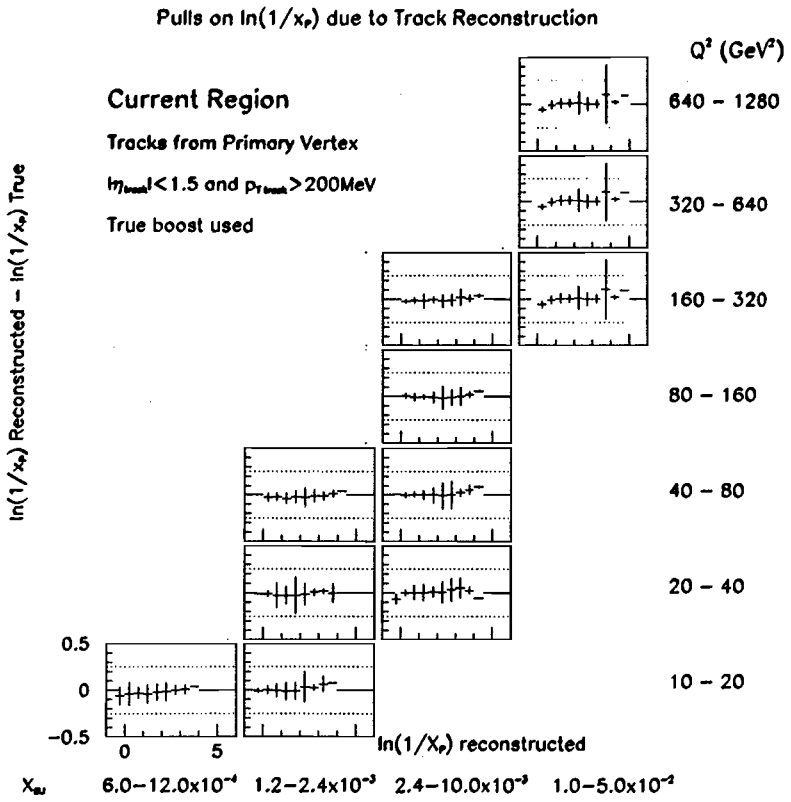

Figure 7.10: *Profile plot of the resolution of* $\ln(1/x_p)$ *as a function of* $\ln(1/x_p)$ *due to track resolution effects.*

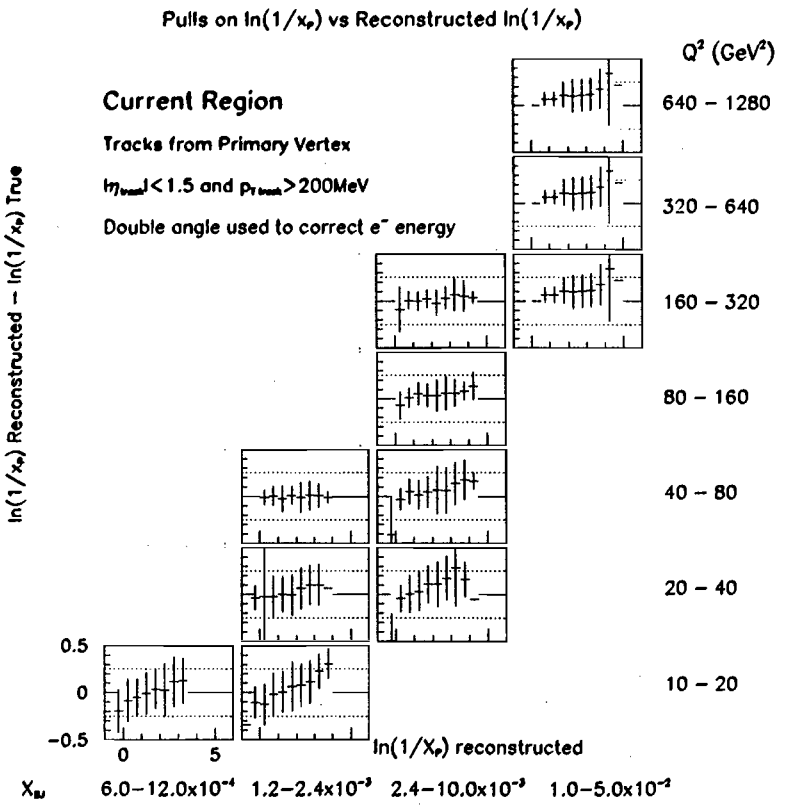

Figure 7.11: *Profile plot of the resolution of* $\ln(1/x_p)$ *as a function of* $\ln(1/x_p)$ *due to the combined effects of the transformation and tracking. The dashed line indicates the adopted* $\ln(1/x_p)$ *binwidth.*

Chapter 8

Scaled Momentum Distributions

8.1 Uncorrected Data

The observed scaled momentum distributions are shown in figure 8.1, uncorrected for effects due to detector acceptance and resolution. The measurements are from tracks measured in the CTD which are associated to the primary vertex and satisfy $p_T > 200$ MeV and $|\eta| < 1.5$ where $\eta = -\ln(\tan\theta/2)$ corresponding to the polar region between 25° and 155°. The tracks have been boosted and assigned to the current region of the Breit frame by virtue of their longitudinal momentum component in the boosted frame, $p'_z < 0$. The boost to the Breit frame has been reconstructed using the scattered electron energy and kinematic quantities x and Q^2 derived from the double angle method.

In figure 8.1 the data are binned in 11 ranges of x and Q^2 and shown with statistical errors only. The arithmetic mean and integral under the curve, given by ALLCHAN × BINWIDTH (= 0.25 units), which represents the mean charged track multiplicity are also shown.

The uncorrected distributions are approximately Gaussian in shape with a broad maximum. In the x ranges considered an increase of the mean position and multiplicity as Q^2 increases is observed. In the Q^2 regions in which two

measurements in different x bins are made, slight differences between the means and multiplicities are observed. At $160 < Q^2 < 320$ GeV^2 the distribution in the highest x bin is substantially smaller than the corresponding spectrum at the lower value of x. This is later shown to be an artifact of the detector acceptance in this region.

8.2 Data Correction

The uncorrected distributions shown in figure 8.1 are a convolution of the underlying physical distribution of charged hadrons convoluted with detector and reconstruction effects. Event and track selection criteria, in addition, will directly modify the "true" distribution. The Monte Carlo samples described in chapter 5 were used to correct the data and provide a quantitative determination of the detector and reconstruction effects.

To determine how well the four Monte Carlos describe the data, a comparison of the uncorrected $\ln(1/x_p)$ distribution obtained from the selected data integrated over the (x, Q^2) range covered by this analysis and results from the four reconstructed Monte Carlo samples are shown in figure 8.2. The Monte Carlo data have been passed through the full detector simulation and reconstruction programs and are plotted in the current region integrated over the same (x, Q^2) range.

All the Monte Carlo models provide a good description of the peak position within the measured $\ln(1/x_p)$ resolution. Differences between the models and the data are observed in terms of the average charged particle multiplicity. ARIADNE provides a good overall description of the data but underestimates the multiplicity around the peak position. The inclusion of a 10% contribution of POMPYT events to the ARIADNE sample better describes the data. The MEPS prediction for the particle multiplicity exceeds the observed data distribution while the HERWIG Monte Carlo underestimates the data.

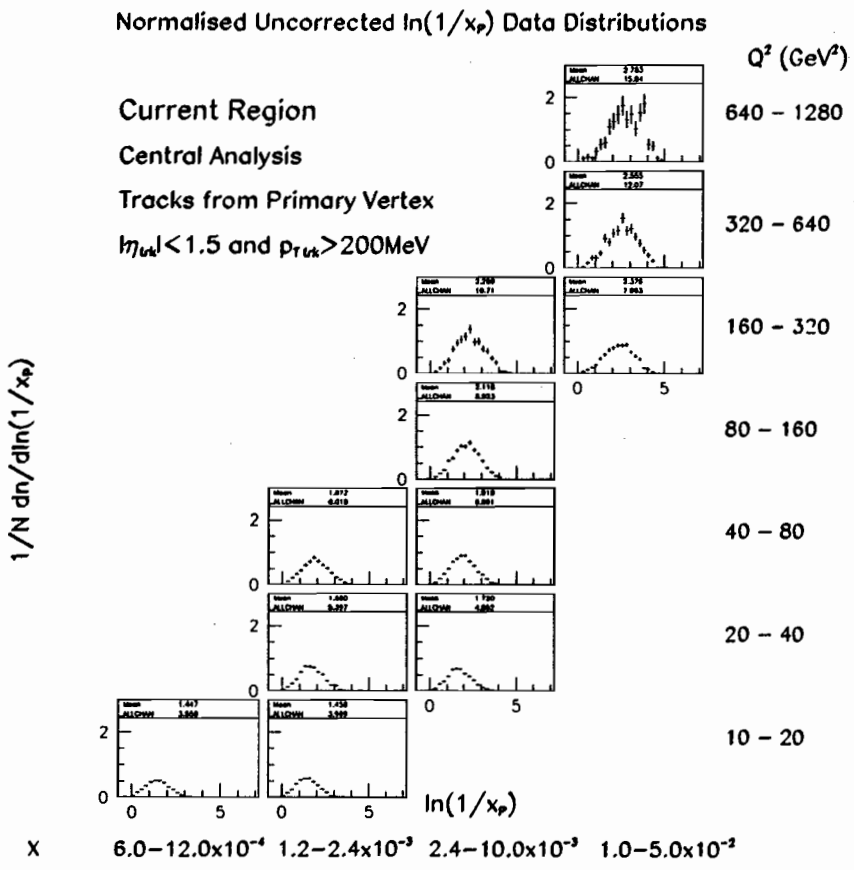

Figure 8.1: *Uncorrected data in the eleven x,Q^2 bins selected. The data are shown with statistical errors only. The arithmetic mean and the integral under the curve* ALLCHAN× BINWIDTH *corresponding the to average charged particle multiplicity are shown.*

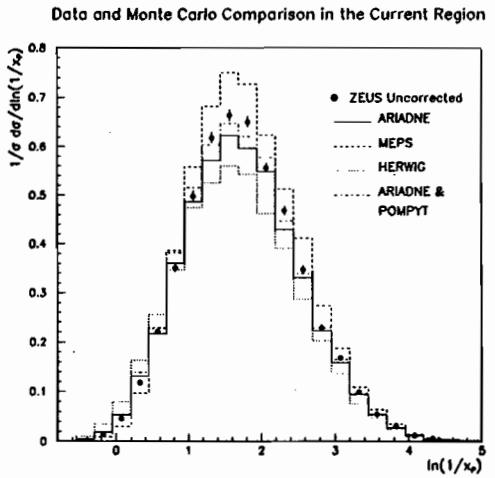

Figure 8.2: *Comparison of the uncorrected* $\ln(1/x_p)$ *distribution from data and four Monte Carlo samples at the detector level.*

The ARIADNE sample, which provides the best description of energy flow measurements at ZEUS, was used in the central analysis to correct the data. Correcting the data with the other Monte Carlo samples, however, was used to test the sensitivity of the results to the model used.

The data were corrected bin-by-bin by first calculating a correction factor $F(i)$ for each bin which is then applied to the uncorrected data. The bin-by-bin correction factors were obtained from the Monte Carlo by comparing the "true" generated distributions, $n_{gen} = n_{gen}(\ln(1/x_p)) = dn/d\ln(1/x_p)$, with the "observed" distributions, $n_{obs} = n_{obs}(\ln(1/x_p)) = dn/d\ln(1/x_p)$.

The generated distributions were constructed from stable charged particles in the final state. Charged particles produced in the decay of K^0_S and Λ were not included, irrespective of their distance from the interaction point. Neither

were charged particles produced from weakly decaying particles with a lifetime $> 10^{-8}$ s. These distributions, were generated in the true current region using the true mass of the produced hadrons for the boost, and in the true x and Q^2 bins selected for their high acceptance.

For every $\ln(1/x_p)$ bin, i, the correction factors were calculated

$$F_i(\ln(1/x_p)) = \frac{n^i_{gen}}{N^i_{gen}} \Big/ \frac{n^i_{obs}}{N^i_{obs}} \tag{8.1}$$

where N^i_{gen} (N^i_{obs}) are the number of generated (observed) Monte Carlo events in the i^{th} bin.

The statistical errors were calculated assuming that the generated and reconstructed events were independent.

$$\sigma_{F_i} = \left(\frac{1}{N_{gen}(i)} + \frac{1}{N_{obs}(i)}\right)^{\frac{1}{2}} . F_i \tag{8.2}$$

This is an upper estimate of the statistical error as the two will exhibit a large degree of correlation.

In order that the bin-by-bin correction technique is valid, the width of the $\ln(1/x_p)$ bins has been chosen to be larger than the RMS resolution of $\ln(1/x_p)$ as shown in chapter 7 to ensure that migrations between the bins are small. The correction factors, F_i, should be $\simeq 1$ to ensure that the correction technique is justified. Otherwise the corrected data would be unduly biased by the Monte Carlo model which is being used to correct the data.

Using the definition of F_i in equation 8.1, the correction factors account for the following effects:

- Acceptance effects due to the geometry of the detector and its efficiency;
- Event selection and reconstruction;
- Track selection and reconstruction;
- QED radiative effects;

- Migration between x,Q^2 bins;
- Migration between the current and target region;
- Migration between bins in $\ln(1/x_p)$; and
- Tracks from the decay products of K^0_S and Λ which are assigned to the primary vertex.

Figure 8.3 shows the measured correction factors obtained with the default event and track selection used in the central analysis. The correction factors are typically $\simeq 1.3$ around the peak of the uncorrected $\ln(1/x_p)$ distributions and are flat in this region. At high values of $\ln(1/x_p)$, *ie* low momentum, the correction factors rise due to the $p_T > 200$ MeV cut imposed on the reconstructed tracks. This cut suppresses the low momentum tail present in the generated Monte Carlo $\ln(1/x_p)$ distributions.

At $160 < Q^2 < 320$ GeV^2 and $1.0\times10^{-2} < x < 5.0\times10^{-2}$ the correction factors are typically 1.8-2.0 which is unacceptably high. In this region the $|\eta| < 1.5$ track cut removes a substantial proportion of the tracks resulting in this low acceptance. Events in this region were therefore removed from the analysis.

Corrected data distributions were then obtained by multiplying the observed data distributions by these correction factors. Figure 8.4 shows the corrected data in the x, Q^2 bins with statistical errors only. Since the data and correction factors are measured independently the statistical errors were added in quadrature. The corrected data have higher means and multiplicities than the uncorrected data and the x dependence of the corrected measurements is less pronounced.

8.3 Mean Multiplicity

The mean charged particle multiplicity, $<n_{ch}>$, was determined as previously described from the integral under the corrected scaled momentum distributions.

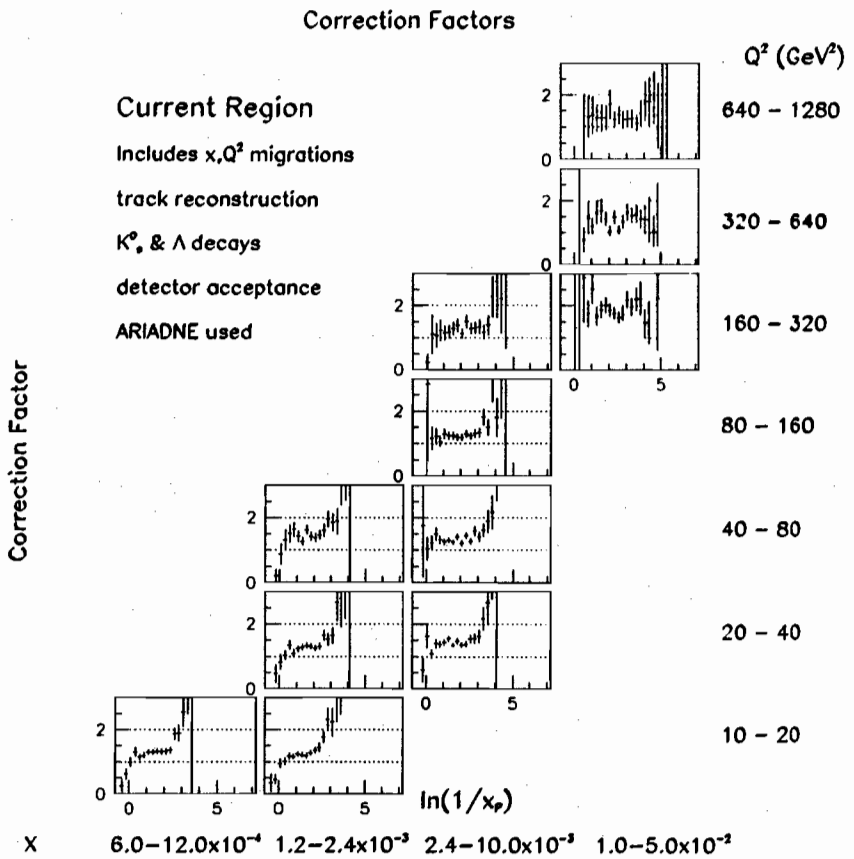

Figure 8.3: *Correction factors calculated from ARIADNE Monte Carlo.*

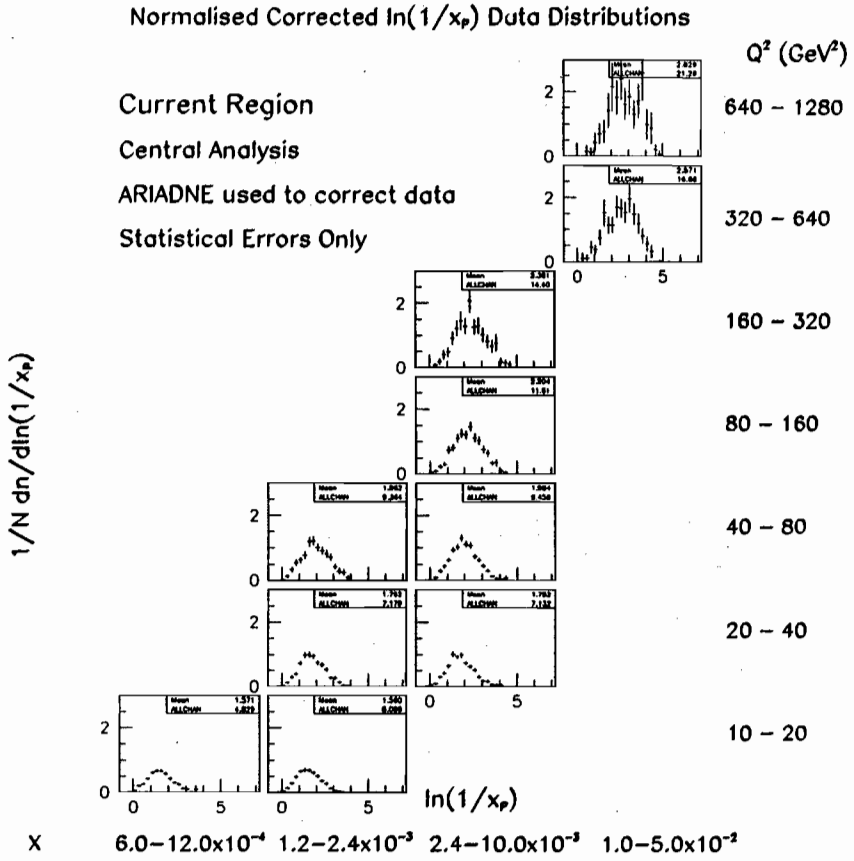

Figure 8.4: *Corrected data in the x,Q^2 bins with statistical errors only.*

The results tabulated in table 8.1 agree within $1-2\sigma$ of the statistical errors from preliminary ZEUS multiplicity data [57] in which a matrix correction technique is applied. A comparison of the results was made to multiplicity data from e^+e^- annihilation experiments at different $\sqrt{s}$. These experiments published their inclusive charged particle multiplicity data excluding the contribution from secondary K^0_S and Λ decays [58, 59, 60, 61].

x range	Q^2 (GeV2) range	$\langle Q \rangle$ (GeV)	$\langle n_{ch} \rangle \pm$ stat
$6.0 - 1.2 \times 10^{-4}$	10-20	3.75	1.21 ± 0.02
$1.2 - 2.4 \times 10^{-3}$	10-20	3.78	1.27 ± 0.02
	20-40	5.28	1.79 ± 0.04
	40-80	7.28	2.34 ± 0.07
$2.4 - 10.0 \times 10^{-3}$	20-40	5.31	1.78 ± 0.03
	40-80	7.37	2.36 ± 0.05
	80-160	10.45	2.90 ± 0.08
	160-320	14.46	3.60 ± 0.21
$1.0 - 5.0 \times 10^{-2}$	320-640	20.44	4.22 ± 0.29
	640-1280	29.19	5.32 ± 0.62

Table 8.1: *Average charged-particle multiplicities evaluated from the* $\ln(1/x_p)$ *distributions. Statistical errors only are shown.*

Following equation 4.12, the inclusive multiplicities from e^+e^- were halved to compare to the DIS results in the current region of the Breit frame. The evolution with $\langle Q \rangle$ is shown in figure 8.5 with statistical error bars only.

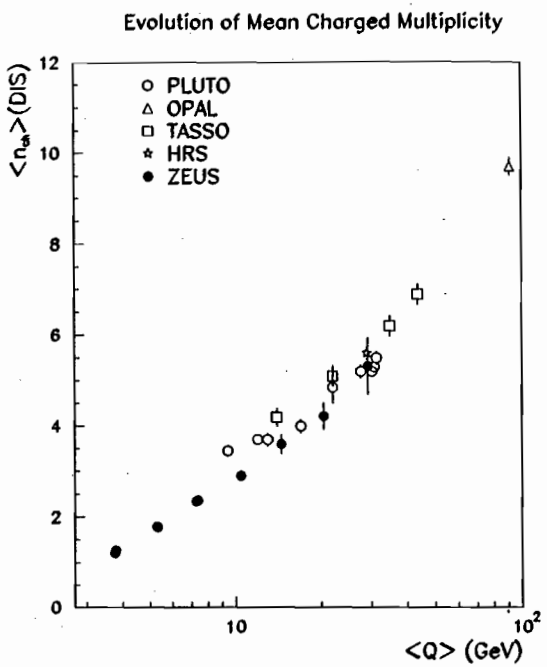

Figure 8.5: *Evolution of the average charged particle multiplicity in the current region of the Breit frame as a function of* $\langle Q \rangle$*. The data are compared to half the inclusive multiplicity in* e^+e^- *data.*

8.3.1 Comparison of $\langle n_{ch} \rangle$ with e^+e^- Data

In DIS the scattering is predominantly from light quarks. The contribution from heavy quarks is suppressed in comparison to the e^+e^- annihilation case. To ascertain if the different flavour composition of the two physics processes could affect the comparison of these measurements a Monte Carlo study of heavy quark production was made using JETSET. Events were generated at PETRA and LEP energies for the processes:

- $e^+e^- \rightarrow q\bar{q}$, where $q = u, d$ or s; and
- $e^+e^- \rightarrow q\bar{q}$, where $q = u, d, s, c$ or b.

The comparison of the scaled momentum distributions of charged particles produced in the 3 and 5-flavour processes is shown in figure 8.6. The results illustrate that the peak position and multiplicity are relatively insensitive to the flavour of the primary quark at the centre-of-momentum energies considered. Furthermore, results from OPAL on the $< n_{ch} >$ from a selected sample of b quarks indicate that the difference between the multiplicity from b quarks and u, d, s and c [62] is within the quoted statistical and systematic errors from the preliminary ZEUS measurement in reference [57]. Heavy flavour production does not therefore account for the observed differences between the DIS and e^+e^- data at low values of $<Q>$.

In figure 8.5 the highest values of $< Q >$, the DIS data are in reasonable agreement with the e^+e^- data only at high values of $<Q>$. At lower values of $<Q>$, however, $<n_{ch}>$ from the DIS data asymptotically approaches zero. This is a direct consequence of hard emissions "pulling" particles from the current region into the target region as discussed in chapter 4. These gluon emissions give rise to the topologies which can deplete the current region of particles and are more prevalent at low (x, Q^2) due to the increased target region phase space and the increased strong coupling.

8.4 Systematic Checks

A series of systematic checks was performed to investigate the sensitivity of the results to features of the central analysis. These can be categorised under event selection, track and vertex reconstruction, track selection, and data correction methods.

The sensitivity to these various systematic effects is discussed in the following

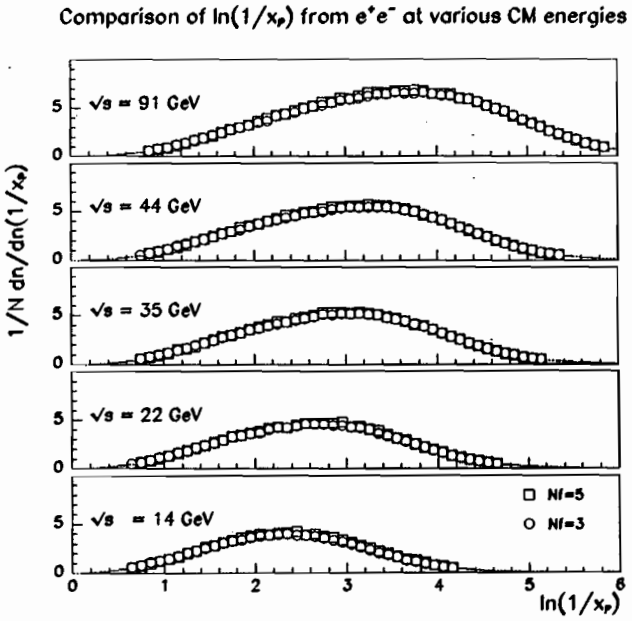

Figure 8.6: *Comparison of the scaled momenta spectra from generated $e^+e^- \rightarrow q\bar{q}$ for 3 and 5 primary quark flavours. The distributions are plotted at PETRA and LEP $\sqrt{s}$ energies.*

subsections in terms of the position of the peak of the $\ln(1/x_p)$ distributions. The peak position is determined by fitting a Gaussian over a limited range around the peak and is fully discussed in section 8.5. The peak determination is itself subject to systematic uncertainty.

To quantitatively study the influence of the aforementioned sources, the analysis was repeated under the following conditions.

1. The value of the cut on $\delta = E - p_z + 2E_\gamma$ was raised from 35 GeV to 40 GeV.

2. The value of the cut on y_{elec} was lowered from 0.95 to 0.8.

3. The value of the cut on y_{JB} was increased from 0.04 to 0.05.

4. The track and vertex reconstruction were performed using a different tracking algorithm.

5. The p_T cut applied to tracks was lowered from 200 MeV to 100 MeV.

6. The η cut applied to tracks was removed.
   Conditions 1-6 above were applied to both the observed Monte Carlo and data distributions.

7. In the Monte Carlo the energies of the calorimeter cells associated with the identified scattered electron were scaled by a factor of 0.96.

8. The Monte Carlo model used to correct the data was MEPS.

9. The Monte Carlo model used to correct the data was HERWIG.

10. A 10% sample of diffractive events was added to the ARIADNE Monte Carlo used to correct the data.

11. The peak position was determined by fitting over various ranges of data points.

Photoproduction Background

As discussed in chapter 6 photoproduction events provide a large source of background to the DIS events. In such events, the scattered electron is not detected in the calorimeter since the virtuality of the exchanged photon $Q^2 \rightarrow 0$. However, the scattered electron signal may be faked by electromagnetic shower formation produced from $\pi^0 \rightarrow \gamma\gamma$ decays. The kinematic variables and the boost to the Breit frame will be completely wrong in these cases. To ascertain

the sensitivity to possible residual photoproduction contamination in the data sample the selection cuts were tightened. Increasing δ from 35 GeV to 40 GeV produced a maximum shift of 2% on $\ln(1/x_p)_{max}$ in any of the (x, Q^2) intervals. A 3% change in $\ln(1/x_p)_{max}$ was the most significant shift observed when decreasing the y_{elec} cut from 0.95 to 0.8.

Calorimeter Noise

The y_{JB} cut was raised from 0.04 to 0.05 to study the effect of increasing the resolution of the hadronic angle γ_h which feeds into the double angle reconstruction of x and Q^2. The effect of this on the position of the $\ln(1/x_p)$ peak was $< 1\%$

Tracking System

Features of the tracking system such as its operation and the track reconstruction techniques employed are likely to be a source of systematic uncertainty in such a measurement. Physics runs in which the CTD suffered operational failures have already been excluded from the analysis. The hardware efficiency of the CTD has been measured at $> 93\%$ throughout the running period as discussed in chapter 2, so uncertainties due to detector inefficiency will be small. Of more significance to the measurement are uncertainties due to the tracking algorithm. These were determined by using a different track reconstruction package, TGTRAK, which employs pattern recognition, track fitting and vertex finding algorithms which were developed separately from the default package. As well as providing independent momentum measurements the TGTRAK vertex was used in the event selection. Fewer event vertices satisfied the event selection cut $-50 < z_{vtx} < 40$ cm and fewer electrons were identified using this vertex.

The tracking algorithm was found to be a significant source of systematic uncertainty particularly in the x range between 2.4×10^{-3} and 1.0×10^{-2}. The systematic differences of the maxima in this range were typically 3% but were

as large as 9% in the highest Q^2 bin in this x region. These shifts were greater than one standard deviation from the central values and just within two standard deviations. In the lower and higher x regions, the systematic shifts were within statistical error limits.

Track Cuts

The effect of the track cuts was studied by separately lowering the p_T cut to 100 MeV and removing the η cut. The largest change on the position of the maxima was $< 1\%$ in all bins rising to $\simeq 2\%$ in the highest x bins. Removing the η cut has little affect since the analysis bins were chosen such that $|\eta(\gamma_h)| < 1.5$.

Electron Energy Scale

The electron energy spectrum is expected to have a kinematic peak at the electron beam energy. The location of this peak provides a good test for the understanding of the electromagnetic calorimeter energy scale. As documented in [63] there is a disagreement between the electron energy spectrum obtained from Monte Carlo and data. The kinematic peak found in Monte Carlo is shifted to a value $\simeq 4\%$ higher with respect to data. Although the electron energy used to calculate the boost is determined by the double angle method which does not depend directly on the electron energy scale, the selection cuts do use the electron energy as measured in the calorimeter. This may introduce some sensitivity of the measurement to the electron energy scale. In the Monte Carlo the energy of the calorimeter cells associated with the electron were scaled by a factor of 0.96 of their measured values. The selection cuts described in chapter 6 were applied and the scaled electron was used to determine the four-momentum of the virtual photon for the boost. The scaled Monte Carlo was then used to correct the data. The largest change to the maximum of the $\ln(1/x_p)$ distribution is 0.2%, a negligible effect.

Different Monte Carlos to Correct the Data

Different Monte Carlo models were used to determine the systematic uncertainty which arises due to unfolding the data using ARIADNE. Using several models which simulate the hadronic final state in different ways also implicitly tests the boost reconstruction as it depends on the kinematic quantities derived from the hadronic activity within the detector.

The data were corrected with

- 200 K MEPS events with electroweak radiative corrections.
- 100 K HERWIG events with no radiative corrections.

Both the MEPS and HERWIG reasonably reproduce the main characteristics of the observed hadronic final state but do not describe the data as well as ARIADNE. Indeed, figure 8.2 shows that MEPS tends to overestimate the particle multiplicity whilst HERWIG underestimates the data.

The changes to the $\ln(1/x_p)_{max}$ values are generally less than 2% and within 1σ of the quoted statistical error rising to 7% for MEPS in the high x, high Q^2 bin where statistics from the Monte Carlo are low. The differences arising from HERWIG are generally higher, $\simeq 5-6\%$ but are typically consistent with statistical fluctuations due to the lack of Monte Carlo statistics.

Rapidity Gap Events

As discussed in chapter 5 diffractive events which have a Large Rapidity Gap (LRG), defined as those events with a maximum pseudorapidity $\eta_{max} < 1.5$, are not included in the ARIADNE Monte Carlo sample used to correct the data. The LRG events populate the low x, low Q^2 part of the kinematic plane forming a non-negligible contribution in this region. To determine the effect of omitting the LRG events from the Monte Carlo on the corrected distributions, the data were

also unfolded with a mixture of 90% ARIADNE and 10% POMPYT. The change to the $\ln(1/x_p)_{max}$ values was < 1%.

Figures 8.7(a), (b) and (c) illustrate the uncorrected $\ln(1/x_p)$ data distributions for events without a large rapidity gap $\eta_{max} > 1.5$; with a LRG $\eta_{max} < 1.5$; and all events respectively. The distributions are normalised to the number of events belonging to each class and plotted in the lowest x, Q^2 bin where the contribution of diffractive events to the inclusive distribution is greatest. The differences between the two classes of events are greatest in this bin. For $Q^2 \gtrsim 100$ GeV^2 the number of LRG events is negligible.

The large rapidity gap events in figure 8.7(b) have a mean value of $\ln(1/x_p)$ shifted to a lower value of $\ln(1/x_p)$ and a higher particle multiplicity in the current region in comparison to the non-LRG events. Whilst the inclusive particle multiplicity from LRG events is smaller than the non-LRG events due to the lack of QCD radiation between the struck quark and proton remnant, it is the lack of QCD radiation which stops particles being pulled from the current region into the target region. The LRG events therefore have a higher particle multiplicity and a harder momentum spectrum in the current region than the non-LRG events.

Figure 8.7(e) is the ratio of the non-LRG distribution over the total distribution. This ratio is flat at approximately 0.95 indicating that whilst there is a significant difference between the LRG and non-LRG events, the contribution of the LRG events to the inclusive DIS sample is small.

8.4.1 Combined Systematic Uncertainty

The overall effect of the systematic errors on the individual data points is shown in figure 8.8. The inner error bars represent the statistical errors. The outer bars show the statistical errors added in quadrature with the overall systematic errors which were determined by combining in quadrature each of the aforementioned systematic uncertainties. These represent therefore a conservative estimate of

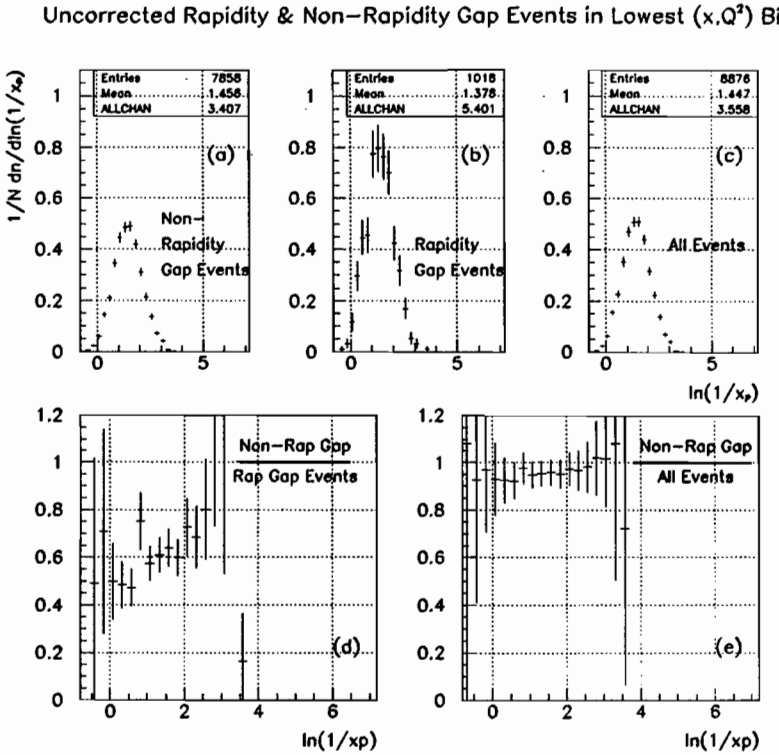

Figure 8.7: *Comparison of uncorrected data from events with and without a large rapidity gap in the region* $6.0 \times 10^{-4} < x < 1.2 \times 10^{-3}$ *and* $10 < Q^2 < 20$ GeV^2 *where the population of LRG events is greatest.*

the systematic uncertainty on the measurements. Tables of corrected $\ln(1/x_p)$ data with statistical and systematic errors are given in appendix B. The largest contribution to the combined systematic uncertainty is the error associated with the different Monte Carlo models and the alternative tracking algorithm.

8.5 Fitting the Distribution

In order to measure the peak position of the $\ln(1/x_p)$ distributions, the OPAL collaboration fitted a distorted Gaussian distribution (see equation 8.5) to OPAL [26] and TASSO [25] data over a limited range around the peak [64]. The form of the distorted Gaussian was suggested by Webber and Fong [65] and its five free parameters can be calculated in the MLLA. For consistency, it is desirable to perform an equivalent fit to the DIS data in order to compare to the published OPAL and TASSO results. However the majority of data measured at ZEUS is at low Q values where the width of the scaled momentum distributions is smaller than the distributions measured at the e^+e^- experiments. Combined with the relatively poorer resolution on the $\ln(1/x_p)$ measurement which is limited by the boost to the Breit frame, there are very few degrees of freedom left after restricting the fit to a limited range around the peak.

Two solutions have been studied:

- fit a standard three parameter Gaussian across a limited range around the peak to ZEUS, TASSO and OPAL data; and
- fit the distorted Gaussian across an increased range of points.

8.5.1 Fitting a Gaussian

Inspired by the MLLA, the distribution can be approximated by a Gaussian distribution close to the peak:

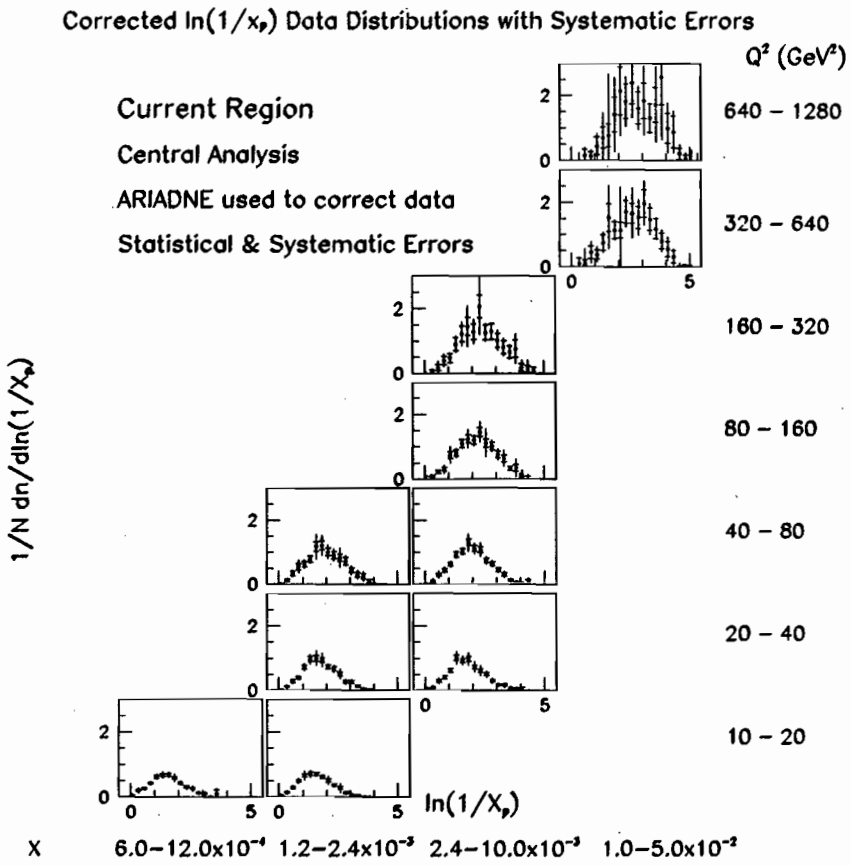

Figure 8.8: *Corrected data in the x,Q^2 bins with all systematic errors added in quadrature with the statistical errors.*

$$\frac{1}{\sigma}\frac{\mathrm{d}\sigma}{\mathrm{d}\ln(1/x_p)} = N(Y)\left(\frac{36N_c}{\pi^2 bY^3}\right)^{1/4}\exp\left[-\sqrt{\frac{36N_c}{b}}\frac{(\ln(1/x_p)-\ln(1/x_p)_{\max})^2}{Y^{3/2}}\right] \tag{8.3}$$

where $Y = \ln(Q/2\Lambda_{\mathrm{EFF}})$, and $b = \frac{11}{3}N_c - \frac{2}{3}N_f$ is a constant which depends on the number of colours, N_c, and flavours N_f. $N(Y)$ is the average charged particle multiplicity which is predicted by the theory.

The peak position of the distributions, $\ln(1/x_p)_{\max}$, was evaluated by fitting a Gaussian across a range

$$\overline{\ln(1/x_p)} - 1 < \ln(1/x_p) < \overline{\ln(1/x_p)} + 1 \tag{8.4}$$

where $\overline{\ln(1/x_p)}$ is the arithmetic mean of the distribution. The fit was restricted to a limited range since a Gaussian fit across the full $\ln(1/x_p)$ range does not provide a good description of the data as Q increases.

A variety of fit ranges around the mean was considered. The region ± 1 unit was finally chosen for the central analysis as it provides a substantial number of points on either side of the peak position for both e^+e^- and ZEUS data to which the functional form can be fitted.

The systematic uncertainty on the position of $\ln(1/x_p)_{\max}$ was evaluated by fitting each distribution over various regions around the peak. For the ZEUS data the fit range was extended/reduced by 1 bin on either/both sides of the fit range. The largest deviation from the central value which still provided a reasonable description of the peak was taken as the systematic deviation. For ZEUS data the systematic uncertainty due to the range considered was typically 0.035-0.090 in each bin. Despite the higher $\ln(1/x_p)$ resolution offered by the e^+e^- experiments the systematic uncertainty on the $\ln(1/x_p)_{\max}$ positions due to the fit was also estimated at 0.030-0.060 by altering the fit range in the same way.

Figures 8.9(a)-(c) show three example corrected $\ln(1/x_p)$ distributions in bins of increasing Q^2, the Gaussian fit and the resulting fit parameters. Figure 8.9(a)

is a typical example of the distribution at low x and Q^2. The fit provides a good description of the data and the χ^2/dof is small. In (c), at high Q^2, the low statistics results in the fits having increasing larger errors. Here the σ of the distribution is smaller than the range over which the Gaussian is fitted. In this region the distribution is pulled by the statistical fluctuations of the data in the region around the peak. Figure 8.10 shows the same fit to the TASSO and OPAL data. The data around the peak are well described by the fit and the measured peak positions agree to within statistical errors with those given in reference [64].

x range	Q^2 (GeV^2) range	Q (GeV)	$\ln(1/x_p) \pm$ stat $\pm$ sys	χ^2/dof
$6.0 - 1.2 \times 10^{-4}$	10-20	3.75	$1.485 \pm 0.024 \pm 0.062$	8.19/6
$1.2 - 2.4 \times 10^{-3}$	10-20	3.78	$1.499 \pm 0.028 \pm 0.058$	4.71/6
	20-40	5.28	$1.699 \pm 0.029 \pm 0.060$	8.93/6
	40-80	7.28	$1.941 \pm 0.055 \pm 0.111$	4.40/6
$2.4 - 10.0 \times 10^{-3}$	20-40	5.31	$1.699 \pm 0.027 \pm 0.091$	12.50/6
	40-80	7.37	$1.923 \pm 0.034 \pm 0.069$	5.81/6
	80-160	10.45	$2.180 \pm 0.057 \pm 0.096$	3.22/6
	160-320	14.46	$2.254 \pm 0.100 \pm 0.233$	3.97/6
$1.0 - 5.0 \times 10^{-2}$	320-640	20.44	$2.776 \pm 0.224 \pm 0.258$	3.82/6
	640-1280	29.19	$2.850 \pm 0.210 \pm 0.237$	5.62/8

Table 8.2: *Fitted values of* $\ln(1/x_p)_{\max}$ *from a Gaussian fit over* ± 1 $\ln(1/x_p)$ *unit of the statistical mean. The systematic errors are determined by combining all the systematic effects in quadrature.*

Results of the fits are shown in tables 8.2 and 8.3. The ZEUS systematic error includes the contribution from refitting the data from the systematic checks listed in section 8.4 and are combined in quadrature with the uncertainty from

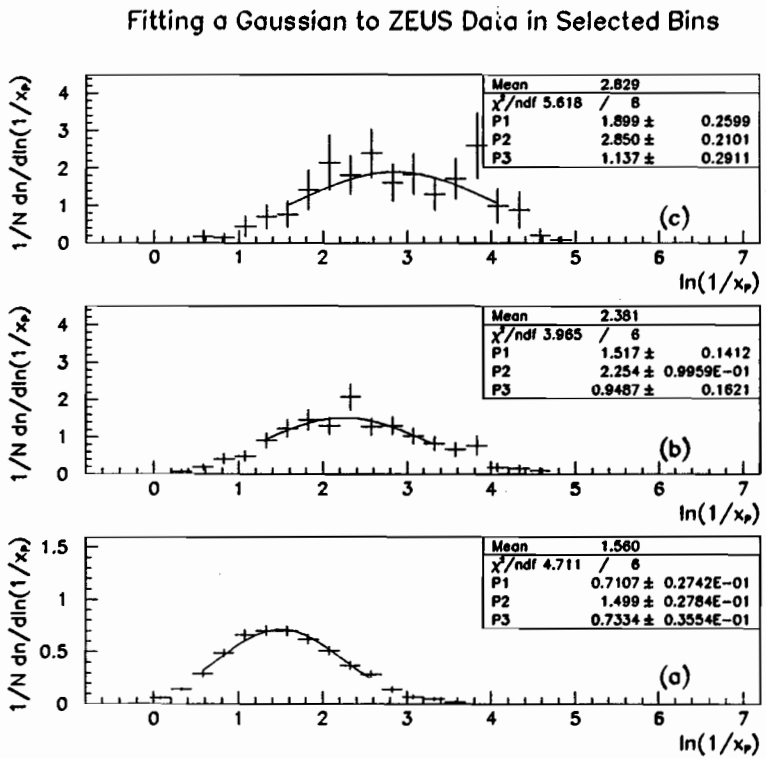

Figure 8.9: *Corrected ZEUS* $\ln(1/x_p)$ *distributions measured in a)*$1.2 \times 10^{-3} < x < 2.4 \times 10^{-3}$ *and* $10 < Q^2 < 20$ *GeV*^{2} *b)*$1.0 \times 10^{-3} < x < 1.0 \times 10^{-2}$ *and* $160 < Q^2 < 320$ *GeV*^{2} *c)*$1.0 \times 10^{-2} < x < 5.0 \times 10^{-2}$ *and* $640 < Q^2 < 1280$ *GeV*^{2}. *The Gaussian fit over the range* ± 1 $\ln(1/x_p)$ *unit of the statistical mean is shown together with the parameters of the fit.*

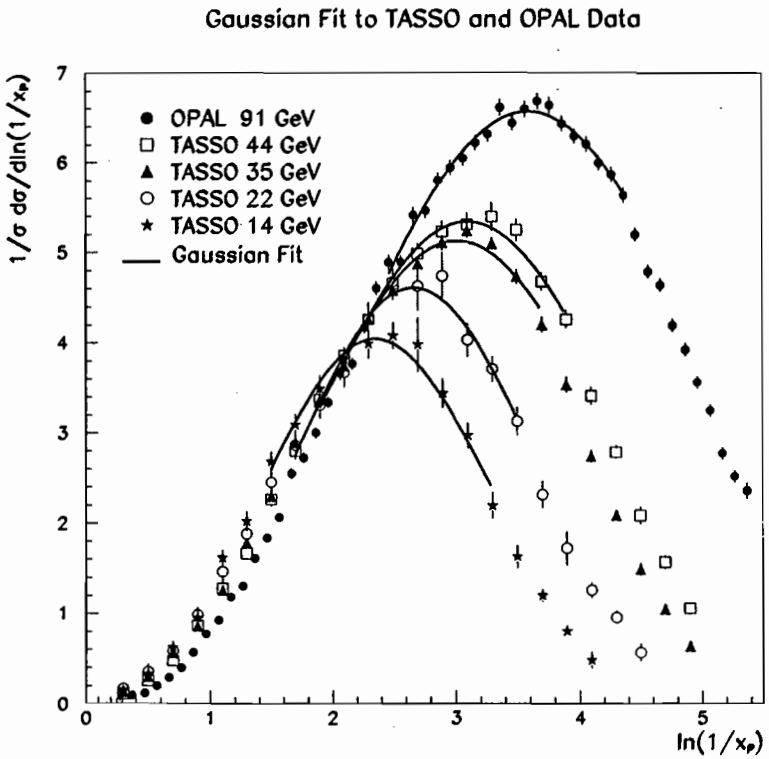

Figure 8.10: $\ln(1/x_p)$ *distributions measured by OPAL and TASSO at different CM energies. A Gaussian fit over* ± 1 $\ln(1/x_p)$ *unit around the statistical mean is shown.*

Experiment	E_{CM} (GeV)	$\ln(1/x_p) \pm$ stat $\pm$ sys	χ^2/dof
TASSO	14	$2.356 \pm 0.022 \pm 0.045$	3.87/7
	22	$2.667 \pm 0.024 \pm 0.030$	4.11/7
	35	$3.020 \pm 0.018 \pm 0.030$	15.28/7
	44	$3.104 \pm 0.021 \pm 0.033$	4.56/7
OPAL	91	$3.594 \pm 0.013 \pm 0.050$	19.14/17

Table 8.3: *Maxima obtained by fitting a Gaussian distribution to TASSO and OPAL data. The systematic errors quoted here arise only from the fit range considered.*

varying the fit range. The relative contribution to the overall systematic error from the fit variation is $\simeq$ 40%. The systematic errors associated to the OPAL and TASSO data given in table 8.3 are from the fit variation only.

In general, the Gaussian fit provides a good description of both the ZEUS and e^+e^- data.

8.5.2 Fitting a Distorted Gaussian

As a check on the results from fitting the Gaussian distribution to the data, a second function, also motivated by the MLLA, was fitted. The second expression for the $\ln(1/x_p)$ spectrum results in a distorted Gaussian

$$g = \frac{1}{\sigma}\frac{d\sigma}{d\ln(1/x_p)} \simeq N \times \exp\left[\frac{1}{8}k - \frac{1}{2}s\delta - \frac{1}{4}(2+k)\delta^2 + \frac{1}{6}s\delta^3 + \frac{1}{24}k\delta^4\right] \quad (8.5)$$

where $\delta = [\ln(1/x_p) - \overline{\ln(1/x_p)}]/\sigma$ and $\overline{\ln(1/x_p)} = m$ is the mean of the $\ln(1/x_p)$ distribution which in the MLLA is shifted with respect to the peak position. The coefficients N, σ, s and k are the normalisation, width, skewness and kurtosis of the Gaussian distribution and are predicted in the MLLA.

Equation 8.5 was fitted to both the ZEUS and the e^+e^- data distributions over the range $0 < \ln(1/x_p) < \ln(Q/2\Lambda_{EFF})$ in which equation 8.5 is valid. N, σ, s, k and m were taken as free parameters in the fit. The starting values of N, m and σ were chosen by fitting a Gaussian over the full range of data.

The peak position was evaluated by substituting $y = \frac{1}{8}k - \frac{1}{2}s\delta - \frac{1}{4}(2+k)\delta^2 + \frac{1}{6}s\delta^3 + \frac{1}{24}k\delta^4$ and differentiating equation 8.5. The maximum is then given by

$$\frac{\partial g}{\partial \ln(1/x_p)} = \frac{\partial g}{\partial y}\cdot\frac{\partial y}{\partial \delta}\cdot\frac{\partial \delta}{\partial \ln(1/x_p)} = 0 \quad (8.6)$$

Since $\partial g/\partial y = Ne^y$ and $\partial\delta/\partial\ln(1/x_p) = 1/\sigma$ cannot be equated to zero, the only maxima of the distribution are solutions of the following cubic equation

$$\frac{\partial y}{\partial \delta} = k\delta^3 + 3s\delta^2 - 3(2+k)\delta - 3s = 0 \quad (8.7)$$

from which $\ln(1/x_p)_{max}$ can be evaluated.

Attempts were made to solve equation 8.7 algebraically using the REDUCE [66] package, however, no sensible solutions were found which could be substituted back into the equation, due to known limitations of this package in solving cubic equations [67]. Instead the coefficients k and s obtained from the fit were substituted into equation 8.7 which was then solved numerically. A rigorous determination of the statistical error on $\ln(1/x_p)_{max}$ from this method is difficult. As m and $\ln(1/x_p)_{max}$ are highly correlated the statistical error on m was used as an estimate of the statistical error on $\ln(1/x_p)_{max}$.

Figure 8.11 shows the same selected bins in x and Q^2 as illustrated in figure 8.9 with the distorted Gaussian fit. In general the fitted function is simultaneously able to well describe the leading edge of the distribution and the peak position. The fit parameters P1-P5 indicated on the plots correspond to N, m, σ, s and k respectively. Fitting the distorted Gaussian produces significantly larger statistical errors on the $\ln(1/x_p)_{max}$ measurement than the standard Gaussian fit due to the increased number of parameters in the fit.

Even when extending the fit over the maximum valid range, the difficulty with the fit to the DIS data is that the number of degrees of freedom in the fit is small at low values of Q. However, in some bins the distorted Gaussian appears to provide a better fit of the peak position. The fitted parameters and the χ^2/dof indicating the quality of the fit are shown in table 8.4 together with the derived value of $\ln(1/x_p)_{max}$.

x range	Q (GeV)	$N\pm$ stat	$m\pm$stat	$\sigma\pm$ stat	$s\pm$stat	$k\pm$ stat	$\ln(1/x_p)$ $\pm$ stat	χ^2/dof
$6.0-1.2\times10^{-4}$	3.75	0.72±0.05	1.39±0.08	0.58±0.09	-0.21±0.37	-0.49±0.73	1.471±0.082	5.19/4
$1.2-2.4\times10^{-3}$	3.78	0.58±0.09	1.93±0.14	-0.94±0.10	-1.51±0.53	-0.12±1.04	1.471 ± 0.136	0.53/4
	5.28	0.81±0.22	1.97± 0.21	0.89±0.20	1.22±0.10	0.54±1.28	1.607 ± 0.211	5.94/5
	7.26	1.24±0.07	1.80±0.13	0.64±0.08	-0.24±0.38	-1.25±0.53	1.978 ± 0.126	6.77/6
$2.4-10.0\times10^{-3}$	5.31	0.80±0.20	1.86±0.17	0.86±0.20	1.01±0.86	1.00±1.46	1.614 ± 0.172	11.09/5
	7.37	1.33±0.05	1.76± 0.05	0.60±0.04	-0.36±0.21	-1.03±0.34	1.982 ± 0.048	4.79/6
	10.45	1.37±0.28	2.20±0.31	0.63±0.29	0.11±0.94	-0.31±1.34	2.142 ± 0.309	8.35/8
	14.46	1.70±0.17	2.28±0.19	0.78±0.12	0.04±0.62	-1.06±0.53	2.316 ± 0.188	8.57/9
$1.0-5.0\times10^{-2}$	20.44	1.88±0.19	2.57±0.20	0.81±0.17	-0.46±0.53	-1.12±1.03	2.236 ± 0.198	5.11/9
	29.19	1.64±1.88	4.41±0.49	1.70±0.63	1.11±3.94	-3.43±2.80	2.607 ± 0.489	5.21/10

Table 8.4: *Fitted values of* $\ln(1/x_p)_{max}$ *from a distorted Gaussian fit over* $0 < \ln(1/x_p) < \ln(Q/2\Lambda_{EFF})$.

Figure 8.12 shows the distorted Gaussian fits to the TASSO and OPAL data fitted over the range $0 < \ln(1/x_P) < \ln(Q/2\Lambda_{EFF})$. The distorted Gaussian describes well the leading rise of the distributions. At TASSO energies the peak position is better described by the distorted Gaussian. The standard Gaussian distribution, however, provides a better representation of the OPAL peak. The fit parameters and the χ^2/dof are shown in table 8.5.

8.6 Energy Evolution of the Maximum

As discussed in chapter 4 coherence reduces the amount of QCD radiation produced in the parton cascade. The evolution of the $\ln(1/x_p)$ peak will therefore be reduced with respect to the incoherent situation. Hadronisation effects may

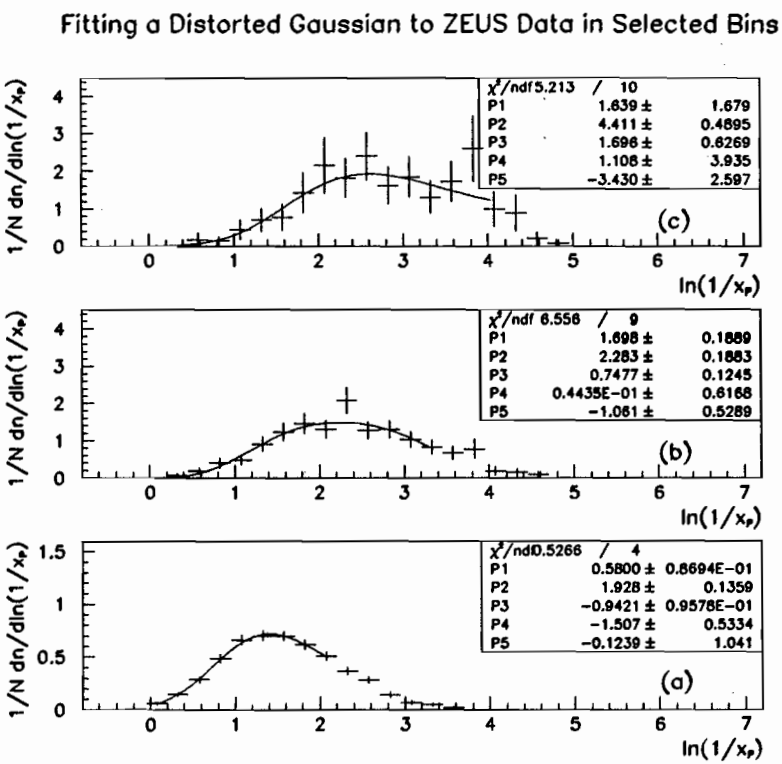

Figure 8.11: *Corrected ZEUS* $\ln(1/x_p)$ *distributions measured in a)*$1.2\times10^{-3} < x < 2.4\times10^{-3}$ *and* $10 < Q^2 < 220\ GeV^2$ *b)*$1.0\times10^{-3} < x < 1.0\times10^{-2}$ *and* $160 < Q^2 < 320\ GeV^2$ *c)*$1.0\times10^{-2} < x < 5.0\times10^{-2}$ *and* $640 < Q^2 < 1280\ GeV^2$. *The distorted Gaussian was fitted over the range* $0 < \ln(1/x_p) < \ln(Q/2\Lambda_{EFF})$ *and is shown together with the parameters of the fit.*

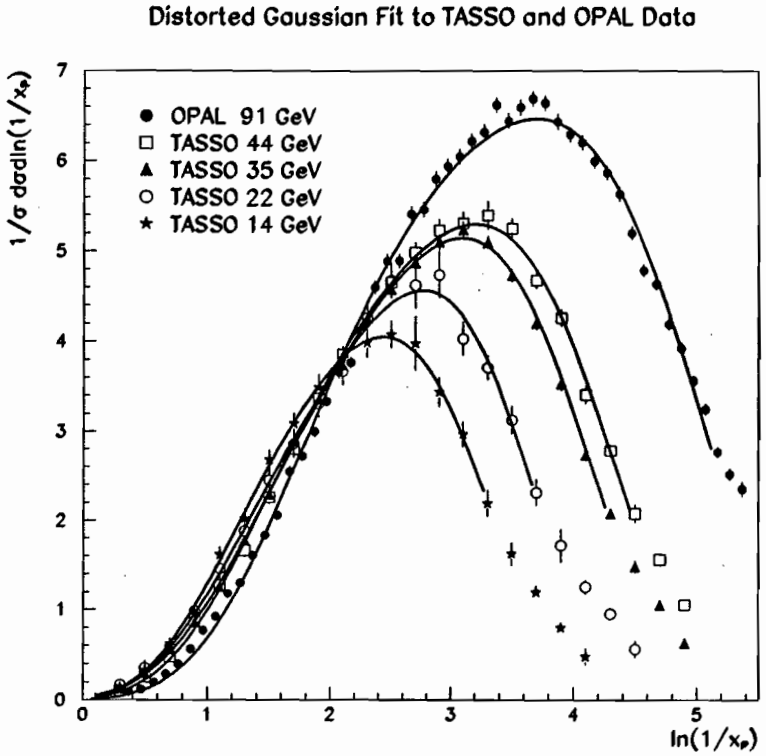

Figure 8.12: $\ln(1/x_p)$ *distributions measured by OPAL and TASSO at different CM energies. The fits shown are to a distorted Gaussian distribution over the range* $0 < \ln(1/x_p) < \ln(E_{cm}/\Lambda_{EFF})$.

Experiment	E_{CM} (GeV)	$N \pm$ stat	$m \pm$ stat	$\sigma \pm$ stat	$s \pm$ stat	$k \pm$ stat	$\ln(1/x_p)_{max} \pm$ stat	χ^2/dof
TASSO	14	4.48±0.09	2.27±0.03	0.74±0.03	-0.25±0.11	-0.92±0.17	2.436±0.032	2.87/12
	22	5.02±0.09	2.51±0.02	0.80±0.02	-3.71±0.08	-1.00±0.14	2.766±0.024	8.26/14
	35	5.71±0.03	2.80±0.01	0.90±0.01	-0.37±0.03	-1.05±0.04	3.097±0.009	24.05/16
	44	5.99±0.05	2.91±0.01	0.93±0.01	-0.32±0.04	-1.17±0.06	3.215±0.012	24.82/17
OPAL	91	7.41±0.02	3.42±0.01	1.05±0.01	-0.23±0.01	-1.21±0.02	3.699±0.006	341.9/47

Table 8.5: *Results from fitting a distorted Gaussian to TASSO and OPAL data.*

influence the shape of the spectrum with regard to the MLLA predictions. If such a distortion is the same at all energies the MLLA predictions for the energy evolution of the $\ln(1/x_p)_{max}$ can be tested.

8.6.1 Comparison with Monte Carlo Models

To determine whether ZEUS data are best described by coherent or incoherent QCD parton evolutions, the data were compared to the results from hadron distributions produced from standalone Monte Carlo programs in which the QCD cascade is modelled in different ways, namely:

- ARIADNE 4.03 with Lund string fragmentation;
- MEPS with coherent parton showers and Lund string fragmentation;
- HERWIG which adopts a coherent parton showering process for the QCD cascade and uses a cluster fragmentation scheme;
- MEPS with incoherent parton showers and Lund string fragmentation; and
- MEPS with incoherent parton showers and independent fragmentation

The default Monte Carlo parameters were used throughout with two exceptions. Although the Monte Carlos have not yet been tuned to HERA data, there exists an option in ARIADNE to use parameters whose values have been tuned by the DELPHI collaboration [68] (`MSTA(3)=1`). This flag is not set by default in

ARIADNE 4.03, but was used for the sample of ARIADNE events used to correct the data and for this study. The peak position of the $\ln(1/x_p)$ distributions and the multiplicities were sensitive to this flag. Using the tuned parameters, the mean of the $\ln(1/x_p)$ distribution was observed to shift to a higher value in the lowest (x, Q^2) bin, taken as an example. The size of this shift was a $3-4\sigma$ effect and indicates that the tuned spectrum is softer than the untuned one. The effect on the mean multiplicity was more dramatic, decreasing by 40% relative to the untuned value in this bin and providing a much better agreement with the measured value in section 8.3.

Secondly, in the case of the independent fragmentation scheme, gluons were split into $u\bar{u}$, $d\bar{d}$ and $s\bar{s}$ according to the Altarelli-Parisi splitting functions, and energy, momentum and flavour were chosen to be conserved in the fragmentation process (`MSTJ(3)=3`). In the default case, no explicit conservation of any kind is applied.

In figures 8.13(a) and (b) the $\ln(1/x_p)_{\max}$ values from ZEUS data are plotted against the mean value of Q, $<Q>$. This evolution is compared to the evolution of the $\ln(1/x_p)$ peak positions obtained from each of the Monte Carlos listed above. For the DIS data the corrected $<Q>$, given by equation 8.8, was determined for each analysis bin by applying a correction factor calculated from the ARIADNE Monte Carlo.

$$<Q>^{\mathrm{DATA}}_{\mathrm{corr}} = <Q>^{\mathrm{DATA}}_{\mathrm{meas}} \cdot \frac{<Q>^{\mathrm{MC}}_{\mathrm{true}}}{<Q>^{\mathrm{MC}}_{\mathrm{meas}}} \qquad (8.8)$$

These correction factors for $<Q>$ were found to be less than 1% in the analysis bins used.

For the Monte Carlo samples, the values of $\ln(1/x_p)_{\max}$ were obtained by fitting a Gaussian over the range ± 1 around the statistical mean of the charged hadron distributions in the current region. No p_T or η cuts were applied to the charged particles and 5 K events were generated in each of the analysis bins used in the central analysis. The discontinuities present at lower values of $<Q>$ show

the difference between the two x ranges generated at the same value of $<Q>$.

The three Monte Carlos which simulate coherence in the QCD cascade provide a good description of the ZEUS data as shown in figure 8.13(a). In contrast, in figure 8.13(b), the model which uses incoherent parton showering and independent fragmentation overestimates the position of the peak in every bin and predicts a steeper evolution with $< Q >$ than observed in the data. However, using Lund fragmentation in conjunction with the incoherent MEPS only slightly overestimates the peak position suggesting that the Lund string model mimics the effects of coherence [69], an effect which has also been reported by OPAL [26].

8.6.2 Comparison with e^+e^- data

The maxima obtained by fitting the e^+e^- data, stated in table 8.3 were plotted as a function of $\sqrt{s}$. Data from ZEUS are shown together with results from TASSO and OPAL in figures 8.14 and 8.15 for the standard and distorted Gaussian fits to the data respectively.

The figures illustrate the large kinematic range over which this measurement can be made in a single HERA experiment. At high $<Q>$ the ZEUS points are consistent with the lower energy TASSO points. A clear agreement in the rate of growth of the ZEUS points with the e^+e^- points at higher $<Q>$ is observed. This implies that, although DIS and e^+e^- annihilation are very different processes, the underlying features of the QCD soft parton cascading process in the current region are similar.

At low $<Q>$, there are two ZEUS data points covering the same range in Q^2 but two different x ranges. As seen from figure 8.14, the peak positions of the two distributions at the same value of $<Q>$ agree within statistical errors. This indicates, that within the limited x range considered, the peak of the $\ln(1/x_p)$ distributions appears to be relatively insensitive to hard gluon emissions which can pull particles from the current region into the target region as discussed in

chapter 4.

8.6.3 Straight Line Approximation

Empirically, the evolution of the $\ln(1/x_p)_{max}$ with $<Q>$ can be fitted by a straight line of the form

$$\ln(1/x_p)_{max} = b \ln Q + c \qquad (8.9)$$

Figure 8.16 shows the results from fitting equation 8.9 to the measured ZEUS data. The fit yields a value of $b = 0.650 \pm 0.035 \pm 0.069$ for the gradient and $c = 0.626 \pm 0.59 \pm 0.129$ for the intercept. As the data points are highly correlated to one another, the systematic errors on b and c were determined by fitting the straight line to each set of $\ln(1/x_p)_{max}$ data points from the twelve systematic checks. This produces a relatively smaller systematic error than one obtained from separately fitting the combined upper and lower systematic deviations on the individual points. The systematic variations on b and c from the central analysis were combined in quadrature to provide an estimate of the overall systematic uncertainty. The largest individual contribution to the systematic error on b comes from using the HERWIG Monte Carlo and the alternative track reconstruction package. For the intercept, c, the determination of the peak position substantially contributes to the combined systematic error.

Also shown in figure 8.16 is the result of the fit when $b = 1$, which would be the case if the soft gluons radiated in the parton shower could radiate anywhere in cylindrical (limited p_T) phase space until hadronisation takes over at a fixed momentum scale. The χ^2/dof=11.45 emphasises that the fit to ZEUS data is not a good one and such a model does not describe the data.

Summarised in table 8.6 are the results from the straight line fits to the data from the five Monte Carlo models. The gradients from ARIADNE, HERWIG and MEPS with the coherent cascade and Lund string fragmentation are in statistical agreement with the value obtained from the data.

Model	$b \pm$ stat $\pm$ sys	$c \pm$ stat $\pm$ sys	χ^2/dof
ZEUS data	$0.650 \pm 0.035 \pm 0.069$	$0.626 \pm 0.059 \pm 0.129$	0.34
ARIADNE	0.666 ± 0.006	0.579 ± 0.014	2.27
HERWIG	0.679 ± 0.029	0.508 ± 0.052	1.07
MEPS coherent cascade and string frag	0.682 ± 0.005	0.590 ± 0.012	3.07
MEPS incoherent cascade and string frag	0.707 ± 0.005	0.638 ± 0.011	12.90
MEPS incoherent cascade and independent frag	0.864 ± 0.004	0.583 ± 0.011	8.80

Table 8.6: *Gradients from the straight line fit applied to data and Monte Carlo models.*

For MEPS with incoherent branchings the gradient from the independent fragmentation, $b = 0.864 \pm 0.004$ is in disagreement with the ZEUS data and is approaching the phase space value of $b = 1$. The gradient obtained when Lund string fragmentation was used in conjunction with the incoherent parton showering is $b = 0.707 \pm 0.005$. Although it approaches the ZEUS data result, it does not agree within 1σ of the ZEUS result.

In conclusion, models which incorporate QCD coherence within the parton cascade provide a better description of the data.

8.7 Determination of Λ_{EFF}

The MLLA predicts that the evolution of the maxima can be approximated by

$$\ln(1/x_p)_{max} = 0.5Y + \sqrt{cY} - c + O(Y^{-\frac{1}{2}}) \qquad (8.10)$$

where $c = \frac{11}{48}\frac{(1+2N_f/11N_c^3)^2}{1-2N_f/11N_c} = 0.29\,(0.35)$ for $N_f = 3(5)$ and $O(Y^{-\frac{1}{2}})$ contains higher-order corrections. Equation 8.10 contains two free parameters, Λ_{EFF} and $O(Y^{-\frac{1}{2}})$: these were found to be highly correlated. The term containing the higher-order corrections was therefore equated to zero.

Λ_{EFF} was determined by fitting equation 8.10, with Λ_{EFF} as the only free parameter and the active number of flavours to be three, to values of $\ln(1/x_p)_{max}$ obtained from the Gaussian and distorted Gaussian fits. The value of Λ_{EFF} obtained from the Gaussian fit to the ZEUS data was:

$$\Lambda_{EFF} = 251 \pm 4\,(\text{stat}) \pm 13\,(\text{sys})\ \text{MeV}.$$

Using the values of $\ln(1/x_p)_{max}$ determined from the distorted Gaussian fit yields a value of $\Lambda_{EFF} = 243 \pm 12\,(\text{stat})$ MeV, consistent with the above value.

The systematic error was determined by fitting equation 8.10 to data obtained from each of the systematic checks including the uncertainty due to fitting the peak position. Again, the systematic error quoted is the quadratic sum of the systematic deviations from the central analysis value. The largest contribution to the systematic error is from the position of the $\ln(1/x_p)_{max}$ obtained from the fit. This error is purely an experimental determination of the systematic uncertainties associated with the measurement within the theoretical arguments presented. Another technique applied to the data, fitting the limiting spectrum to the $\ln(1/x_p)$ distributions in order to extract Λ_{EFF} [57] suggests that the theoretical uncertainty associated with the measurement is ~ 50 MeV.

Figure 8.17 shows the MLLA prediction for the evolution of $\ln(1/x_p)_{max}$ with $c = 0.35$ (three flavours) and several values of Λ_{EFF} ranging from 100 to 1000 MeV

in 100 MeV intervals. This shows that the value of Λ_{EFF} within the MLLA affects the overall height of the curves rather than the gradient and indicates why the uncertainty on the measurement of the peak position is the most significant contribution to the error on Λ_{EFF}.

Whilst an independent fit to the e^+e^- data favours the lower value of $\Lambda_{EFF} = 231 \pm 3 \pm 15$ MeV, Λ_{EFF}=250 MeV indicated on figure by the solid black line describes the data well over a large range in Q from 4-91 GeV.

Experiment	$\ln(1/x_p)_{max}$ Fit	$\Lambda_{EFF}\pm$(stat)$\pm$(sys)	χ^2/dof
ZEUS	Gaussian	251±4±13	0.36
TASSO and OPAL	Gaussian	231±3±15	3.08

Table 8.7: *Summary of the Λ_{EFF} results obtained keeping* c *fixed to the theoretical value for 3 flavours.*

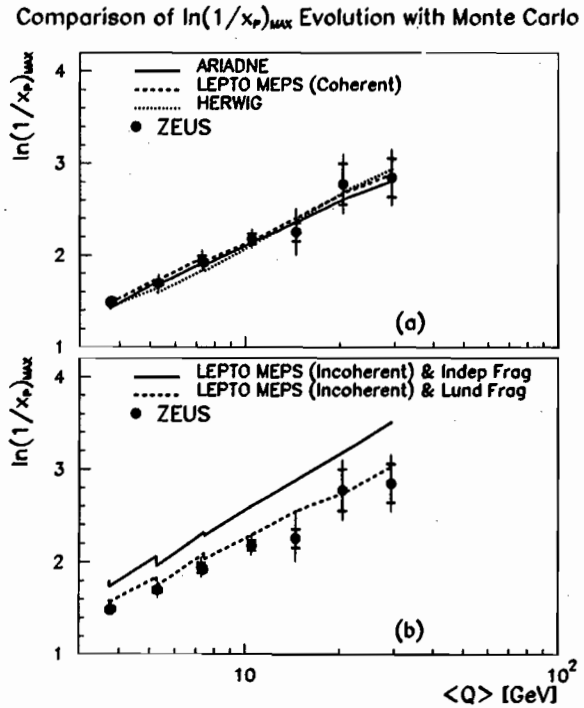

Figure 8.13: *Comparison of the* $\ln(1/x_p)$ *evolution of* $\ln(1/x_p)_{\rm max}$ *with* $<Q>$ *and Monte Carlo models. There are two data points at each of the three lowest values of* $<Q>$ *corresponding to two* x *ranges covered at the same* $<Q>$ *value. The discontinuities in the Monte Carlo lines show the differences between the generated* $\ln(1/x_p)_{\rm max}$ *values measured in the two different* x *ranges. The inner error bars represent the statistical error whilst the outer error bars show the quadratic sum of the statistical and the systematic errors added in quadrature.*

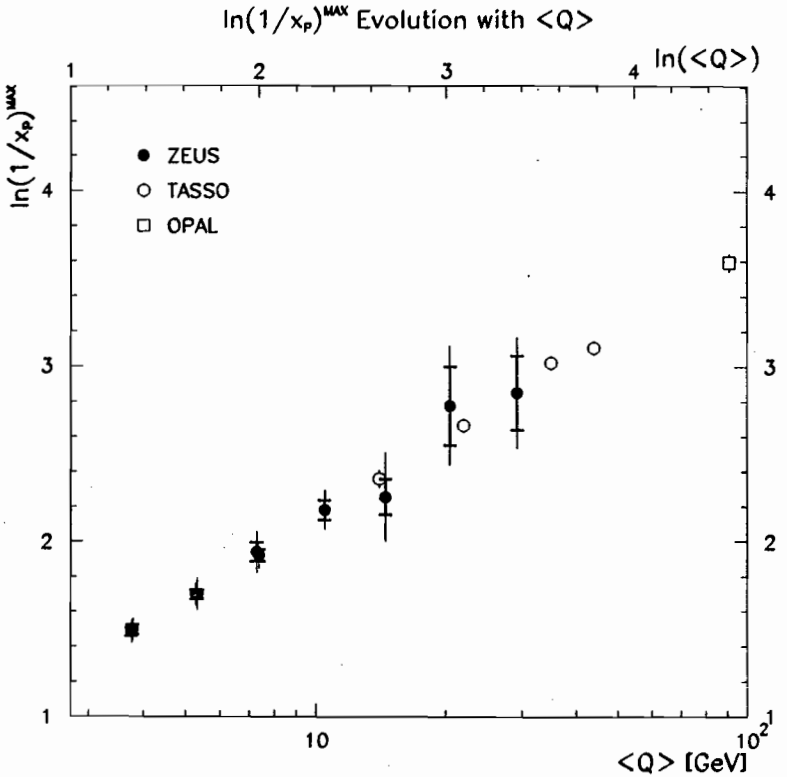

Figure 8.14: *Evolution of* $\ln(1/x_p)_{\rm max}$ *with* $<Q>$ *determined by fitting a Gaussian to ZEUS, TASSO and OPAL data. Statistical and systematic errors are shown.*

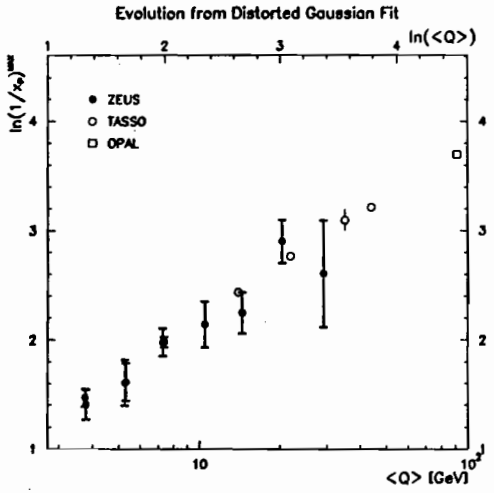

Figure 8.15: *Evolution of* $\ln(1/x_p)_{\rm max}$ *with* <Q> *determined by fitting a distorted Gaussian to ZEUS, TASSO and OPAL data. The error bars indicate the statistical errors only.*

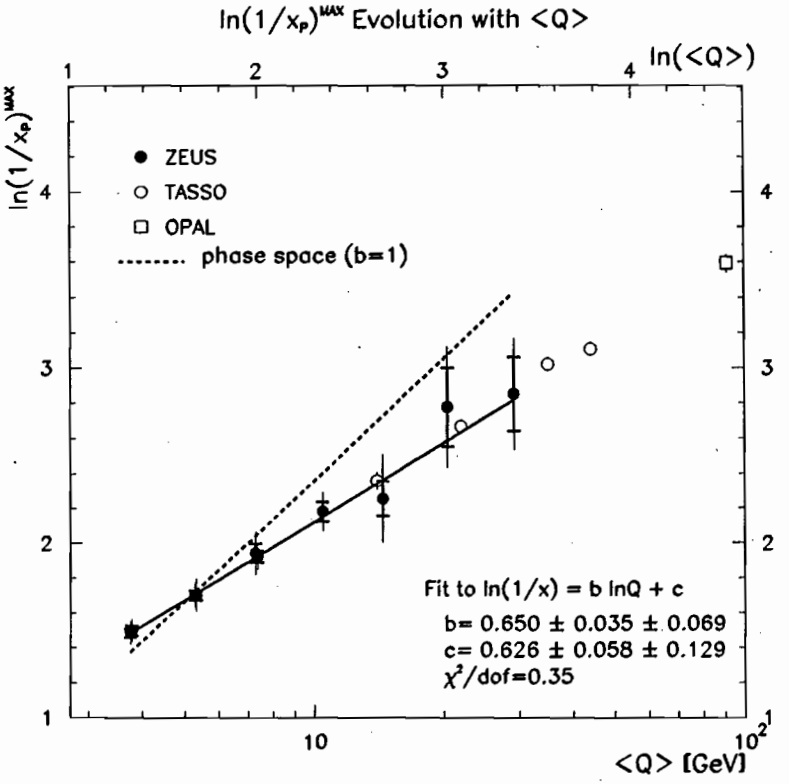

Figure 8.16: *Straight line Fit of* $b \ln Q + c$ *to the* $\ln(1/x_p)_{\rm max}$ *values measured using ZEUS data.*

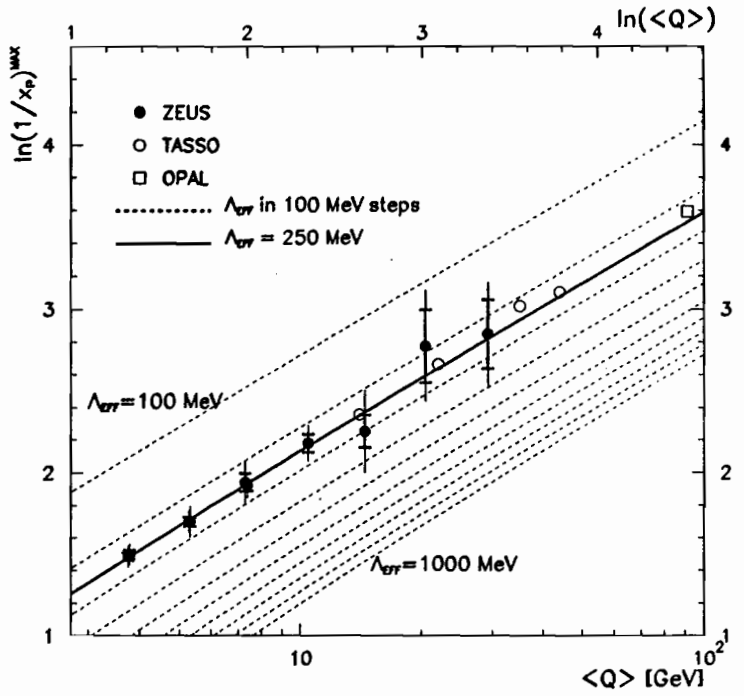

Figure 8.17: *MLLA curves as a function of* Λ_{EFF} *in intervals of 100 MeV.* Λ_{EFF}*=250 MeV describes the evolution of the data over a large range in* Q.

Chapter 9

Summary and Conclusions

This thesis has presented a first measurement of scaled momentum distributions in the current region of the Breit frame at HERA and a comparison of the evolution with Q of the peak position to data from e^+e^- annihilation experiments. The large kinematic range accessible to HERA has allowed the measurement to be made in ten regions of phase space in the range $6.0 \times 10^{-4} < x < 5.0 \times 10^{-2}$ and $10 < Q^2 < 1280$ GeV^2 commensurate with the x and Q^2 resolution offered by the ZEUS detector.

Charged tracks in the hadronic final state of DIS events were measured using the ZEUS CTD, the efficiency of which was measured to be $\sim$ 95% during the 1993 running period in which the data were collected. The tracks were subsequently boosted to the Breit frame of reference in which a comparison between the fragmentation properties of the struck quark in DIS events and those from $e^+e^- \rightarrow q\bar{q}$ can be made.

The reconstruction of the required Lorentz boost from the HERA laboratory frame to the Breit frame limits the resolution with which the inclusive scaled momentum distributions can be measured, nevertheless the $\ln(1/x_p)$ distributions can be measured with a sufficiently high resolution to provide an accurate determination of the peak position.

Data were corrected using bin-by-bin correction factors determined from Monte Carlo and the main systematic errors were studied. The dominant sources of systematic uncertainty were found to emanate from the choice of tracking algorithm used and Monte Carlo model used to correct the data.

The average charged particle multiplicity per event, $<n_{ch}>$, was determined from the integral of the $\ln(1/x_p)$ distributions and its evolution with Q was compared to data from PLUTO, TASSO, HRS and ZEUS. Within statistical errors, the data are consistent with those from the e^+e^- experiments at high values of Q. At low Q higher order effects result in an event topology which depopulates the current region. The scaled momentum distributions were found to be insensitive to the flavour composition of the primary-produced quark.

A common method was presented to evaluate the peak positions of the $\ln(1/x_p)$ distributions in ZEUS, TASSO and OPAL data. Such measurements by these e^+e^- experiments have provided evidence of the coherence phenomenon which reduces the phase space available for soft particle emissions. Evidence for coherence in DIS has also been presented by studying the evolution with Q of the peak position. The slope of this evolution is reduced compared to the value which would be obtained if the gluon emissions were not restricted by coherence. The evolution of the peak position was compared to Monte Carlo models in which coherence effects can be optionally removed. The ZEUS data were shown to favour models in which coherence is included, and definitely rule out a model in which incoherent parton branchings are used in conjunction with an independent fragmentation scheme. However, the Lund string model of fragmentation was shown to reproduce the effects of coherence to a substantial extent. This suggests that whilst the data appear to favour a model in which coherence is applied, the interplay between coherence and hadronisation is important in such measurements.

The evolution was compared to the TASSO and OPAL points. The ZEUS

data complement the e^+e^- results, extending the range in Q to lower values. At high Q the ZEUS data points agree with the lower energy TASSO data. A clear agreement in the rate of growth of the ZEUS data points with the e^+e^- points at higher Q is observed.

Predictions of the MLLA were fitted to the evolution of the ZEUS data in order to extract Λ_{EFF}, a free parameter in this theory. The fit provides a value of $\Lambda_{EFF} = 251 \pm 4\,(\text{stat}) \pm 13\,(\text{sys})$ MeV which describes the evolution from $4 \lesssim Q \lesssim 90$ GeV. The data are consistent with the predictions of the MLLA and the assumptions of LPHD.

The clear agreement in the rate of growth of the ZEUS and e^+e^- data points at higher Q indicates that the fragmentation properties of the struck quark from the proton in DIS are very similar to those from the quarks created in e^+e^- annihilation. The results therefore provide evidence for the universality of quark fragmentation.

Appendix A

Preselection of Data

A.1 Selection Procedure

The Third Level Trigger (TLT) has a loose selection procedure used by all the physics groups to reject beam-gas events, cosmic rays and fake signals in the calorimeter due to sparks, followed by filters designed specifically by each physics group. Approximately 1.1 million events are selected for the DIS group at the TLT and are written to a Data Summary Tape (DST) much of which still contains background contamination. Events from the DST are passed to the offline reconstruction which includes a filter where stricter cuts are applied using correct calibration constants. During the reconstruction, filter bits are set according to information from the reconstructed vertex and electron finder.

A.1.1 Bit Selection

For the analysis described in this thesis, events were required to have a specific filter bit which corresponds to the following requirements:

- Calorimeter timing: $|t_R| < 6$ ns; and $|t_F - t_R| < 8$ ns and a global calorimter timing cut of $|t_G| < 8$ ns;

- Remove cosmic and halo muon events;
- Remove calorimeter sparks;
- $\delta = E - P_z + 2E_\gamma < 35$ GeV if an event vertex has been found, otherwise $\delta > 25$ GeV;
- For a logical OR of two high-efficiency electron finding algorithms, the electron energy has to be greater than 5 GeV;
- $y_{JB} > 0.02$;
- the electron must have an impact point on the face of the RCAL which satisfies $|x| < 16$ cm and $|y| < 16$ cm.

Events which satisfied these cuts form a mini-DST; however, additional cuts are applied at the next stage, known as preselection.

A.1.2 Preselection

Tighter cuts were applied at the preselection level. Events were required to satisfy the following cuts:

- Filter bit set;
- Remove events in which the detector did not operate efficiently;
- A logical OR of two vertex finding algorithms, VCTRAK .OR. TGTRAK, provides a $|z_{vtx}| < 75$ cm;
- A tighter RCAL timing cut of $t_R < 3$ ns for $E_{RCAL} > 5$ GeV.

Appendix B

Tables of Data

$\ln(1/x_p)$	$1/N\,dn/d\ln(1/x_p) \pm \Delta(\text{stat}) \pm \Delta(\text{sys})$
	$6.0 \times 10^{-4} < x < 1.2 \times 10^{-3}$
	$10 < Q^2 < 20$ GeV^2
-0.55 - -0.30	0.001 ± 0.001 ± 0.002
-0.30 - -0.05	0.014 ± 0.005 ± 0.009
-0.05 - 0.20	0.061 ± 0.012 ± 0.015
0.20 - 0.45	0.201 ± 0.026 ± 0.090
0.45 - 0.70	0.262 ± 0.027 ± 0.029
0.70 - 0.95	0.419 ± 0.035 ± 0.073
0.95 - 1.20	0.613 ± 0.044 ± 0.079
1.20 - 1.45	0.661 ± 0.046 ± 0.098
1.45 - 1.70	0.675 ± 0.046 ± 0.073
1.70 - 1.95	0.580 ± 0.043 ± 0.113
1.95 - 2.20	0.420 ± 0.036 ± 0.025
2.20 - 2.45	0.306 ± 0.031 ± 0.056
2.45 - 2.70	0.259 ± 0.032 ± 0.080
2.70 - 2.95	0.133 ± 0.023 ± 0.019
2.95 - 3.20	0.104 ± 0.024 ± 0.018
3.20 - 3.45	0.019 ± 0.009 ± 0.033
3.45 - 3.70	0.101 ± 0.118 ± 0.119

Table B.1: *Normalised* $\ln(1/x_p)$ *distributions,* $(1/N)dn/d\ln(1/x_p)$*, in the kinematic range* $6.0 \times 10^{-4} < x < 1.2 \times 10^{-3}$ *and* $10 < Q^2 < 20$ GeV^2.

$\ln(1/x_p)$	$1/N\,dn/d\ln(1/x_p) \pm \Delta(\text{stat}) \pm \Delta(\text{sys})$		
	$1.2 \times 10^{-3} < x < 2.4 \times 10^{-3}$		
	$10 < Q^2 < 20$	$20 < Q^2 < 40$	$40 < Q^2 < 80$
-0.55 - -0.30	0.003 ± 0.002 ± 0.003	-	-
-0.30 - -0.05	0.008 ± 0.003 ± 0.007	0.007 ± 0.005 ± 0.005	0.002 ± 0.003 ± 0.032
-0.05 - 0.20	0.059 ± 0.012 ± 0.008	0.035 ± 0.012 ± 0.010	0.022 ± 0.012 ± 0.038
0.20 - 0.45	0.145 ± 0.020 ± 0.027	0.123 ± 0.023 ± 0.043	0.129 ± 0.040 ± 0.026
0.45 - 0.70	0.289 ± 0.030 ± 0.034	0.294 ± 0.044 ± 0.074	0.336 ± 0.076 ± 0.076
0.70 - 0.95	0.485 ± 0.040 ± 0.088	0.394 ± 0.045 ± 0.023	0.549 ± 0.094 ± 0.181
0.95 - 1.20	0.660 ± 0.048 ± 0.140	0.723 ± 0.067 ± 0.099	0.629 ± 0.094 ± 0.104
1.20 - 1.45	0.699 ± 0.049 ± 0.094	0.971 ± 0.083 ± 0.130	0.778 ± 0.097 ± 0.086
1.45 - 1.70	0.694 ± 0.049 ± 0.039	1.002 ± 0.083 ± 0.215	1.176 ± 0.138 ± 0.372
1.70 - 1.95	0.616 ± 0.046 ± 0.050	0.945 ± 0.078 ± 0.198	1.209 ± 0.141 ± 0.285
1.95 - 2.20	0.506 ± 0.044 ± 0.117	0.741 ± 0.065 ± 0.058	1.013 ± 0.118 ± 0.166
2.20 - 2.45	0.366 ± 0.038 ± 0.043	0.675 ± 0.068 ± 0.097	0.906 ± 0.111 ± 0.156
2.45 - 2.70	0.383 ± 0.036 ± 0.128	0.520 ± 0.064 ± 0.138	0.828 ± 0.113 ± 0.285
2.70 - 2.95	0.138 ± 0.027 ± 0.053	0.277 ± 0.042 ± 0.082	0.723 ± 0.116 ± 0.121
2.95 - 3.20	0.069 ± 0.018 ± 0.010	0.271 ± 0.047 ± 0.059	0.431 ± 0.082 ± 0.114
3.20 - 3.45	0.048 ± 0.017 ± 0.029	0.132 ± 0.037 ± 0.033	0.294 ± 0.077 ± 0.104
3.45 - 3.70	0.020 ± 0.013 ± 0.025	0.046 ± 0.021 ± 0.034	0.245 ± 0.087 ± 0.125
3.70 - 3.95	-	0.022 ± 0.017 ± 0.015	0.093 ± 0.054 ± 0.060

Table B.2: *Normalised* $\ln(1/x_p)$ *distributions in the kinematic range* $1.2 \times 10^{-3} < x < 2.4 \times 10^{-3}$ *and three regions of* Q^2*:* $10 < Q^2 < 20$ GeV^2*;* $20 < Q^2 < 40$ GeV^2*; and* $40 < Q^2 < 80$ GeV^2.

$\ln(1/x_p)$	$1/N\ dn/d\ln(1/x_p) \pm \Delta(\text{stat}) \pm \Delta(\text{sys})$			
	$2.4 \times 10^{-3} < x < 1.0 \times 10^{-2}$			
	$20 < Q^2 < 40$	$40 < Q^2 < 80$	$80 < Q^2 < 160$	$160 < Q^2 < 320$
-0.05 - 0.20	0.006 ± 0.004 ± 0.007	0.009 ± 0.009 ± 0.007	-	-
0.20 - 0.45	0.065 ± 0.019 ± 0.029	0.022 ± 0.010 ± 0.028	0.048 ± 0.048 ± 0.057	0.003 ± 0.005 ± 0.044
0.45 - 0.70	0.095 ± 0.017 ± 0.014	0.096 ± 0.022 ± 0.081	0.096 ± 0.037 ± 0.013	0.078 ± 0.054 ± 0.054
0.70 - 0.95	0.304 ± 0.039 ± 0.069	0.299 ± 0.048 ± 0.109	0.225 ± 0.054 ± 0.045	0.191 ± 0.086 ± 0.172
0.95 - 1.20	0.419 ± 0.041 ± 0.032	0.449 ± 0.055 ± 0.083	0.307 ± 0.060 ± 0.113	0.402 ± 0.137 ± 0.141
1.20 - 1.45	0.641 ± 0.055 ± 0.089	0.832 ± 0.081 ± 0.088	0.750 ± 0.106 ± 0.243	0.484 ± 0.136 ± 0.096
1.45 - 1.70	1.016 ± 0.075 ± 0.187	0.940 ± 0.077 ± 0.095	0.803 ± 0.100 ± 0.107	0.907 ± 0.203 ± 0.156
1.70 - 1.95	0.932 ± 0.065 ± 0.120	1.031 ± 0.081 ± 0.101	1.099 ± 0.120 ± 0.091	1.226 ± 0.238 ± 0.263
1.95 - 2.20	0.984 ± 0.071 ± 0.178	1.286 ± 0.097 ± 0.251	1.248 ± 0.128 ± 0.268	1.457 ± 0.273 ± 0.573
2.20 - 2.45	0.727 ± 0.056 ± 0.187	1.118 ± 0.086 ± 0.138	1.204 ± 0.121 ± 0.131	1.299 ± 0.231 ± 0.304
2.45 - 2.70	0.622 ± 0.053 ± 0.181	1.077 ± 0.090 ± 0.196	1.457 ± 0.143 ± 0.281	2.073 ± 0.348 ± 0.810
2.70 - 2.95	0.512 ± 0.053 ± 0.089	0.746 ± 0.069 ± 0.102	1.111 ± 0.116 ± 0.417	1.272 ± 0.233 ± 0.146
2.95 - 3.20	0.304 ± 0.038 ± 0.092	0.640 ± 0.071 ± 0.081	1.023 ± 0.118 ± 0.141	1.302 ± 0.240 ± 0.113
3.20 - 3.45	0.177 ± 0.028 ± 0.027	0.457 ± 0.058 ± 0.043	0.761 ± 0.105 ± 0.143	1.022 ± 0.214 ± 0.223
3.45 - 3.70	0.166 ± 0.035 ± 0.088	0.310 ± 0.049 ± 0.089	0.642 ± 0.104 ± 0.231	0.523 ± 0.195 ± 0.197
3.70 - 3.95	0.068 ± 0.023 ± 0.089	0.138 ± 0.032 ± 0.048	0.338 ± 0.070 ± 0.066	0.667 ± 0.186 ± 0.122
3.95 - 4.20	0.057 ± 0.032 ± 0.043	0.071 ± 0.023 ± 0.034	0.351 ± 0.106 ± 0.244	0.774 ± 0.287 ± 0.368
4.20 - 4.45	0.040 ± 0.056 ± 0.040	0.042 ± 0.021 ± 0.058	0.105 ± 0.043 ± 0.162	0.186 ± 0.113 ± 0.208
4.45 - 4.70	-	0.080 ± 0.071 ± 0.113	0.005 ± 0.052 ± 0.083	0.151 ± 0.100 ± 0.260
4.70 - 4.95	-	-	-	0.091 ± 0.097 ± 0.070

Table B.3: *Normalised* $\ln(1/x_p)$ *distributions in the kinematic range* $2.4 \times 10^{-3} < x < 1.0 \times 10^{-2}$ *and four regions of* Q^2*:* $20 < Q^2 < 40$ GeV^2; $40 < Q^2 < 80$ GeV^2; $80 < Q^2 < 160$ GeV^2; *and* $160 < Q^2 < 320$ GeV^2.

$\ln(1/x_p)$	$1/N\ dn/d\ln(1/x_p) \pm \Delta(\text{stat}) \pm \Delta(\text{sys})$	
	$1.0 \times 10^{-2} < x < 5.0 \times 10^{-2}$	
	$320 < Q^2 < 640$	$640 < Q^2 < 1280$
0.20 - 0.45	0.117 ± 0.156 ± 0.074	-
0.45 - 0.70	0.131 ± 0.083 ± 0.442	0.168 ± 0.194 ± 0.135
0.70 - 0.95	0.456 ± 0.199 ± 0.265	0.144 ± 0.125 ± 0.148
0.95 - 1.20	0.382 ± 0.132 ± 0.202	0.449 ± 0.270 ± 0.296
1.20 - 1.45	0.745 ± 0.240 ± 0.224	0.701 ± 0.323 ± 0.689
1.45 - 1.70	1.525 ± 0.427 ± 0.891	0.772 ± 0.348 ± 1.869
1.70 - 1.95	1.141 ± 0.268 ± 0.181	1.418 ± 0.539 ± 1.024
1.95 - 2.20	1.140 ± 0.247 ± 1.308	2.151 ± 0.744 ± 1.183
2.20 - 2.45	1.707 ± 0.353 ± 0.318	1.818 ± 0.523 ± 0.576
2.45 - 2.70	1.662 ± 0.308 ± 0.712	2.394 ± 0.647 ± 0.877
2.70 - 2.95	1.538 ± 0.335 ± 0.451	1.616 ± 0.496 ± 0.457
2.95 - 3.20	1.964 ± 0.431 ± 0.526	1.843 ± 0.541 ± 0.943
3.20 - 3.45	1.478 ± 0.347 ± 0.343	1.307 ± 0.436 ± 0.205
3.45 - 3.70	1.191 ± 0.317 ± 0.143	1.723 ± 0.538 ± 1.047
3.70 - 3.95	0.799 ± 0.236 ± 0.267	2.593 ± 0.883 ± 1.744
3.95 - 4.20	0.552 ± 0.229 ± 0.294	0.993 ± 0.466 ± 0.633
4.20 - 4.45	0.310 ± 0.190 ± 0.187	0.884 ± 0.490 ± 0.436
4.45 - 4.70	0.019 ± 0.022 ± 0.097	0.210 ± 0.175 ± 0.229
4.70 - 4.95	0.029 ± 0.035 ± 0.033	0.075 ± 0.094 ± 0.150

Table B.4: *Normalised* $\ln(1/x_p)$ *distributions in the kinematic range* $1.0 \times 10^{-2} < x < 5.0 \times 10^{-2}$ *and two regions of* Q^2*:* $320 < Q^2 < 640$ GeV^2; *and* $640 < Q^2 < 1280$ GeV^2.

References

[1] The ZEUS Detector, Status Report 1993, DESY 1993.

[2] B. Foster et al., Nucl. Instr. and Meth. A338 (1994) 254.

[3] Presentation given by M. Lancaster, ZEUS Collaboration Meeting, November 1993.

[4] C. Alvisi et al., Nucl. Instr. and Meth. A305 (1991) 30.

[5] B. Bock et al., Nucl. Instr. and Meth. A344 (1994) 335.

[6] A. Andersen et al., Nucl. Instr. and Meth. A336 (1993) 23.

[7] J. Andruszków et al., DESY 92-066 (1992).

[8] D. Bandyopadhyay et al., "VCTRAK Offline Output Information", ZEUS internal note 93-122.

[9] G. Bruni et al., "A Description of TGTRAK and Associated Tables", ZEUS internal note 94-009

[10] R.E. Kalman, J. Basic Eng. 82 (1960) 35.
R.E. Kalman and R.S. Bucy, ibid. 83 (1961) 95.

[11] P. Billoir and S.Qian, Nucl. Instr. and Meth. A311 (1992) 139.

[12] T. Yip, Private Communication.

[13] GEANT 3.13: R. Brun et al., CERN DD/EE/84-1 (1987).

[14] S. Bentvelsen et al., Physics at HERA Vol. 1 (1991) 23.
S. Bentvelsen, PhD Thesis University of Amsterdam 1994.

[15] J.I. Friedman and H.W. Kendall, Annual Review of Nucl. and Particle Science, Vol. 22 (1972) 227.

[16] C.G. Callan and D. Gross, Phys. Rev. Lett. 22 (1969) 156.

[17] A. Bodek et al., Phys. Rev. D 20 (1979) 1471.

[18] CDHS Collaboration, H. Abramowicz et al., Z. Phys. C 17 (1983) 283.
EMC Collaboration, J.J. Aubert et al., Phys. Lett. B 105 (1981) 322.

[19] R.E Taylor, Proceedings of the Int. Symposium on Lepton and Photon Interactions at High Energies (1975) 679.

[20] G. Altarelli and G. Parisi, Nucl. Phys. B 126 (1977) 298.

[21] A. Chudakov, Ivz. Akad. Nauk SSSR, Ser. Fiz. 19 (1955) 650.

[22] Ya.I. Azimov, Yu.L Dokshitzer, V.A. Khoze and S.I. Troyan, Z. Phys. C 31 (1986) 213.

[23] Yu.L Dokshitzer, V.A. Khoze, A.H. Mueller and S.I. Troyan, "Basics of Perturbative QCD", Editions Frontières, 1991.

[24] Ya.I. Azimov, Yu.L. Dokshitzer, V.A. Khoze and S.I. Troyan, Z.Phys. C 27 (1985) 65.

[25] TASSO Collaboration, W. Braunschweig et al., Z. Phys. C 47 (1990) 187.

[26] OPAL Collaboration, M.Z. Akrawy et al., Phys. Lett. B 247 (1990) 617.

[27] L3 Collaboration, B. Adeva et al., Phys. Lett. B 259 (1991) 199.

[28] E.R. Boudinov, P.V. Chliapnikov and V.A. Uvarov, Phys. Lett. B 309 (1993) 210.

[29] A.V. Anisovich et al., Nuovo Cimento A 106 (1993) 547.

[30] I.J.R. Aitchison and A.J.G. Hey, "Gauge Theories in Particle Physics", 2nd edition, p.230-231, Adam Higler, 1989.

[31] K. Charchuła, J. Phys. G 19 (1993) 1587.

[32] K.H. Streng, T.F. Walsh, and P.M. Zerwas, Z. Phys. C 2 (1979) 237.

[33] ZEUS Collaboration, M. Derrick et al., Phys. Lett. B 315 (1993) 481.

[34] ZEUS Collaboration, M. Derrick et al., DESY 94-117 accepted by Phys. Lett. B.

[35] Yu.L. Dokshitzer, V.A. Khoze, S.I. Troyan and A.H. Mueller, Rev. of Mod. Phys. 60 (1988) 373.

[36] G. Ingelman and J. Rathsman, J. Phys. G 19 (1993) 1694.

[37] G. Ingelman, Proceedings of the 1991 Workshop on Physics at HERA, DESY Vol. 3 (1992) 1366.

[38] A. Kwiatkowski, H. Spiesberger and H.-J. Möring, Proceedings of the 1991 Workshop on Physics at HERA, DESY Vol. 3 (1992) 1294.

[39] G.A. Schuler and H. Spiesberger, Proceedings of the 1991 Workshop on Physics at HERA, DESY Vol. 3 (1992) 1419.

[40] A.D. Martin, R.G. Roberts and W.J. Stirling, Phys. Lett. B 306 (1993) 145.

[41] ZEUS Collaboration, M. Derrick et al., Phys. Lett. B 316 (1993) 412.
H1 Collaboration, I. Abt et al., Nucl. Phys. B 407 (1993) 515.

[42] ARIADNE 3.1: L. Lönnblad, Comput. Phys. Commun. 71 (1992) 15.

[43] B. Andersson et al., Phys. Rep. 97 (1983) 31.

[44] JETSET 6.3: T. Sjöstrand, Comput. Phys. Commun. 39 (1986) 347.
T. Sjöstrand and M. Bengtesson, Comput. Phys. Commun. 43 (1987) 347.

[45] ZEUS Collaboration, M. Derrick et al., Z. Phys. C 59 (1993) 231.

[46] P. Bruni and G. Ingelman, DESY 93-187.

[47] A. Donnachie and P.V. Landshoff, Phys. Lett. B 191 (1987) 309.

[48] M. Glück, E. Reya and A. Vogt, Phys. Lett. B 306 (1993) 391.

[49] G. Marchesini et al.: Comput. Phys. Commun. 67 (1992) 465.

[50] G. Marchesini and B.R. Webber, Nucl. Phys. B 310 (1988) 461.

[51] H. Abramowicz et al., "A Determination of F_2 with the 1992 Data", ZEUS internal note 93-078.

[52] M. Rocco, PhD Thesis University of Iowa 1994, DESY F35D-94-04.

[53] Zeus Collab., M. Derrick et al DESY 94-143 accepted by Z. Phys. C.

[54] H. Beier, Diploma Thesis University of Hamburg 1994, DESY F35D-94-07.

[55] G. Thompson et al, J. Phys. G19 (1993) 1575.
N. McCubbin, private communication.

[56] D. Sankey, private communication.

[57] Preliminary ZEUS results presented at the XXIXth Recontres de Moriond, QCD and High Energy Hadronic Interactions, March 1994.
ZEUS Collaboration., M. Derrick et al., paper in preparation.

[58] TASSO collaboration, W. Braunschweig et al., Z. Phys. C 45 (1989) 193.

[59] PLUTO collaboration, Ch. Berger et al., Phys. Lett. B 95 (1980) 313.

[60] OPAL collaboration, P.D. Acton et al., Z. Phys. C 53 (1992) 539.

[61] HRS collaboration, M. Derrick et al., Phys. Rev. D 34 (1986) 3304.

[62] OPAL Collaboration, R. Akers et al., Z. Phys. C 61 (1994) 209.

[63] ZEUS Collaboration, M.Derrick et al., Phys. Lett. B 303 (1993) 183.

[64] H. Kreutzmann, PhD Thesis University of Bonn, Bonn-IR-91-08.

[65] C.P. Fong and B.R. Webber, Phys. Lett. B 229 (1989) 289.

[66] The Rand Corporation, "REDUCE User's Manual", Rand Publication CP78 April 1985.

[67] G. Rayna, "REDUCE: Software for Algebraic Computation" p. 74, Springer-Verlag 1987.

[68] W. de Boer and H. Fürstenau, Proceedings of the MC91 Monte Carlo Workshop, Amsterdam (1991) 616. and IEKP-KA/91-07.

[69] G. Gustafson, private communication.

Acknowledgements

I am grateful to Professor David Saxon for giving me the opportunity to work with the ZEUS group at Glasgow University. The strong support and encouragement from my colleagues at Glasgow has been invaluable. In particular, Drs Tony Doyle and Nick Brook have guided me through my research and provoked many interesting and valuable discussions. I thank the many members of the ZEUS collaboration who have also assisted me with my research.

The financial support of the UK Engineering and Physical Sciences Research Council is gratefully acknowledged.

Acknowledgements

I am grateful to Professor David Saxon for giving me the opportunity to work with the ZEUS group at Glasgow University. The strong support and encouragement from my colleagues at Glasgow has been invaluable. In particular, Drs Tony Doyle and Nick Brook have guided me through my research and provoked many interesting and valuable discussions. I thank the many members of the ZEUS collaboration who have also assisted me with my research.

The financial support of the UK Engineering and Physical Sciences Research Council is gratefully acknowledged.